

EVALUATION OF UNDERGROUND SUPPORTS MADE OF WOOD AND
OTHER MATERIALS

by

Zhanjing Yu

Thesis submitted to the Faculty of the
Virginia Polytechnic Institute and State University
in partial fulfillment of the requirements for the degree of

MASTER OF SCIENCE

in

Mining Engineering

APPROVED:

Gavin J. Faulkner, Chairman

Michael E. Karmis

J. Richard Lucas, Department Head

Thomas E. McLain

March, 1987

Blacksburg, Virginia

EVALUATION OF UNDERGROUND SUPPORTS MADE OF WOOD AND
OTHER MATERIALS

by

Zhanjing Yu

Committee Chairman: Gavin J. Faulkner

Mining Engineering

(ABSTRACT)

A roof support system is one of the most important systems in underground mining. It may consist of various types of supports such as props, cribs, steel arches, powered supports and roof bolts, among others. In this research, powered supports and roof bolting are not included.

Evaluation of underground supports needs to take account of several factors. These factors include the mechanical behavior of the supports, the interaction between the support and the surrounding strata, the cost of the support, and the overall economic results. In this research, emphasis is placed on the mechanical behavior of the supports. Criteria have been set up and, based on these criteria, a variety of supports have been evaluated.

ACKNOWLEDGEMENTS

I would like to thank my advisor, Dr. Gavin J. Faulkner for his guidance, encouragement, help and support throughout this project. I would also like to thank the other members of my committee, Dr. Thomas E. McLain, Dr. Michael Karmis, and Dr. J. Richard Lucas for their advice and suggestions.

In addition I would like to express my gratitude to Wenliang Tang for helping to do the tests and to Zach Agioutantis and Zhongxue Li for sharing with me their computer knowledge.

I am indebted to my wife for her patient wait in China for almost two years. I am also indebted to my colleagues in Shandong Mining Institute, China for their support.

Finally, to all of my friends among the staff and students of the Department of Mining and Minerals Engineering, thanks for an enjoyable two years.

TABLE OF CONTENTS

	<u>Page</u>
AKNOWLEDGEMENTS.....	iii
LIST OF FIGURES.....	vi
LIST OF TABLES.....	xi
CHAPTER 1 INTRODUCTION	1
CHAPTER 2 CRITERIA FOR EVALUATING UNDERGROUND SUPPORTS.....	3
2.1 Resistance-Deflection Relationship — Hyperbolic.....	3
2.2 Resistance-Deflection Relationship — Linear.....	11
2.3 Criteria Based on the Resistance-Deflection Relationships.....	25
CHAPTER 3 CONVENTIONAL TIMBER SUPPORTS.....	28
3.1 Some Wood Terminology.....	31
3.2 Brief Review of Wood Structure and Properties.....	34
3.3 Timber Posts.....	42
3.4 Timber Cribs.....	57
3.5 Timber Gallery Sets.....	71
3.6 Factors Affecting the Strength and Stability of Timber Supports.....	80
CHAPTER 4. NOVEL TIMBER SUPPORTS.....	91
4.1 Micon Yield Capsule.....	91
4.2 Super Post.....	100
4.3 Wedge Prop.....	111
CHAPTER 5. CONCRETE SUPPORTS.....	139
5.1 Plain Concrete Supports.....	139

5.2	Steel Fiber Reinforced Concrete Supports.....	150
5.3	Sandwich Cribs.....	162
CHAPTER 6.	STEEL SUPPORTS.....	178
6.1	Yielding Steel Post.....	179
6.2	Steel Friction Props.....	185
6.3	Steel Arches.....	195
CHAPTER 7.	SUMMARY AND RECOMMENDATIONS.....	209
7.1	Summary.....	209
7.2	Recommendation For Future Work.....	215
REFERENCES.....		218
APPENDIX: FINITE ELEMENT PROGRAM.....		222
VITA.....		236

LIST OF FIGURES

<u>Figure</u>		<u>Page</u>
2.1	Hyperbolic Resistance-Deflection relations obtained from laboratory experiments.	5
2.2	Hyperbolic Resistance-Deflection relations obtained from underground testing.	6
2.3	Resistance-Deflection relationships similar to a hyperbolic curve.	8
2.4	Model for deriving the hyperbolic Resistance-Deflection relationship.	9
2.5	Concentrated force on an infinite beam on an elastic foundation.	13
2.6	Linearly distributed load on the infinite beam on elastic foundation.	13
2.7	Point A outside the linearly distributed load.	16
2.8	The coordinate system for roof deflection.	16
2.9	Model for finding out the deflection of the semi-infinite beam on an elastic foundation.	19
2.10	Model for calculating roof deflection.	21
2.11	Comparison between theoretical and measured deflections.	24
2.12	Three sections of the hyperbolic curve.	26
3.1	A ground control plan showing the use of timber supports.	29
3.2	Three principal directions of wood.	40
3.3	The relationship between the load bearing capacity and the height-diameter ratio.	45
3.4	Load-deformation curve of a hickory post.	47
3.5	Finite element mesh for analyzing the stress distribution in a circular post.	53
3.6	Radial stress distribution in a circular post.	54

3.7	Tangential stress distribution in a circular post. ..	55
3.8	Load-deformation curve of a beech crib.	61
3.9	Load-deformation curve of an oak crib.	62
3.10	Load-deformation curve of a hickory crib.	63
3.11	Plan view of the timber crib used for calculating the critical buckling strength.	66
3.12	Compression perpendicular to grain creep of red oak at 82° C.	69
3.13	Relaxation of a compression force acting on sugar maple perpendicular to grain.	70
3.14	Timber gallery set.	72
3.15	Model for calculating the deflection of a gallery set.	74
3.16	Modified model for calculating the deflection of gallery set.	76
3.17	Post with shoe, under test.	81
3.18	Comparison between the Load-deformation curves of the timber crib and the post with shoe.	82
3.19	Effect of moisture content at about 20°C on compressive strength parallel-to-grain. 100% at 12% moisture content.	84
3.20	Effect of moisture content at about 20°C on bending strength of wood. 100% at 12% moisture content.	85
3.21	Longitudinal stress concentration factors for various knot locations.	88
3.22	Transverse stress concentration factors for various knot locations.	89
4.1	Micon Yield Capsule.	96
4.2	Load-deformation curve of Micon Yield Capsule, post 1.	97
4.3	Load-deformation curve of Micon Yield Capsule, post 2.	98

4.4	Structure of the Super Post.	101
4.5	Load-deformation curve of Super Post, Square poplar A.	106
4.6	Load-deformation curve of Super Post, Unfinished locust B.	107
4.7	Load-deformation curve of Super Post. Unfinished white oak C.	108
4.8	Structure of the Wedge Prop.	113
4.9	The distributed load created by the band.	115
4.10	Freebody diagram of the wedge.	115
4.11	Side view of the mushroom head.	117
4.12	Top view of the mushroom head.	118
4.13	A Wedge Prop before testing.	122
4.14	A Wedge Prop under testing.	123
4.15	Load-deformation curve of Wedge Prop 1.	125
4.16	Load-deformation curve of Wedge Prop 2.	126
4.17	Load-deformation curve of Wedge Prop 3.	127
4.18	Load-deformation curve of Wedge Prop 4.	128
4.19	Load-deformation curve of Wedge Prop 5.	129
4.20	Load-deformation curve of Wedge Prop 6.	130
4.21	Wedge Prop 2 after failure. (Premature failure)	133
4.22	The head of Wedge Prop 3. (Sawcut too wide)	134
5.1	Load-deformation curve of a plain concrete crib.	142
5.2	Relationship between water-cement ratio and compressive strength of the concrete.	145
5.3	Relationship between the age and the strength of concrete.	147

5.4	Effect of high temperatures on concrete compressive strength at various ages.	149
5.5	Load-deformation curve of steel-fiber-reinforced-concrete crib.	158
5.6	Donut Crib.	160
5.7	Comparison between the load-deformation curve of Donut Crib and that of the steel-fiber-reinforced-concrete block crib.	161
5.8	Sandwich crib.	163
5.9	The effect of concrete strength on sandwich crib characteristics.	166
5.10	The effect of the block height and surface finish on sandwich crib characteristics.	167
5.11	The effect of timber species on sandwich crib characteristics.	169
5.12	Sandwich crib before testing.	171
5.13	Sandwich crib after testing.	172
5.14	Load-deformation curve of a sandwich crib.	173
5.15	Skeleton crib.	175
5.16	Comparison of the load-deformation characteristics of the sandwich crib and skeleton crib.	176
6.1	Structure of a yielding steel post.	180
6.2	Tube expanding over a conical mandrel.	183
6.3	The structure of the HZJA steel friction prop.	187
6.4	The load-deformation curve of a HZJA prop.	188
6.5	Structure of the HZWA steel friction prop.	190
6.6	Sketch for load-deformation analysis of the HZWA steel friction prop.	192
6.7	Stages of the load-deformation curve of a HZWA prop.	193
6.8	A typical load-deformation curve of a HZWA prop.	196

6.9	Load-deformation curves for single-point crown loading tests.	198
6.10	Strength of arches from single-point crown loading tests.	201
6.11	Structure of Toussaint-Heizmann arch.	203
6.12	Load-deformation curves of the yield arches for single-point crown loading with the arches being confined.	205
6.13	Load-deformation curves of the yield arches for single-point loading without confinement.	206
6.14	Load-deformation curve of the joint of the Toussaint-Heizmann arch.....	207

LIST OF TABLES

<u>Table</u>	<u>Page</u>
3.1.	Summary of wood products used in underground coal mines by category. 30
3.2	Functions relating mechanical properties to specific gravity of clear, straight-grain wood. 37
3.3	Elastic constants of various wood species. 43
3.4	The effect of height-diameter ratio on the load bearing capacity of timber post. 46
3.5	Results of compression tests of timber posts. 49
3.6	Results of compression tests on timber crib corners. .. 60
3.7	Regression constants for the L-D curves of the timber criber corners. 64
4.1	Parameters of Micon Yield Capsule Posts. 93
4.2	Parameters of Super Posts. 105
4.3	Constants from the regression equation. 109
4.4	Specifications of wedge props. 120
5.1	Steel-fiber-reinforced-concrete crib member mix design. 156
5.2	Dimension of the steel-fiber-reinforced-concrete cribs tested. 157
7.1	Summary of the maximum loads and deformation for the supports evaluated. 216

CHAPTER 1 INTRODUCTION

A roof supporting system is one of the most important systems in underground mining. It may consist of various types of supports such as props, cribs, steel arches, powered supports, and roof bolts, among others. In this research, powered support and roof bolting are not included since these have been evaluated elsewhere.

Evaluation of underground supports needs to take account of several factors. Those factors include the mechanical behavior of the supports, the interaction between the support and the surrounding strata, the cost of the support, and the overall economics of using that support. Criteria are set up for evaluating the mechanical behavior of the supports, and a variety of supports are evaluated based on these criteria.

The first category considered consists of conventional wood supports including plain timber posts, timber cribs, and gallery sets. Tests were carried out to determine their mechanical behavior. The results from the tests are analyzed. The effects of moisture content, specific gravity, and defects on the mechanical properties of a timber support are also discussed. A finite element program has been modified to analyze the stress distribution of a round timber post under compression. The influence of eccentric loading and natural bow on the stress in the post are considered.

The second category to be considered is modified wood posts. This includes the Super Post, the Micon Yield Capsule post, and the Wedge Prop. The working mechanisms of these props together with factors affecting their performances are discussed. A testing program was

developed to evaluate these supports. Using the data gathered, recommendations are made on improving these props.

The third category consists of concrete supports. Included are the plain concrete crib, the steel-fiber-reinforced concrete crib, the donut crib, and the sandwich crib.

The final category of supports discussed in this thesis is steel supports which include the steel yielding prop, steel friction prop, and steel yielding arch. The structures and working principles of these supports are described and their mechanical properties are discussed.

Comparisons between the various supports are made on the basis of their mechanical behavior and cost. However, the cost is sometimes difficult to evaluate since, in some cases, only one kind of support can deal with the existing ground control problems and others will not work. In such a situation this particular kind of support is the only choice and the benefit of using it to solve the ground control problems can not be evaluated based only on its cost. The suitability of each kind of support under a certain roof conditions is also discussed, as is the future development of underground supports using wood and other materials.

CHAPTER 2 CRITERIA FOR EVALUATING UNDERGROUND
SUPPORTS

In order to assess a support, the following factors should be considered:

1. the mechanical behavior of the support, and
2. the cost of the support.

Of the two, the criterion for the cost of the support can be easily found since a lower cost is always favored. On the contrary, the criteria for the mechanical behavior are difficult to establish due to the great variety of strata conditions which require a support with a certain specific mechanical behavior.

A good support should effectively control the surrounding strata, and thus it is important to find out the relationships between the deflection of the surrounding strata and the resistance of the support. Based on these relationships, criteria for evaluating the mechanical behaviors of supports can be established. Two kinds of relationships, hyperbolic and linear, are considered here.

2.1 Resistance-Deflection Relationship — Hyperbolic

The hyperbolic relationship is one of the well-known relationships between roof deflection and the resistance of the roof support. This relationship was established mainly on a basis of experimentation and underground observation. Although some researchers try to verify it theoretically, the theories that they apply are not very convincing.

In early 1960's, experiments were conducted in the ground control laboratory of the China Institute of Mines and Technology in an effort to discover the relationship between roof deflection and the resistance of the roof support (Qian, 1983). It was found that the relationship is hyperbolic. The results are shown in figure 2.1.

In Russia, tests were performed in a longwall face (Qian, 1983). The seam height of the face was between 2.3 (7.5) and 2.5 meters (8.5 feet), and the dip angle of the seam was between 2 and 3 degrees. The immediate roof consisted of sandstone and its height was 5 meters (16.4 feet). The compressive strength of the immediate roof was 730 kg/cm^2 (10384 psi). The stratum above the immediate roof was also sandstone, but its density was higher and its compressive strength was between 810 (11522) and 826 kg/cm^2 (11750 psi). The supports used were powered supports. The test was performed in such a way that, as the working resistance of the support was adjusted, the deflection of the roof was recorded. The test results are shown in figure 2.2(a), the R-D curves under normal circumstance, and figure 2.2(b), the R-D curve under periodic weighting. According to the Russians, these curves are hyperbolic. The curves can be divided into three sections. In the first section, slightly decreasing the resistance will result in significant roof deflection. In the third section, the roof deflection decreases only slightly when the resistance increases. The second section is in transition between the first and the third. In figure 2.2(b), for example, when the resistance changes from 59 to 50 tons, the roof deflection increases by more than 200 mm (7.87 inches), but when resistance decreases from 125 to 100 tons, the deflection only increases by 21 mm (0.83 inches). Therefore, in this

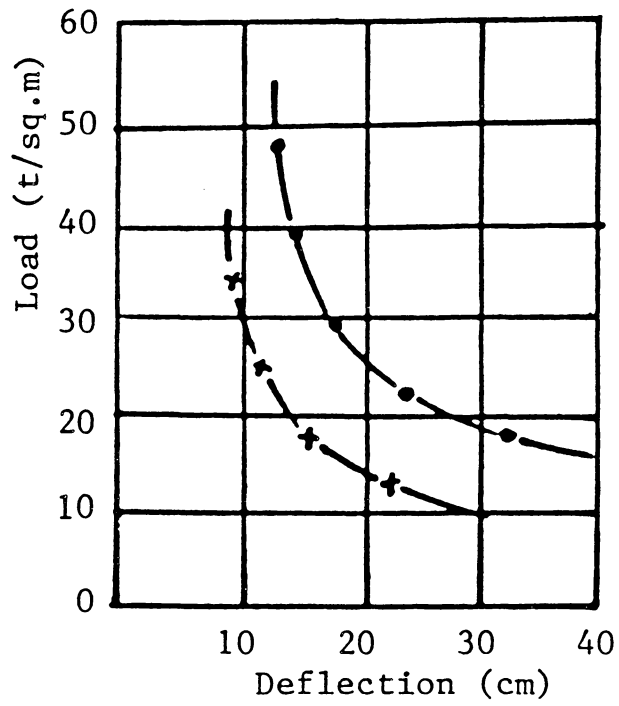
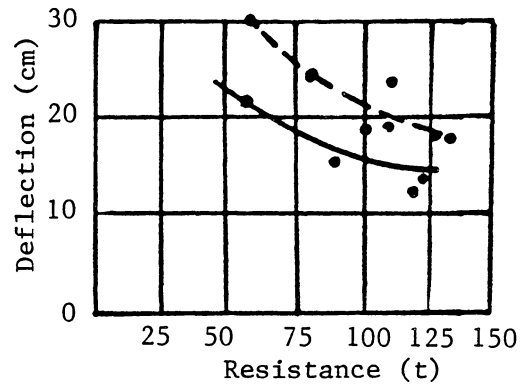
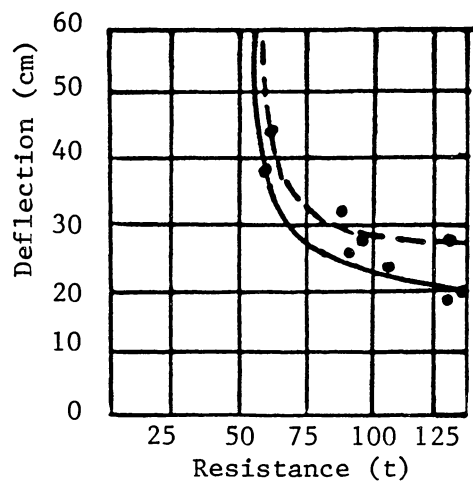


Figure 2.1 Hyperbolic Resistance-Deflection relations obtained from laboratory experiments. (Qian, 1983)



(a) Under normal condition



(b) During periodic weighting

Figure 2.2 Hyperbolic Resistance-Deflection relations obtained from underground testing. (Qian, 1983)

particular case the resistance of the support can not be less than 59 tons since the low resistance will result in significant roof deflection. On the other hand, it is unwise to have a support resistance of more than 100 tons because the high resistance means more cost for the support and the roof deflection will not substantially change.

In addition to the hyperbolic curve, other similar relationships also exist between the roof deflection and the resistance of the support. Figure 2.3 shows some non-hyperbolic curves obtained by different researchers.

Although many experiments and underground observations indicate that the R-D relationship is hyperbolic, this result is seldom obtained by analytical methods. Song (1982) proposed a model as shown in figure 2.4(a). He calls the lower part of the roof, which collapses after the face advances, the immediate roof, and the upper portion of the roof, which affects the load on the support and can transmit force horizontally, the transmitting beam.

The R-D relationship can be derived from figures 2.4(a) and (b). At the beginning, the immediate roof is in the horizontal position and it deflects under the load of the transmitting beams Q and its own weight G. When the deflection increases to Δh_i , the immediate roof reaches an equilibrium state due to the resistance of the support. From statics:

$$\sum M_o = 0$$

$$R_{zi} \frac{l_k}{2} = G \frac{l_z}{2} \cos\theta + Q l_Q$$

since $G = m_z l_z r_z$, and $\theta = \tan^{-1}(\Delta h_i / l_k)$

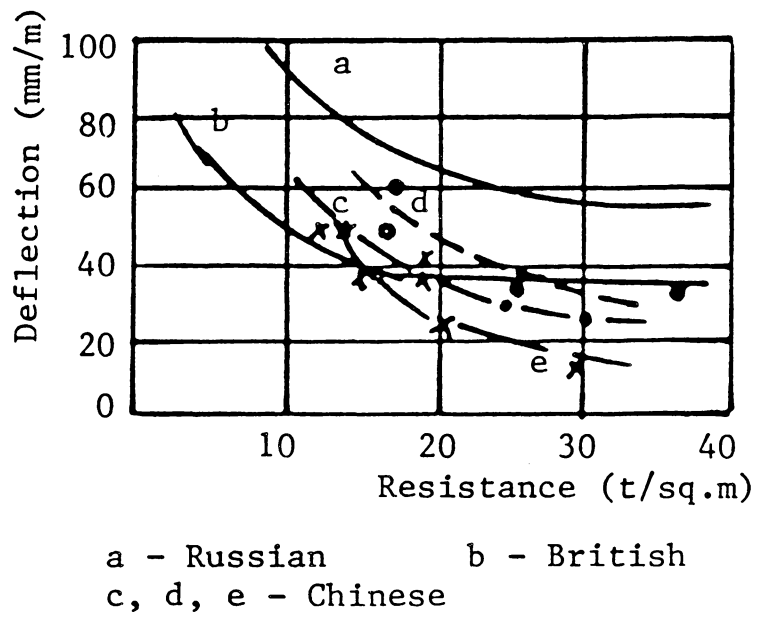


Figure 2.3 Resistance-Deflection relationships similar to a hyperbolic curve. (Qian, 1983)

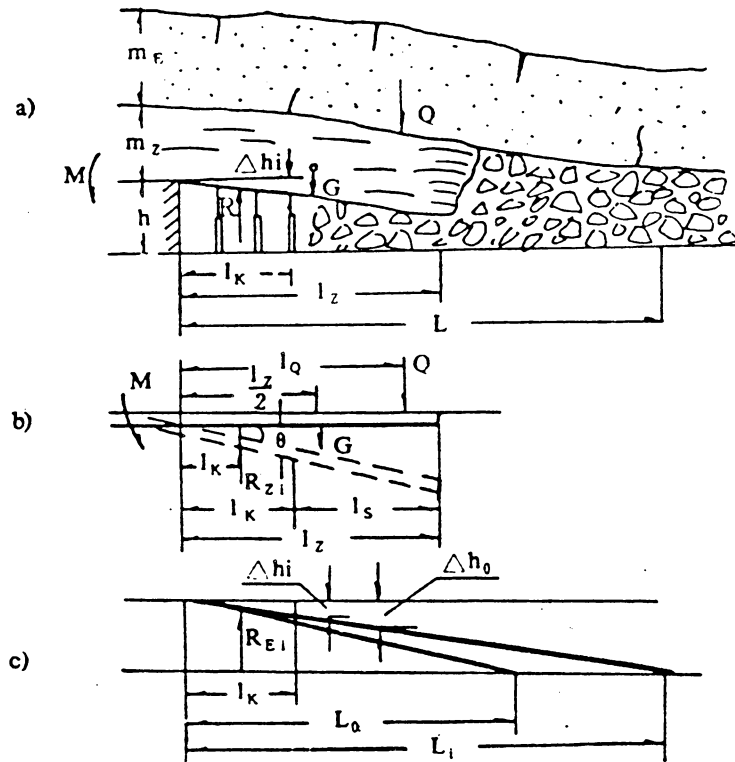


Figure 2.4 Model for deriving the hyperbolic Resistance-Deflection relationship. (Song, 1982)

$$R_{zi} = \frac{m_z l_z^2 r_z}{l_k} \cos\left(\tan^{-1} \frac{\Delta h_i}{l_k}\right) + \frac{2Ql_q}{l_k} \quad (2.1)$$

where R_{zi} = the resistance of the support (ton),

l_k = the width of the supporting area (ft.),

m_z = the thickness of the immediate roof (ft.),

r_z = the density of the immediate roof (t/ft.³),

l_z = the total length of the hanging part of the immediate roof (ft.),

Q = the resulting force of the transmitting beam on the immediate roof (ton),

l_q = the distance between force Q and the face line (ft.).

Q can be expressed as:

$$Q = \frac{m_E r_E L_i}{K_T} \quad (2.2)$$

where m_E = the thickness of the transmitting beam (ft.),

r_E = the density of the transmitting beam (t/ft.³),

L_i = the length of the transmitting beam (ft.),

K_T = the transmitting coefficient.

From figure 2.4(c)

$$L_i = \frac{\Delta h_o}{\Delta h_i} L_o \quad (2.3)$$

Substituting equations 2.2 and 2.3 into equation 2.1, the following equation is obtained:

$$R_{zi} = \frac{m_z l_z^2 r_z}{l_k} \cos\left(\tan^{-1} \frac{\Delta h_i}{l_k}\right) + \frac{2l_q m_E r_E \Delta h_o}{l_k K_T \Delta h_i} L_o \quad (2.4)$$

where Δh_o = the final deflection of the roof (in.),

L_o = the length of the transmitting beam when the deflection of the roof is Δh_o (ft.),

Δh_i = the deflection of the roof (in.).

In practice, $\frac{\Delta h_i}{l_k}$ is very small, and $\cos(\tan^{-1} \frac{\Delta h_i}{l_k}) = 1$.

let
$$A = \frac{m r l^2}{z z z} \quad \text{and}$$

$$B = \frac{2 l^m Q E E \Delta h_o L_o}{l_k K_T}$$

Then
$$R_{zi} = A + \frac{B}{\Delta h_i} \quad (2.5)$$

where A and B are constants. The relationship between R_{zi} and Δh_i , expressed in equation 2.5, is hyperbolic. Equation 2.5 coincides with experimental results. However two assumptions of Song's model lower the value of equation 2.5. One is the synchronous deflection assumption which assumes that the transmitting beam and the immediate roof have the same deflection. Another is the straight line assumption which assumes that the contour of the roof keeps straight as the roof deflects. Satisfactory explanation of the hyperbolic R-D relationship is probably another task for future ground control researchers.

2.2 Resistance-Deflection Relationship — Linear

This relationship is based on the theory of mechanics. The roof is viewed as a semi-infinite beam and the coal seam is regarded as an

elastic foundation. The relationship shows that the deflection of the roof decreases linearly as the resistance of the support increases. Underground observations of roof deflection correspond very well to the theoretical results, indicating that the assumption made in deriving the relationship is reasonable.

From advanced mechanics of materials (Cook, 1985), it is known that the deflection of the infinite beam shown in figure 2.5 is:

$$y = \frac{P\beta}{2k} e^{-\beta x} (\cos\beta x + \sin\beta x) \quad (2.6)$$

where y = the deflection of the infinite beam on elastic foundation (in.),

P = the concentrated force acting on the beam (lb.),

k = the foundation modulus indicating the reaction per unit length when the deflection is a unit (psi),

$$\beta = \sqrt{k/(4EJ_z)}$$

where E = the Young's modulus of the beam (psi),

J_z = the moment of inertia of the beam cross-section to its neutral axis (in.⁴),

x = the distance between the concentrated force and the point where the deflection is y (in).

For a linearly distributed load as shown in figure 2.6, the deflection of the beam at point A can be obtained by integration. Suppose that A is inside the load range and it divides the length of the distribution L into two sections, c and b . In section c the force acting on the beam at the point a distance x_2 from point A is $(b+x_2)qdx_2/L$, and it causes a deflection of

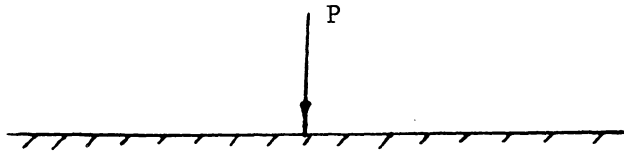


Figure 2.5 Concentrated force on an infinite beam on an elastic foundation.

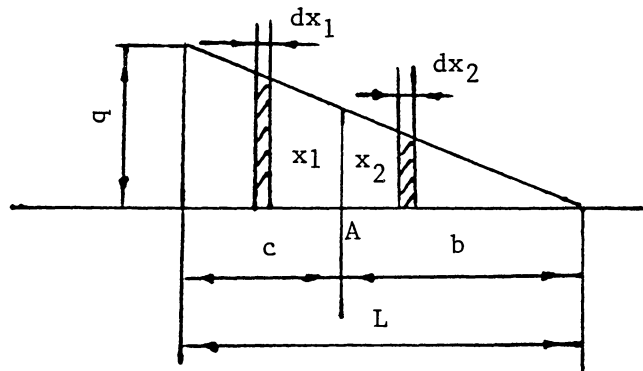


Figure 2.6 Linearly distributed load on the infinite beam on elastic foundation.

$$\frac{(b+x_2)q\beta}{2Lk} e^{-\beta x_2} (\cos\beta x_2 + \sin\beta x_2) dx_2$$

at point A. Thus the deflection at point A caused by the total load in section c is:

$$\int_0^c \frac{(b+x_2)q\beta}{2Lk} e^{-\beta x_2} (\cos\beta x_2 + \sin\beta x_2) dx_2.$$

Similarly, in section c, the force acting on the beam at the point a distance x_1 from point A is $(b-x_1)qdx_1/L$, and it causes a deflection of

$$\frac{(b-x_1)q\beta}{2Lk} e^{-\beta x_1} (\cos\beta x_1 + \sin\beta x_1) dx_1$$

at point A. Thus the deflection at point A caused by the total load in section b is:

$$\int_0^b \frac{(b-x_1)q\beta}{2Lk} e^{-\beta x_1} (\cos\beta x_1 + \sin\beta x_1) dx_1.$$

The total deflection at point A caused by the entire linearly distributed load is:

$$y = \int_0^c \frac{(b+x_2)q\beta}{2Lk} e^{-\beta x_2} (\cos\beta x_2 + \sin\beta x_2) dx_2 + \int_0^b \frac{(b-x_1)q\beta}{2Lk} e^{-\beta x_1} (\cos\beta x_1 + \sin\beta x_1) dx_1.$$

After integration,

$$y = \frac{q}{4\beta kL} \{ [4\beta b + e^{-\beta c} (\sin\beta c - \cos\beta c) - e^{-\beta b} (\sin\beta b - \cos\beta b)] - 2\beta(b+c)e^{-\beta c} \cos\beta c \}. \quad (2.7)$$

Let $\Phi(\beta c) = -e^{\beta c} (\sin\beta c - \cos\beta c)$

$$\Phi(\beta b) = -e^{\beta b}(\sin\beta b - \cos\beta b)$$

$$\theta(\beta c) = e^{-\beta c} \cos\beta c.$$

Then
$$y = \frac{q}{4kL\beta} [4\beta b - \Phi(\beta c) + \Phi(\beta b) - 2\beta L\theta(\beta c)]. \quad (2.8)$$

If point A is outside the distributed load, as shown in figure 2.7, the deflection at point A caused by the load increment $xqdx/L$ a distance (x_0+x) from point A is:

$$\frac{xq\beta}{2kL} e^{-\beta(x+x_0)} [\cos(x+x_0) + \sin(x+x_0)] dx.$$

The deflection at point A caused by the entire distributed load is:

$$\begin{aligned} y &= \int_0^L \frac{xq\beta}{2kL} e^{-\beta(x+x_0)} [\cos(x+x_0) + \sin(x+x_0)] dx \\ &= \frac{q}{4k\beta L} \{-2\beta L e^{-\beta(x_0+L)} \cos(x_0+L) + \\ &\quad + e^{-\beta(x_0+L)} [\sin\beta(x_0+L) - \cos\beta(x_0+L)] - \\ &\quad - e^{-\beta x_0} (\sin\beta x_0 - \cos\beta x_0)\}. \end{aligned} \quad (2.9)$$

Let
$$\begin{aligned} \Phi(\beta x_0) &= -e^{-\beta x_0} (\sin\beta x_0 - \cos\beta x_0) \\ \Phi[\beta(x_0+L)] &= -e^{-\beta(x_0+L)} [\sin\beta(x_0+L) - \cos\beta(x_0+L)] \\ \theta[\beta(x_0+L)] &= e^{-\beta(x_0+L)} \cos(x_0+L). \end{aligned}$$

Then
$$y = -\frac{q}{4k\beta L} \{2\beta L \theta[\beta(x_0+L)] + \Phi[\beta(x_0+L)] - \Phi(\beta x_0)\}. \quad (2.10)$$

So far, the deflections of point A in two different locations, namely inside and outside the range of the distributed load, have been discussed. The two cases can be put together under the same coordinate system as shown in figure 2.8. Comparing figures 2.6 and 2.7 with figure

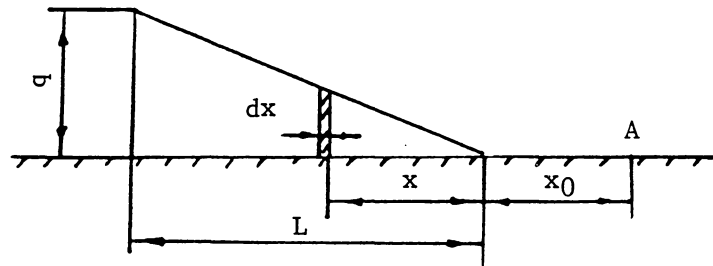


Figure 2.7 Point A outside the linearly distributed load.

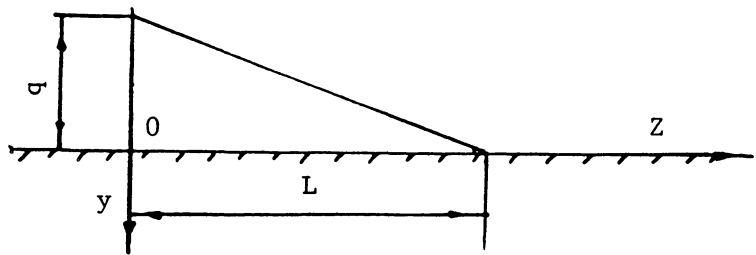


Figure 2.8. The coordinate system for roof deflection.

2.8, one can see that c and b in equation 2.7 can be replaced with z and $L-z$ respectively, and x_0 in equation 2.9 can be substituted by $z-L$. Thus for $z \geq 0$, the deflection of the infinite beam can be expressed as:

$$y = \begin{cases} \frac{q}{4kL\beta} [4\beta b - \Phi(\beta c) + \Phi(\beta b) - 2\beta L\theta(\beta c)] & 0 \leq z \leq L \\ \frac{q}{4k\beta L} \{2\beta L \theta[\beta(x_0+L)] + \Phi[\beta(x_0+L)] - \Phi(\beta x_0)\} & L \leq z \leq \infty. \end{cases} \quad (2.11)$$

In order to find out the deflection of a semi-infinite beam subjected to the same distributed load as mentioned previously, the moment and shear force at $z=0$ have to be known. From the mechanics of materials, it is known that the moment:

$$M = -EJ \frac{d^2 y}{dz^2}$$

and that the shear force:

$$P = \frac{dM}{dz}$$

In the domain of $0 \leq z \leq L$

$$\begin{aligned} M &= -EJ \frac{d^2 y}{dz^2} \\ &= -\frac{q}{8\beta^3} \{e^{-\beta(L-z)} [\cos\beta(L-z) + \sin\beta(L-z)] - \\ &\quad -e^{-\beta z} (\cos\beta z + \sin\beta z) - 2\beta L e^{\beta z} \sin\beta z\} \\ &= -\frac{q}{8\beta^3 L} \{\phi[\beta(L-z)] - \phi(\beta z) - 2\beta L \zeta(\beta z)\} \end{aligned} \quad (2.12)$$

and

$$\begin{aligned}
 P &= -\frac{q}{4\beta^2 L} [e^{-\beta(L-z)} \sin\beta(L-z) + e^{-\beta z} \sin\beta z + \\
 &\quad + \beta L e^{-\beta z} (\sin\beta z - \cos\beta z)] \\
 &= -\frac{q}{4\beta^2 L} \{ \zeta[\beta(L-z)] + \zeta(\beta z) - \beta L \Phi(\beta z) \}. \quad (2.13)
 \end{aligned}$$

At $z=0$

$$M'_0 = -\frac{q}{8\beta^3 L} [\phi(\beta L) - 1] \quad (2.14)$$

and

$$P'_0 = -\frac{q}{4\beta^2 L} [\zeta(\beta L) - \beta L]. \quad (2.15)$$

Thus the deflection of a semi-infinite beam subjected to linearly distributed load can be obtained.

To find out the deflection, superposition principle is applied. The load shown in figure 2.9(a) can be thought of as the sum of the loads in figures 2.9(b) and 2.9(c). The deflection of the beam in figure 2.9(b) is equal to that of the infinite beam subjected only to linearly distributed load and the deflection of the beam in figure 2.9(c) can be expressed as:

$$y = \frac{2\beta}{k} \{ P_0 \theta(\beta z) - \beta M_0 [\theta(\beta z) - \zeta(\beta z)] \} \quad (2.16)$$

where

$$P_0 = -P'_0$$

$$M_0 = -M'_0$$

M'_0 = the bending moment of the infinite beam at $z=0$ when subjected to a linearly distributed load (lb.in),

P'_0 = the shear force of the infinite beam at $z=0$ when subjected to a linearly distributed load (lb).

By superposing the deflection of the beam in figure 2.9(c) on that in

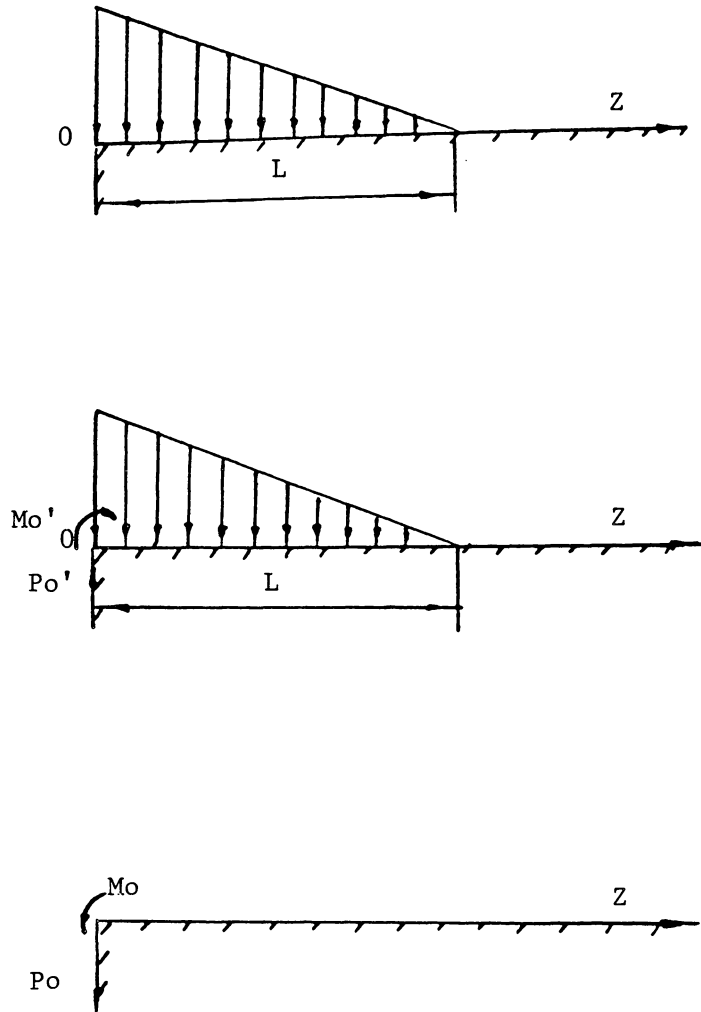


Figure 2.9. Model for finding out the deflection of the semi-infinite beam on an elastic foundation.

figure 2.9(b), the deflection of semi-infinite beam subjected to linearly distributed load is obtained:

$$y = \begin{cases} \frac{q}{4k\beta L} \{4\beta(L-z) - \Phi(\beta z) + \Phi[\beta(L-z)] + \\ + 2[\zeta(\beta L) - 2\beta L]\theta(\beta z) - [\phi(\beta L) - 1][\theta(\beta z) - \zeta(\beta z)]\} & 0 \leq z \leq L \\ \frac{q}{4k\beta L} \{2[\zeta(\beta L) - 2\beta L]\theta(\beta z) - \Phi(\beta z) + \\ + \Phi[\beta(z-L)] - [\phi(\beta L) - 1][\theta(\beta z) - \zeta(\beta z)]\} & L \leq z \leq \infty \end{cases} \quad (2.17)$$

where q = the peak value of the load distribution (lb/in),

L = the length of the distribution (in.).

Thus, all the background information needed is known. The task remaining is to set up the model and use the background information to obtain the R-D relationship.

Figure 2.10(a) is the model used to derive the deflection of the roof. The actual distribution of the abutment pressure on the immediate roof is indicated by the dotted line, and it is not a linear distribution. For convenience the distribution is assumed linear, as indicated by the solid line in figure 2.10(a). According to the results from the abutment pressure research (Qian, 1983), the peak of the distribution is at the plane which divides the coal seam into an elastic zone and a nonelastic zone. If the coal seam in the elastic zone is taken as an elastic foundation and the immediate roof as a semi-infinite beam,

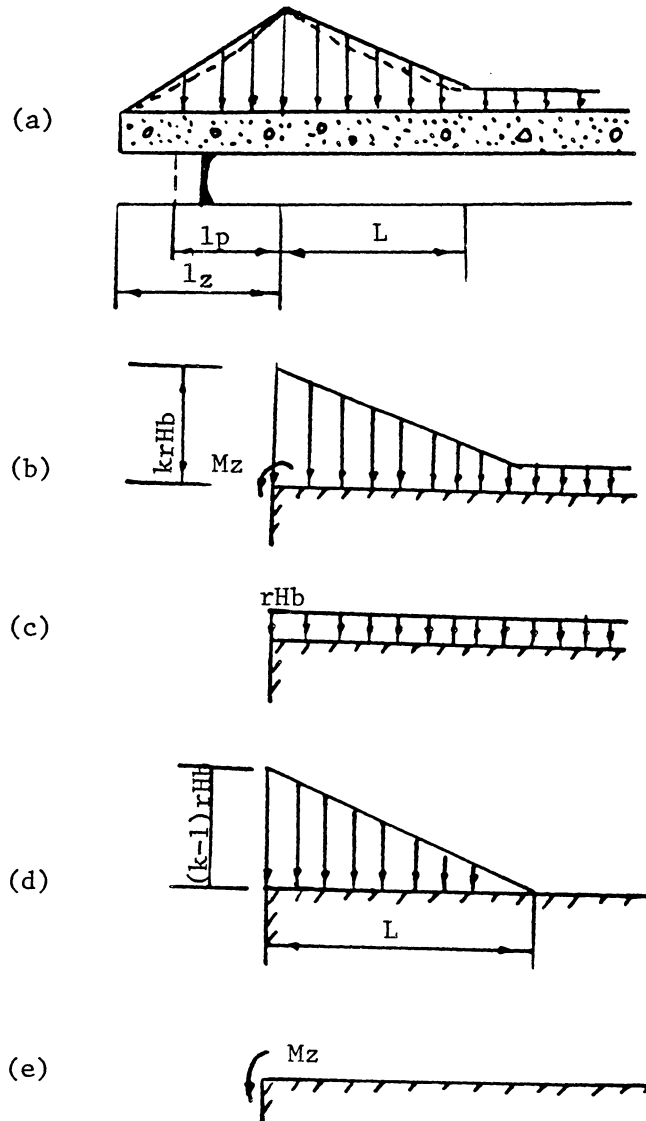


Figure 2.10 Model for calculating roof deflection.

then a model of a semi-infinite beam on an elastic foundation is set up, as shown in figure 2.10(b). Note that in this model the distributed load above the nonelastic zone and the resistance of the support are turned into a bending moment which can be expressed as:

$$M_z = \frac{KrHb}{6} l_z^2 - Pl_p \quad (2.18)$$

where K = stress concentration factor,
 r = the density of the overburden (lb/in.³),
 H = the thickness of the overburden (in.),
 P = the resistance of the support (lb),
 l_z = the length of the immediate roof in the nonelastic zone (in.),
 l_p = the distance of the support from the peak load (in.),
 b = the width of the beam (in.).

The load in the model shown in figure 2.10(b) consists of three parts, namely the uniformly distributed load in figure 2.10(c), the linearly distributed load in figure 2.10(d), and the bending moment in figure 2.10(e). The deflection caused by each part of the load can be calculated separately, and then the total deflection of the immediate roof can be obtained by superposition. However, the deflection due to the uniformly distributed load need not be taken account of since it occurred prior to the underground mining and it can not be measured underground. The deflection caused by the linearly distributed load can be expressed by equation 2.17, and the deflection due to the bending moment is:

$$y = \frac{2\beta^2}{k} \left[\frac{KrHb}{6} 1_z^2 - P1_p \right] [\theta(\beta z) - \zeta(\beta z)] \quad (2.19)$$

By adding equations 2.17 and 2.19 together, the deflection of the immediate roof is obtained:

$$y = \left\{ \begin{array}{l} \frac{q}{4k\beta L} \{4\beta(L-z) - \Phi(\beta z) + \Phi[\beta(L-z)] + \\ + 2[\zeta(\beta L) - 2\beta L]\theta(\beta z) - [\phi(\beta L) - 1][\theta(\beta z) - \zeta(\beta z)]\} \\ + \frac{2\beta^2}{k} \left[\frac{KrHb}{6} 1_z^2 - P1_p \right] [\theta(\beta z) - \zeta(\beta z)] \\ \hspace{15em} 0 \leq z \leq L \\ \\ \frac{q}{4k\beta L} \{2[\zeta(\beta L) - 2\beta L]\theta(\beta z) - \Phi(\beta z) + \\ + \Phi[\beta(z-L)] - [\phi(\beta L) - 1][\theta(\beta z) - \zeta(\beta z)]\} \\ + \frac{2\beta^2}{k} \left[\frac{KrHb}{6} 1_z^2 - P1_p \right] [\theta(\beta z) - \zeta(\beta z)] \\ \hspace{15em} L \leq z \leq \infty \end{array} \right. \quad (2.20)$$

It can be seen from equation 2.20 that the deflection of the immediate roof along the panel length is a periodic curve with the amplitude decaying gradually. There will be no negative deflection in a considerably large area around the face however, since the wavelength of the curve is very large. Figure 2.11 shows both the deflection calculated from equation 2.20 and that obtained from underground observations. The two curves agree with each other, suggesting that the assumption made for deriving equation 2.20 may be valid. Equation 2.20

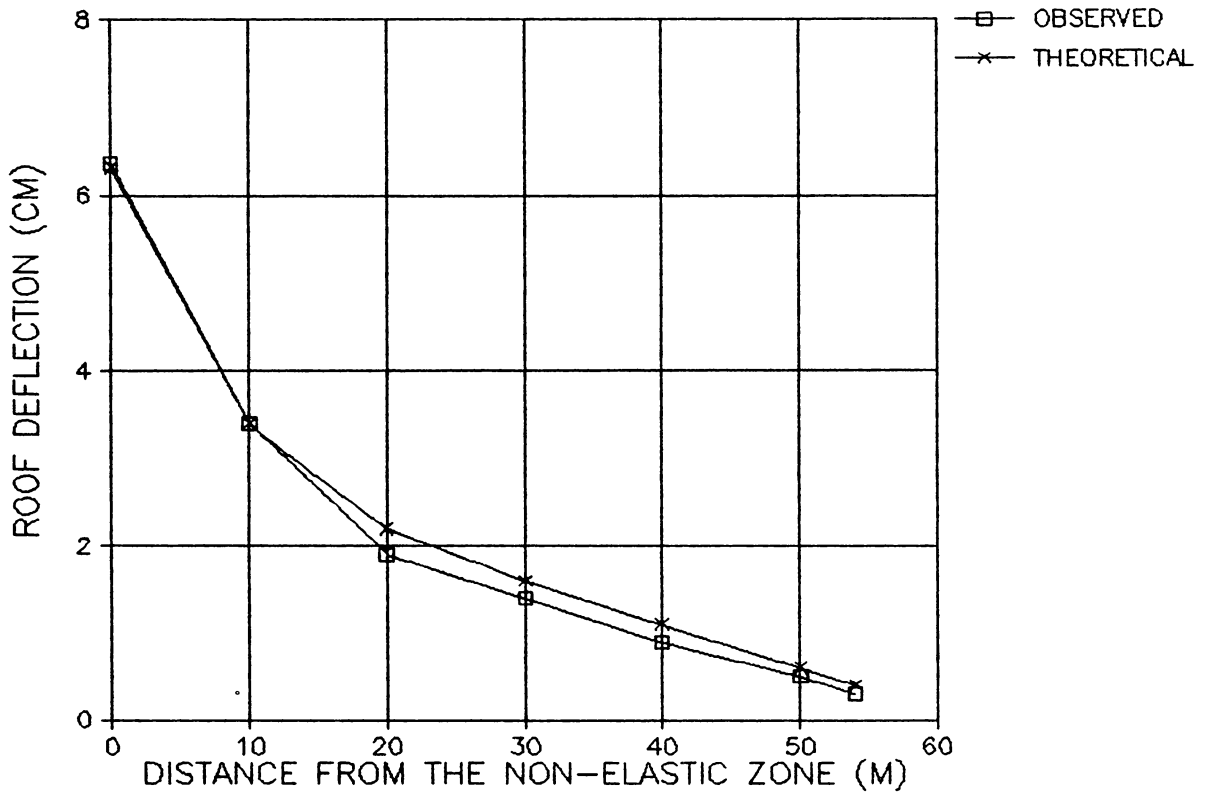


Figure 2.11. Comparison between theoretical and measured deflection.

shows a linear relationship between the resistance of the support and the deflection of the immediate roof.

2.3 Criteria Based on The Resistance-Deflection Relationship

As mentioned earlier in this chapter, the hyperbolic R-D curve can be divided into three sections which are indicated in figure 2.12. The first section is defined by $0 < P \leq P_1$, the second is between P_1 and P_2 , and the third is in the domain of $P > P_2$. In the first section, slightly decreasing the resistance of the support will result in a significant increase in roof deflection. Therefore the resistance can not be allowed to be lower than P_1 in order to limit the roof deflection. In the third section, on the other hand, a significant increase in the support resistance only slightly reduces the roof deflection, and thus it does not make much sense to increase the support resistance beyond P_2 . The second section is the range in which the support resistance can be changed in accordance with the deflection control requirements.

According to the above analysis of the hyperbolic relationship, a good support should have following characteristics (Blight, 1978):

1. The slope of the initial portion of the load-deformation curve should be as steep as possible. Ideally, it should approach the corresponding characteristic for the intact rock.

2. A definite, predictable yield point should be reached, after which the support should behave in such a way that its load increases slowly as it deforms.

Based on the linear relationship, the support may have a constant

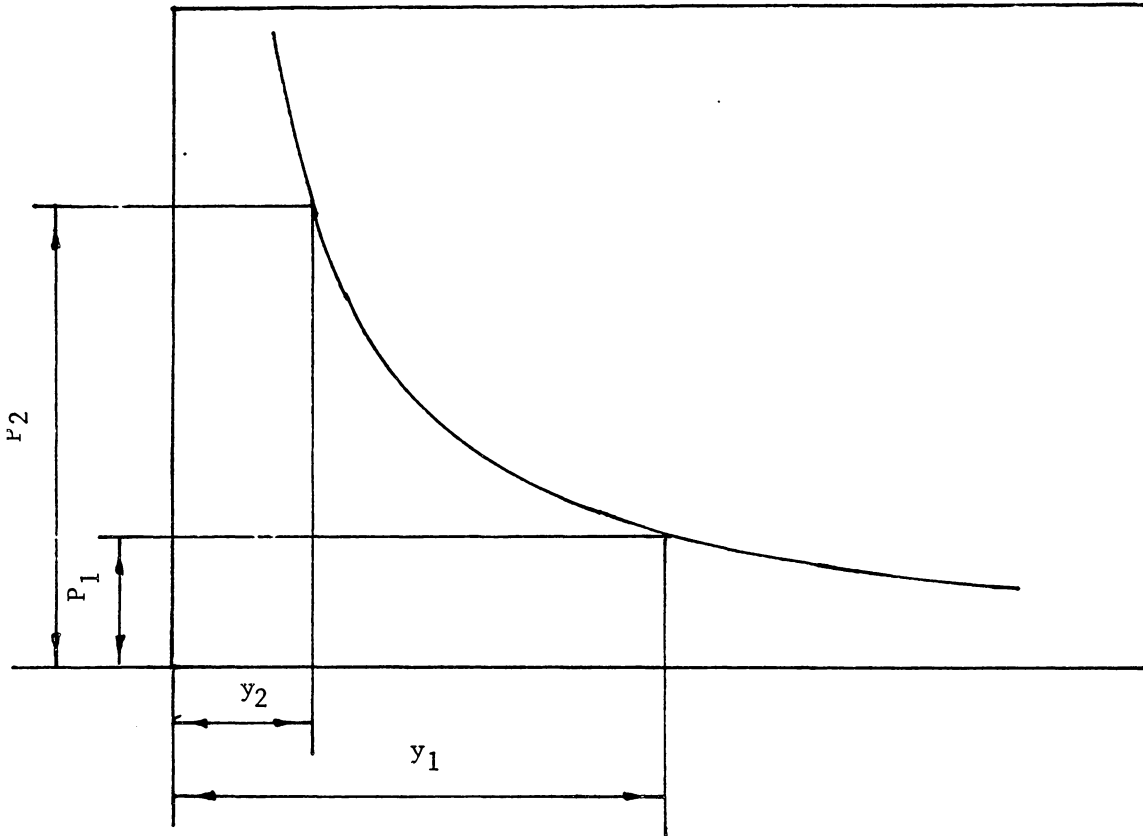


Figure 2.12. Three sections of the hyperbolic curve.

stiffness from beginning to end. The value of stiffness depends on what kind of roof the support is going to control.

From equation 2.20 it can be seen that the deflection of the roof decreases linearly as the resistance increases. However, the effect of the support resistance on the deflection of the roof may not be significant, since, in some cases, the abutment pressure is a dominant factor. Depending on the magnitude of the abutment pressure, the following can be said about the stiffness of the support:

1. If the abutment pressure dominates, then the resistance of the support is of little significance, or in other words, the deflection of the roof is non-resistable. In this case the function of the support is to prevent local roof falls, and thus the support should be yieldable enough to accommodate the non-resistable deflection and at the same time be stiff enough to prevent local delamination and cracking.

2. If the abutment pressure is not very large and the roof is flexible, the support can effectively control the deflection. In this case the stiffness of the support can be determined according to the deflection control requirements.

CHAPTER 3 CONVENTIONAL TIMBER SUPPORT

Timber was the most important material for support in mining until the end of the Second World War (Biron, 1983). Since then steel has become the primary material used for mine support. However, due to its economy and availability, timber is still widely used for entry supports and as reinforced support in mining areas where the roof or floor deteriorates. Figure 3.1 shows the use of timber, in the form of both timber posts and cribs, for roof control in room-and-pillar mining. In 1979, United States underground coal mines consumed more than 34 million cubic feet of timber, and the amounts, by categories, are listed in Table 3.1 (Stone, 1985). In South Africa, timber mine supports are the third largest consumer of round wood, using 27 percent of the total supply (Sorfa, 1985). Timber supports are more widely used in some developing countries which can not afford to buy expensive steel supports.

In this chapter, various factors affecting the mechanical behavior of timber supports are discussed. A finite element program is modified to analyze the stress distribution in timber posts. Statistical methods are utilized to analyze the test results, and principles of mechanics are used to explain various phenomena associated with the timber supports used underground.

In order to assess the mechanical behavior of timber supports, it is necessary to review some of the basic knowledge about wood.

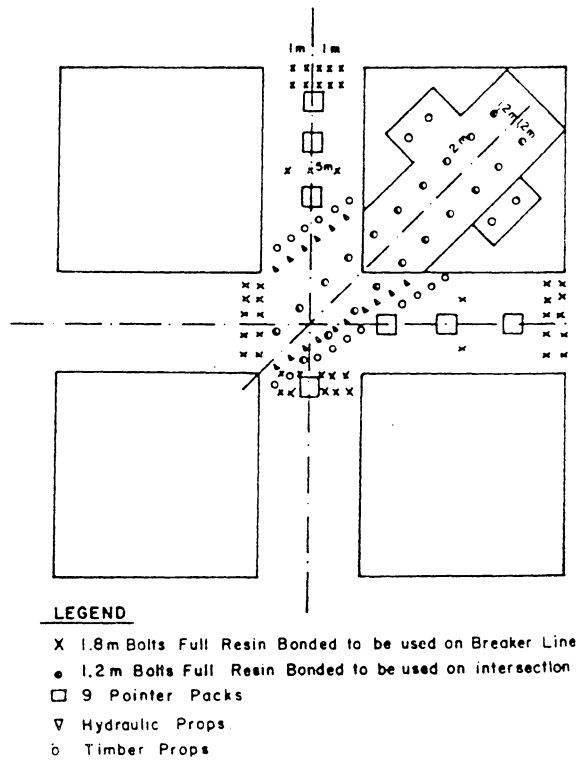


Figure 3.1. A ground control plan showing the use of timber supports. (Flint, 1984)

Table 3.1 Summary of Wood Products Used in Underground Coal Mines by Category in 1979 (Stone, 1985)

Category	Amount (Mft ³)
Round props	8,408.2
Sawn props	3,072.0
Split props	781.3
Lagging	250.1
Crib blocks	3,815.5
Headers	2,016.7
Crossbars	14,438.5
Ties	848.9
Wedges	6.3
Miscellaneous	677.9
Total	34,225.4

3.1 Some Wood Terminology

Since mining engineers may not be very familiar with the wood science terminology, some of the most commonly used terms are briefly reviewed here.

Softwood and hardwood

Trees are classified into two major categories, called softwoods (gymnosperms) and hardwoods (angiosperms) (Thomas, 1979). The botanical basis for classification is whether or not the tree seed is naked, as in softwoods, or covered, as in hardwoods. A more familiar classification, which, with some exception is valid, is based on retention of leaves by softwoods or the annual shedding of leaves by hardwoods. Thus softwoods are often referred to as evergreen trees and hardwoods as deciduous trees. Another classification based on leaves describes hardwoods as broad leaved trees and softwoods as narrow leaved trees. Anatomically, the major difference between the two categories of wood is the presence of vessels in the hardwoods. Vessels are structures created exclusively for conduction of water. Softwoods lack vessels but have cells called longitudinal tracheids which perform both the conduction and support roles.

The terms softwood and hardwood are not to be taken as a measure of hardness since some hardwoods are softer than many softwoods. For the commercially important domestic woods, the average specific gravity for softwoods is 0.41 with a range of 0.29 to 0.60. Hardwoods average 0.50

and vary from 0.32 to 0.81.

Sapwood and heartwood

From the end view of a tree stem or log, it can be seen that the central wood portion of the stem is considerably darker in color than the part adjacent to the bark. The light-colored wood is called sapwood and the dark-colored wood is designated heartwood (Thomas, 1979). The difference in coloration is due to the production and secretion of substances which are by products of the death of food-storage cells. As new wood, that is sapwood, is formed adjacent to the bark at the outside of the tree stem, additional interior sapwood adjacent to the heartwood zone is converted to heartwood. Some trees do not form discolored heartwood, thus recognition of heartwood based on color is not always possible. Trees which lack discolored heartwood are referred as sapwood trees. In many woods the discoloring substances are toxic to insects and fungi which decay wood. Hence heartwood often possesses greater resistance to decay than sapwood.

The proportion of sapwood to heartwood is variable. The variation ranges from trees composed almost entirely of heartwood with only a very narrow band of sapwood to those with only a small amount of heartwood.

Growth ring, earlywood and latewood

During each growing season, a new layer of wood is formed around the tree stem. These new layers are called growth rings or annual increments

(Thomas, 1979). The growth rings are distinguishable due to differences in the wood produced early as opposed to late in the growing season. The wood produced early is called earlywood or spring wood, and that formed late in the growing season is referred to as latewood or summerwood. Earlywood is lighter in color than latewood. The color separation is due primarily to differences in the structure of earlywood and latewood cells. The earlywood cells have a relatively large diameter, a thin wall and a large open center. The latewood cells have a smaller diameter, thicker wall and smaller open center. As a result, the latewood of softwoods and ring-porous hardwoods has a higher density than earlywood. Since the wood substance in earlywood and latewood is basically the same, the higher density of the latewood means that there is more material per unit volume that can resist force, thus the strength and stiffness of the latewood are much greater than that of the earlywood.

Moisture content, green wood and fiber saturation point

Moisture content of wood is defined as the weight of water in wood expressed as a fraction, usually as a percentage of the weight of oven-dry wood (Forest Products Lab., 1974). Strength, shrinkage, weight and other properties depend upon the moisture content of wood.

In trees moisture content may range from about 30 percent to more than 200 percent of the weight of oven-dry wood substance. Moisture content of the sapwood portion is usually high. Heartwood moisture content may be much less than sapwood moisture content in some species, although it is greater in others.

Moisture can exist in wood as water or water vapor in cell lumens (cavities). Green wood is often defined as wood in which the cell walls are completely saturated with water. However, green wood usually contains additional water in the lumens. The moisture content at which cell walls are completely saturated but no water exists in cell cavities is called the fiber saturation point. The fiber saturation point of wood averages about 30 percent moisture content, but individual pieces of wood may vary by several percentage points from that value.

The fiber saturation point also is considered as the moisture content below which the physical and mechanical properties of wood begin to change.

3.2 Brief Review of Wood Structure and Properties

Micro-structure of wood

Wood is a natural material of biological origin (Haygreen, 1982). It is a complex material not only because it is made up of many types of cells which vary in regard to size and cell wall thickness but also because of the physical structure of the cell wall. The consistent orientations of the cell and of the major molecular components in the cell wall result in a material with distinctly anisotropic properties.

The typical wood cell can be thought of being similar to a drinking straw in shape. It is hollow, although the ends are closed, it is many times as long as it is wide and often the cell wall is relatively thin. The majority of the cells in the wood are oriented in the longitudinal

direction. It is these longitudinal cells which determine, for the most part, the properties of wood.

There is another kind of cell, called the ray cell, which lies in tissues extending from the outer surface of the tree toward the pith. These tissues called rays are commonly only one or two cells thick in softwoods but may be many cells thick in hardwood. The percent of the total volume of wood which is made up of ray tissues varies between species from about 3 to 30 percent. Softwood species characteristically have a relatively low percent of ray tissues, 3 to 11 percent, while in hardwoods the percentage of ray volume may vary from about 5 percent to 30 percent. The rays have relatively high strength and stiffness in the radial direction, so that the rays, even though they may in volume constitute only a small percentage of the total, act like reinforcing rods in the radial direction.

Some physical properties of wood

Wood possesses many physical properties. It is not the author's intention to list all those properties. Emphasis is placed only on the properties which may affect the in-situ performance of the timber support.

Among these physical properties of concern, density or specific gravity is the most important. Wood density is often calculated based on the water-free mass and on the volume which includes the water in the cell walls. However, the density of wood is also calculated including the water as part of the mass. Thus water enters as a factor

affecting wood density. Therefore, whenever wood density is discussed, the basis for calculation should be stated. It can be based on either dry or total mass (Haygreen, 1982).

Because of the ambiguity of the basis for calculating the density of wood, it is much better to use specific gravity as the indicator of the mass per volume. It is a recognized standard in the wood product field that specific gravity is always based on the oven-dry (moisture free) weight. The volume used to determine the specific gravity is that at the moisture content of interest. For example, if the oven-dry specific gravity is desired, then the volume at 0 percent moisture content is used. When the green specific gravity is being calculated, the volume must be measured before any shrinkage has taken place.

Specific gravity is one of the most important physical characteristics of wood. Almost all the mechanical properties of wood are closely related to specific gravity. Table 3.2 shows the relationships between the specific gravity and various mechanical properties of wood. If the specific gravity is known, a reasonable estimate of clear wood strength can be made using Table 3.2, even if the species is unknown.

Moisture content is another important physical property of wood. It affects the mechanical properties of wood when below the fiber saturation point, as discussed in Section 3.1.

Shrinkage is also an important physical property in terms of timber support performance. Shrinkage of timber cribs can cause serious ground control problems since very tight cribs can relax due to shrinkage.

Wood is dimensionally stable when the moisture content is above the

Table 3.2 Functions Relating Mechanical Properties to Specific Gravity of clear, Straight-grained Wood (Forest Products Lab., 1974)

	Specific gravity-strength relation	
	Green wood	Air-dry wood (12% MC)
Static bending:		
Fiber stress at proportional limit p.s.i.	10,200G ^{1.25}	16,700G ^{1.25}
Modulus of elasticity million p.s.i.	2.36G	2.8G
Modulus of rupture p.s.i.	17,600G ^{1.25}	25,700G ^{1.25}
Work to maximum load in.-lb. per cu. in.	35.6G ^{1.75}	32.4G ^{1.75}
Total work in.-lb. per cu. in.	103G ²	72.7G ²
Impact bending, height of drop causing complete failure in.	114G ^{1.75}	94.6G ^{1.75}
Compression parallel to grain:		
Fiber stress at proportional limit p.s.i.	5,250G	8,750G
Modulus of elasticity million p.s.i.	2.91G	3.38G
Maximum crushing strength p.s.i.	6,730G	12,200G
Compression perpendicular to grain, fiber stress at proportion p.s.i.	3,000G ^{2.25}	4,630G ^{2.25}
Hardness:		
End lb.	3,740G ^{2.25}	4,800G ^{2.25}
Side lb.	3,420G ^{2.25}	3,770G ^{2.25}

Note: G represents the specific gravity of oven-dry wood, based on the volume at the moisture condition indicated.

fiber saturation point (Forest Products Lab., 1974). Wood changes dimension as it gains or loses moisture below that point. It shrinks when losing moisture from the cell wall and swells when gaining moisture in the cell walls. This shrinking and swelling may result in warping, checking, splitting or other performance problems.

Wood possesses anisotropic shrinkage characteristics. It shrinks most in the direction of the annual growth rings (tangentially), about one-half as much across the rings (radially), and only slightly along the grain (longitudinally).

The shrinkage of wood is related to its moisture content. A formula is developed to estimate shrinkage from the green condition to any moisture content (Forest Products Lab., 1974):

$$S_m = S_0 \frac{30-m}{30} \quad (3.1)$$

where S_m = the shrinkage (in percent) from the green condition to moisture content m which is less than 30 percent,
 S_0 = the total shrinkage from green to oven-dry found in Wood Handbook.

In equation 3.1, if the moisture content at which shrinkage from the green condition begins is known to be different from 30% for a species, the shrinkage estimate can be improved by replacing 30% in the equation with the appropriate moisture content.

Some mechanical properties of wood

Wood can be described as an orthotropic material; that is, it has unique and independent mechanical properties in the directions of three mutually perpendicular axes - longitudinal, radial and tangential (Forest Products Lab., 1974). The longitudinal axis (L) is parallel to the grain; the radial axis (R) is normal to the growth rings (perpendicular to the grain in a radial direction); the tangential direction axis (T) is tangent to the growth rings, as show in figure 3.2.

In an isotropic material, i.e, a material where properties are the same regardless of direction, three elastic constants are used to describe the strain-stress relationship (Schniewind, 1979). They are the modulus of elasticity E, the shear modulus G, and the Poisson's ratio μ . Among the three constants, only E and μ are mutually independent, and G is related to E and μ . As an orthotropic material, wood has more elastic constants than the isotropic materials. There are three moduli of elasticity, one for each of the principal directions of wood; three shear moduli, one for each of the principal planes; and six Poisson's ratios, two for each principal direction. For instance, if the stress is in the longitudinal direction, there will be lateral strains in both the radial and tangential directions, and each has its own Poisson's ratio. The elastic constants can be denoted as:

Moduli of elasticity: E_L, E_R, E_T

Shear moduli: G_{TR}, G_{RL}, G_{TL}

Poisson's Ratios: $\mu_{LT}, \mu_{TL}, \mu_{TR}, \mu_{RT}, \mu_{LR}, \mu_{RL}$.

The subscripts for E and G refer to the three principal directions in

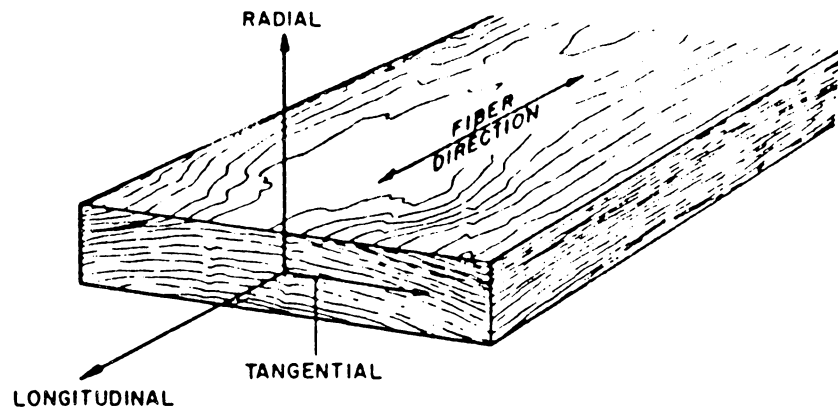


Figure 3.2. Three principal directions of wood.
(Forest Product Lab., 1974)

wood. For the Poisson's ratios, the first subscript refers to the direction of the applied stress and the second subscript to the direction of lateral strain. The twelve constants can be reduced to nine independent constants by the following relationship (Schniewind, 1979):

$$\begin{aligned} \frac{\mu_{LT}}{E_L} &= \frac{\mu_{TL}}{E_T} \\ \frac{\mu_{TR}}{E_T} &= \frac{\mu_{RT}}{E_R} \quad \dots\dots(3.2) \\ \frac{\mu_{LR}}{E_L} &= \frac{\mu_{RL}}{E_R} \end{aligned}$$

The stress-strain relationship can be expressed as:

$$\begin{vmatrix} \epsilon_x \\ \epsilon_y \\ \epsilon_z \\ \epsilon_{xy} \\ \epsilon_{yz} \\ \epsilon_{zx} \end{vmatrix} = \begin{vmatrix} 1/E_L & -\mu_{RL}/E_R & -\mu_{TL}/E_T & 0 & 0 & 0 \\ -\mu_{LR}/E_L & 1/E_R & -\mu_{TR}/E_T & 0 & 0 & 0 \\ -\mu_{LT}/E_L & -\mu_{RT}/E_R & 1/E_T & 0 & 0 & 0 \\ 0 & 0 & 0 & 1/G_{LR} & 0 & 0 \\ 0 & 0 & 0 & 0 & 1/G_{RT} & 0 \\ 0 & 0 & 0 & 0 & 0 & 1/G_{TL} \end{vmatrix} \begin{vmatrix} \sigma_x \\ \sigma_y \\ \sigma_z \\ \tau_{xy} \\ \tau_{yz} \\ \tau_{zx} \end{vmatrix} \quad (3.3)$$

where x, y, and z directions coincide with the L, R, and T directions respectively. If the coordinates do not coincide with the principal directions in the wood structure, the stress and strain relationship will become more complex. For example, if a piece of lumber were to be cut such that the grain direction was not parallel to the edges of the piece, then for a deviation in the LR-plane alone, the modulus of elasticity at an angle θ to the longitudinal direction would be given by (Bodig, 1982):

$$\frac{1}{E_x} = \frac{1}{E_L} \cos^4 \theta + \frac{1}{E_R} \sin^4 \theta + \cos^2 \theta \sin^2 \theta \left(\frac{1}{G_{LR}} - \frac{2\mu_{LR}}{E_L} \right). \quad (3.4)$$

The three moduli of elasticity E_L , E_R , and E_T , are usually obtained from compression tests. However, data for E_R and E_T are not extensive. Values of E_R and E_T for samples from a few species are listed in Table 3.3 as ratios with E_L . These ratios, as well as the three elastic constants themselves, vary within and between species and with moisture content and specific gravity. Often the E_L value determined from bending, rather than from an axial test, is the only E available. From Table 3.3 it can be seen that E_L is by far the largest among the moduli of elasticity because the majority of the microfibrils are aligned most nearly in the longitudinal direction. E_R is greater than E_T because of the reinforcing action of the rays.

The three moduli of rigidity and the six Poisson's ratios for a few species are also presented in Table 3.3. Among the moduli of rigidity, G_{RT} is much lower than the other two shear moduli. This is due to the fact that the applied shear stress acts in the RT plane, tending to distort the cross section of the tubular cells.

3.3 Timber Post

Timber posts are used as temporary supports near the working face, as breaker posts in pillar removal, or along both sides of an entry to reduce the span supported by the ribs. The latter is commonly seen along belt or track entries in coal mines to maintain a clear roadway for

Table 3.3. Elastic constants of various species
(Forest Products Lab., 1974)

Species	Approximate specific gravity ¹	Approximate moisture content (pct.)	Modulus of elasticity ratios		Ratio of modulus of rigidity to modulus of elasticity			Poisson's ratios					
			E_T/E_L	E_R/E_L	G_{LR}/E_L	G_{LT}/E_L	G_{RT}/E_L	μ_{LR}	μ_{LT}	μ_{RT}	μ_{TR}	μ_{RL}	μ_{TL}
Balsa	0.13	9	0.015	0.046	0.054	0.037	0.005	0.229	0.488	0.665	0.217	0.011	0.007
Birch, yellow64	13	.050	.078	.074	.068	.017	.426	.451	.697	.447	.033	.023
Douglas-fir50	12	.050	.068	.064	.078	.007	.292	.449	.390	.287	.020	.022
Spruce, Sitka38	12	.043	.078	.064	.061	.003	.372	.467	.435	.240	.029	.020
Sweetgum53	11	.050	.115	.089	.061	.021	.325	.403	.682	.297	.037	.020
Walnut, black59	11	.056	.106	.085	.062	.021	.495	.632	.718	.379	.052	.035
Yellow-poplar38	11	.043	.092	.075	.069	.011	.318	.392	.703	.329	.029	.017

¹ Based on oven-dry weight and volume at the moisture content shown.

transportation purposes. Posts may also be used where additional support is required in order to assist roof bolting (Faulkner, 1985).

Generally, there are two types of plain timber posts, namely round posts and square posts. The terms, round and square, refer to the cross-section of the timber post. The Federal Register stipulates that a round post will be 1" in diameter for each 15" in length but no less than 4" in diameter. It also states that split posts should have a cross-sectional area equal to that required for round posts of equivalent length.

The strength of the timber post is affected by many factors. For a certain species of wood, strength is a function of several variables such that:

$$P = f(m, i, g,)$$

where

P = the strength of the post,

m = moisture content in the post,

i = imperfections such as knots,

g = specific gravity.

These factors are going to be discussed in Section 3.6. The species of wood also has a great effect on the ultimate strength of a post.

Hardwoods such as oak, hickory, maple, and locust exhibit much higher compressive strength than some softwoods such as pine and spruce. The capacity of the timber post is also related to the length to diameter ratio. Figure 3.3 and Table 3.4 show this relationship.

As shown in figure 3.4, plain timber posts do not have good load-deformation characteristics. They generally exhibit a shortening of less than 1 percent under their maximum loads. Testing has shown that a

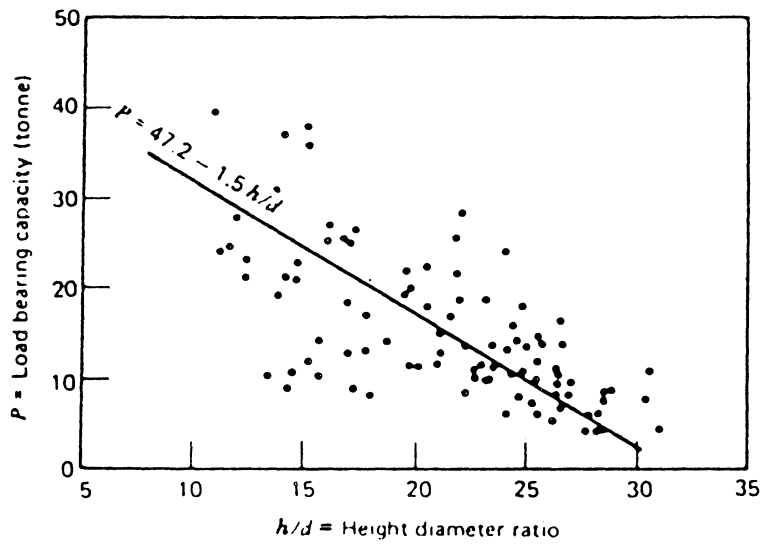


Figure 3.3. The relationship between the load bearing capacity and the height-diameter ratio. (Biron, 1983)

Table 3.4 The Effect of Height-ratio on the Load Bearing Capacity of Timber Post (Biron, 1983)

Height-diameter ratio	5	10	15	20	25
Load bearing capacity (tonnes)	39.5	32.2	24.7	17.2	9.7

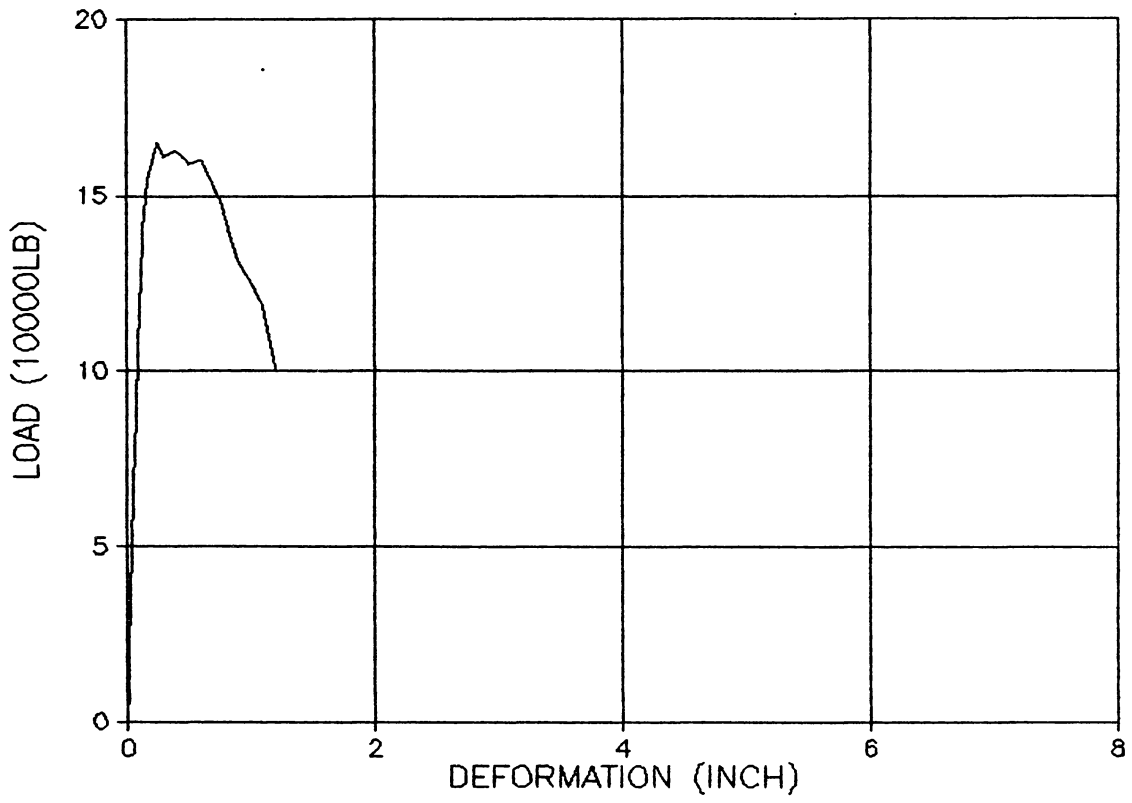


Figure 3.4. Load-deformation curve of a hickory post (8"x6"x29").

wooden post usually fails in a buckling or shear failure mode. The load at which this takes place depends on the type of wood being used and the factors mentioned above. Table 3.5 shows the results from testing timber posts. The manner in which a wood column buckles and fails can be dangerous. Whole lines of timber posts have been known to snap when a sudden ground motion introduced high loads onto them (Johnsson, 1985). The rate of loading is also important with failure taking place much sooner when an impact-type loading occurs. A slow, even loading will produce more deformation before failure. It can be reasoned that slow loading produces slow failure because the individual wood fibers have time to adjust to the load. The sudden failure of wooden posts is undesirable, as the roof is no longer supported and thus deteriorates quickly.

Preliminary testing and observation have shown some differences between the round post and the square post, in both the strength and failure mode. From Table 3.5, it can be seen that the strength of the round posts is less than that of the equivalent square post. Observations made on the timber post tests reveal that most round posts fail in a buckling mode while some square posts break down in a shearing failure mode.

The following reasons may help to explain the difference in performance between the round posts and square posts:

1. From the wood structure point of view, the round post is usually a section of the trunk of a small tree or a branch and it consists of both heartwood and sapwood, while the square post is commonly cut from a large trunk and only contains heartwood. The sapwood in the round post

Table 3.5 Results of Compression Tests of Timber Posts

Post type	Size	Moisture content (%)	Maximum stress (psi)	Maximum Load (1000 lbs)	Deformation at maximum load (inches)
S. Poplar	5.6"x5.6"x42"	22	2551	80	0.19
S. Poplar	5.4"x5.3"x42"	19	2621	75	0.22
S. Poplar	5.3"x5.2"x35"	19	2903	80	0.38
S. Poplar	5.25"x5.25"x72"	X	1451	40	X
S. Poplar	3.5"x3.5"x60"	X	2190*	27*	X
R. Poplar	4.25"-5"x60"	X	1132	18	X
R. Poplar	4.25"-4.75"x60"	X	1007	16	X
R. Poplar	4"-4.25"x60"	X	1011*	14*	X
R. Poplar	4"-4.75"x60"	X	1464	22	X
R. Pine	4"-4.25"x60"	X	1348	18	X
R. Pine	4.75"-5"x60"	X	1876	35	X
R. Pine	4.5"-4.75"x60"	X	1251	21	X
R. Beech	4"-5"x60"	X	1699	27	X
S. Hickory	8"x6"x29"	Green	3438	165	0.24
S. White Oak	9"x7"x23	Green	3571	210	0.19
S. Red Oak	8"x6"x42"	Green	2813	135	0.43

R - Round,
S - Square,
X - data is not available,
* - average value.

may result in the average strength of the round post being lower than that of its square counterpart since the strength of the sapwood is usually lower than that of the heartwood, although sometimes this difference may not be significant. Another reason is that round posts usually contain bark which may cause faulty sizing. The natural irregularities of the shape of the round posts may also contribute to their lower strength.

2. The moment of inertia for the square cross-section is larger than that for the circular cross-section with the same sectional area. Thus the critical buckling load for the square post is higher than that for the round post. This will become clear from the following derivation.

For a round post with diameter D, the equivalent square post has sides of 0.886D. The moments of inertia for the square section and for the circular section are $0.051D^4$ and $0.049D^4$ respectively. The critical buckling loads are:

$$P_s = \frac{0.13ED^4}{l^2} \quad (3.5)$$

for a square post and

$$P_r = \frac{0.12ED^4}{l^2} \quad (3.6)$$

for a round post, where l and E are the length and Young's modulus of the posts respectively. The critical buckling load for a square post is 8 percent larger than that for a round post.

In an attempt to find out the stress distributions in a timber post subject to uniaxial compression, a finite element program is modified.

The uniaxial compression of a round timber post is a three dimensional problem. However, due to the axi-symmetric nature of the round post, the problem can be solved by a two dimensional program. The program was originally written by T. Kuppusamy. In the original program, the material in each element is viewed as an isotropic material, and for the axially symmetric problem, the constitutive relation is (Kuppusamy, 1986):

$$\begin{pmatrix} \sigma_R \\ \sigma_L \\ \sigma_T \\ \tau_{RL} \end{pmatrix} = \frac{E}{(1+\mu)(1-2\mu)} \begin{pmatrix} 1-\mu & \mu & \mu & 0 \\ \mu & 1-\mu & \mu & 0 \\ \mu & \mu & 1-\mu & 0 \\ 0 & 0 & 0 & (1-2\mu)/2 \end{pmatrix} \begin{pmatrix} \epsilon_R \\ \epsilon_L \\ \epsilon_T \\ \epsilon_{RL} \end{pmatrix} \quad (3.7)$$

In equation 3.7, there are only two independent elastic constants, E and μ . Because wood is an orthotropic material and there are 9 independent elastic constants, the above relation is replaced by following relation in the modified program:

$$\begin{pmatrix} \sigma_R \\ \sigma_L \\ \sigma_T \\ \tau_{RL} \end{pmatrix} = \begin{pmatrix} C_{11} & C_{12} & C_{13} & 0 \\ C_{21} & C_{22} & C_{23} & 0 \\ C_{31} & C_{32} & C_{33} & 0 \\ 0 & 0 & 0 & C_{44} \end{pmatrix} \begin{pmatrix} \epsilon_R \\ \epsilon_L \\ \epsilon_T \\ \epsilon_{RL} \end{pmatrix} \quad (3.8)$$

where

$$C_{11} = \frac{1-\mu_{LT}\mu_{TL}}{E_L E_T \delta}$$

$$C_{12} = \frac{\mu_{LR} + \mu_{TR} \mu_{LT}}{E_L E_T \delta} = C_{21}$$

$$C_{13} = \frac{\mu_{TR} + \mu_{LR} \mu_{TL}}{E_L E_T \delta} = C_{31}$$

$$C_{22} = \frac{1 - \mu_{RT} \mu_{TR}}{E_R E_T \delta}$$

$$C_{23} = \frac{\mu_{TL} + \mu_{RL} \mu_{TR}}{E_R E_T \delta} = C_{32}$$

$$C_{33} = \frac{1 - \mu_{RL} \mu_{LR}}{E_R E_L \delta}$$

$$C_{44} = G_{LR}$$

$$\delta = \frac{1 - \mu_{RL} \mu_{LR} - \mu_{LT} \mu_{TL} - \mu_{TR} \mu_{RT} - 2 \mu_{LR} \mu_{TL} \mu_{RT}}{E_R E_L E_T}$$

The modified program is attached in Appendix A.

The finite element mesh layout for the uniaxial compression of a round timber post is shown in figure 3.5. Since the post is axial symmetric, only half of the longitudinal cross-section of the post is considered. The length of the area under consideration is the length of the post and the width is the radius of the post. The load on the end of the post is assumed uniform. The elastic constants are chosen from Table 3.3. The radial and tangential stress distributions obtained from the finite element analysis are shown in figure 3.6 and figure 3.7, the longitudinal stress is uniformly distributed, and the shear stress τ_{RL} is negligible. From figures 3.6 and 3.7 it can be seen that both the algebraical value of the radial stress and that of the tangential stress decrease as the distance from the center of the post increases. In the figures, negative values indicate compressive stress and positive ones

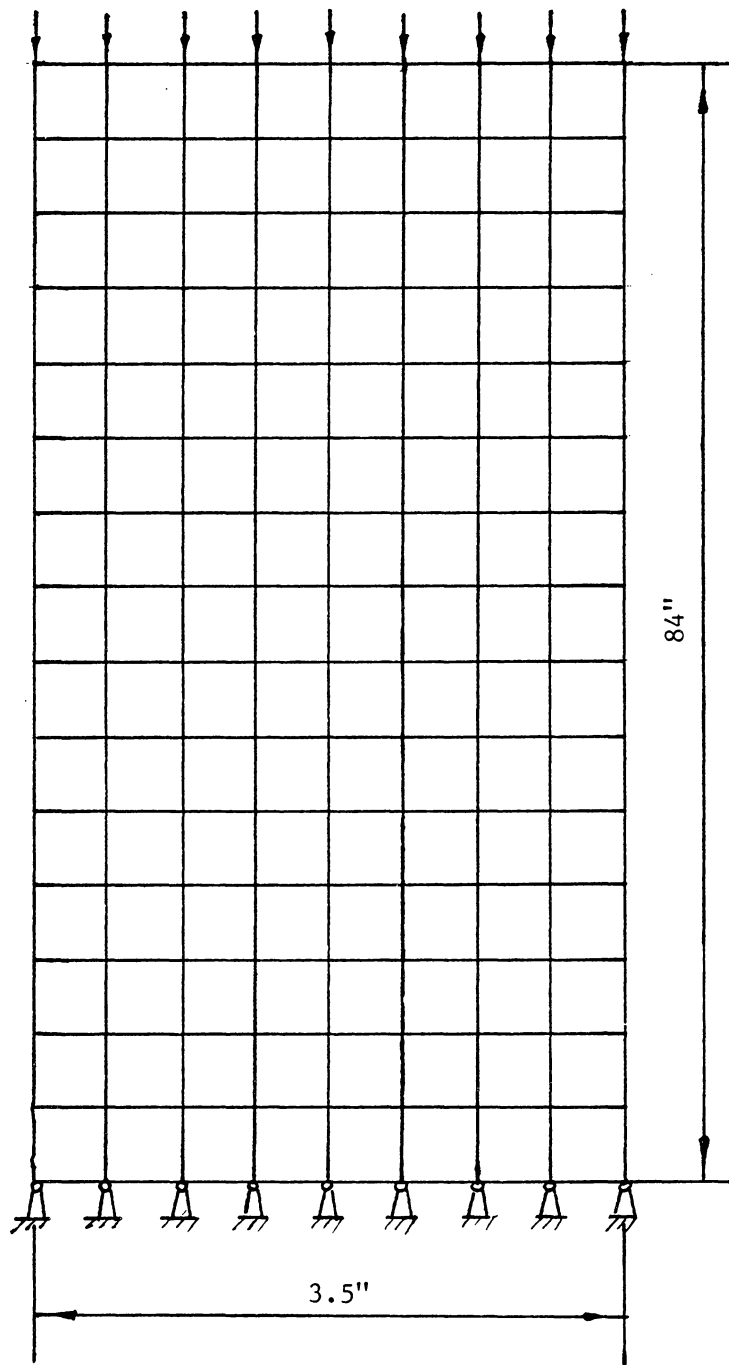


Figure 3.5. Finite element mesh for analyzing the stress distribution in a circular post.

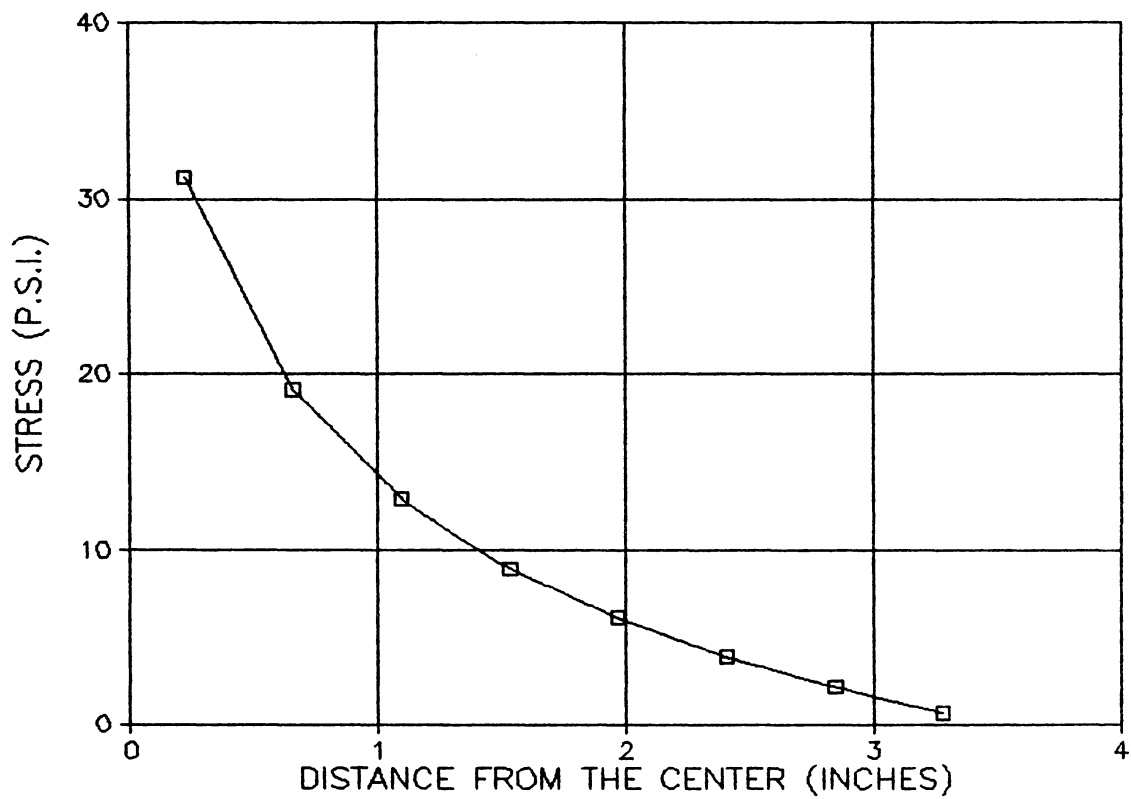


Figure 3.6. Radial stress distribution in a circular post.

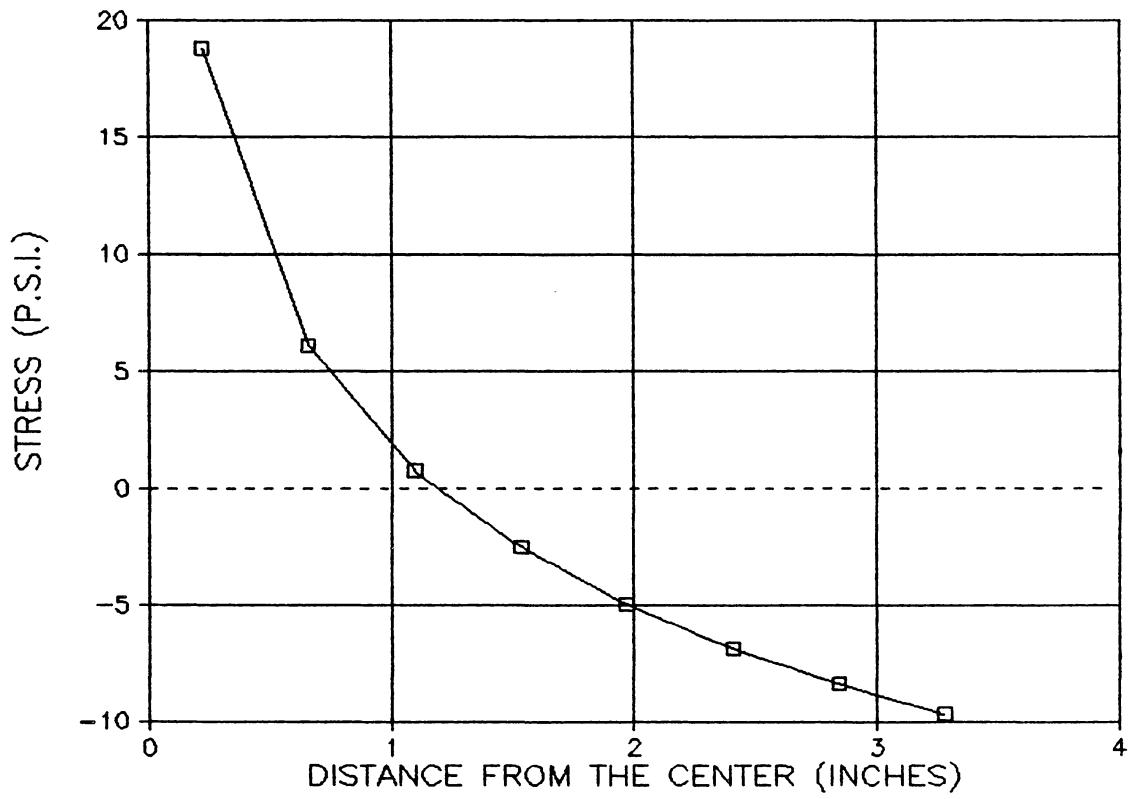


Figure 3.7. Tangential stress distribution in a circular post.

indicate tensile stress. The change of the tangential stress from tensile to compressive along the radius may suggest a possible twist inside the post. Because there is no shear stress in the planes normal to σ_L , σ_T and σ_R , the three normal stresses can be regarded as principal stresses. Thus the largest shear stress in the post is:

$$\tau_{\max} = \frac{\sigma_R - \sigma_L}{2} \quad (3.9)$$

and is on the plane at 45° to σ_R and σ_L . The location of τ_{\max} is in the center of the post since σ_R reaches maximum value there. Thus if the post is going to fail in a shearing failure mode, the failure probably will begin at the center of the post.

The finite element program can not be used to analyze the stress distribution of square posts since the problem is no longer an axi-symmetric one, and therefore a three dimensional program must be utilized.

It seems that timber posts are very easy to use. However, there are some points to which one must pay attention when using them. One problem associated with the use of timber posts is non-uniform loading or eccentric compression. When an eccentric load is applied to the post, the post is subjected not only to compression but also to bending. In the case of pure compression the maximum compressive stress in the post is:

$$\sigma_{pc} = \frac{Q}{A} \quad (3.10)$$

where Q = the load applied to the post by roof and floor;

A = the cross-sectional area of the post.

On the other hand, when an eccentric compression force is applied, the maximum compressive stress in the post is:

$$\sigma_{ec} = \frac{Q}{A} + \frac{Q.a.c.\sec(u)}{I} \quad (3.11)$$

where a is the distance between the centroid of the post cross-section and the point where the force acts, c is the distance between the neutral surface and the point where the maximum compressive stress occurs, I is the moment of inertia of the cross-section area and:

$$u = \frac{l \sqrt{Q}}{2 \sqrt{EI}}$$

where l is the length of the post and E the modulus of elasticity.

Comparing σ_{ec} and σ_{pc} , one can see that the maximum compressive stress is increased by $(Q.a.c.\sec(u))/I$, due to eccentricity of the load. In order to avoid the eccentric compression, several precautions can be taken, the most common of which is the use wedges, headers and caps.

3.4 Timber Cribs

Cribs are often used to maintain important intersections and gateroads for longwall mining. In many cases wood cribs will handle roof support demands that can not be met by normal timber posts. The most useful features of timber cribs are their stability and deformability.

The yieldability of timber cribs is high since the load on a crib is perpendicular to the wood grain. Tests have been done to determine the load-deformation characteristics of timber cribs. In the 1960's, the South Africans conducted a load-deformation experiment on

a range of 36 in. high cribs constructed from commercial 32 in. saligna slabbed crib pieces. The diameters of the timber poles from which the slabbed pieces were made ranged from 4.46 to 8.65 inches. After the test results were analyzed, this relationship between load and deformation was obtained (Margo, 1966):

$$T = A(e^{Bx} - e^{-Cx})(1 + Pe^{-Re-Sx}) \quad (3.12)$$

where $A = 0.27296NLW - 9.14860$

$$B = 0.00104D - 0.00003NL + 0.02650$$

$$C = 0.00860M + 0.03116$$

$$S = 0.16596e^{-0.046} + 0.058$$

$$P = 0.0083 / (S + 0.005)^{2.375}$$

$$R = 5.4834e^{38.16S}$$

T = vertical load, tons,

x = deformation, percentage,

L = effective length of crib piece, inches,

N = number of pieces per row,

W = width of slabbing, inches,

D = pole diameter, inches,

M = moisture content as measured.

Tests were also performed as part of this research. The tests were not comprehensive and only three timber crib corners were tested, two on the one million loading frame manufactured by S.B.E.L. and one on the M.T.S. stiff testing machine. Because of the extension limit of the hydraulic ram of the loading frame, the crib specimen was unloaded after 4 inches of deformation, a spacer was installed between the specimen and the testing platen, and then the specimen was reloaded. The test

performed on the M.T.S machine was a continuous test. Each test took about twenty to thirty minutes. Deformation readings were taken at regular intervals. The moisture content in the timber was taken before each test and all the crib pieces were saturated. Table 3.6 shows the results from compression tests of timber crib corners. Figures 3.8 through 3.10 show the load-deformation curves of the crib corners tested and the regression curves from statistical analysis. The regression equations can be expressed in a general form for the three curves:

$$T = a x^{1/3} + b \quad (3.13)$$

where T and x have the same meanings as in equation 3.12 and, a and b are shown in Table 3.7.

It would be reasonable to assume that a full crib with four corners would bear at least four times as much load as one corner of a crib, and possibly more due to the extra confinement.

From figures 3.8 through 3.10, it is obvious that timber cribs have a very good yieldability. According to research done in South Africa (Margo, 1966), timber cribs can yield up to 50 percent of their height while the load still increases steadily. The initial stiffness of the timber cribs is something controversial. Some people tend to think that the initial stiffness of timber cribs is lower than that of the timber posts since the compression of timber cribs is perpendicular to the wood grain (Johnsson, 1985). However, this may not always be true because the stiffness of the cribs depends not only upon the elastic modulus perpendicular to the grain but also upon the size of the cribs and timber blocks. Thus, if properly designed, the initial stiffness of timber cribs could be very high and, based on the first criterion discussed in

Table 3.6 Result of Compression Tests on Timber Crib Corners

Test	Block Size	Crib Height	Moisture Content	Maximum Load (10,000 lbs)	Deformation (percentage)
Hickory	6"x8"x24"	25"	green	15	19.64
Oak	6"x8"x24"	24"	green	8.5	21.29
Beech	6"x6"x15"	12"	green	11.2	24.21

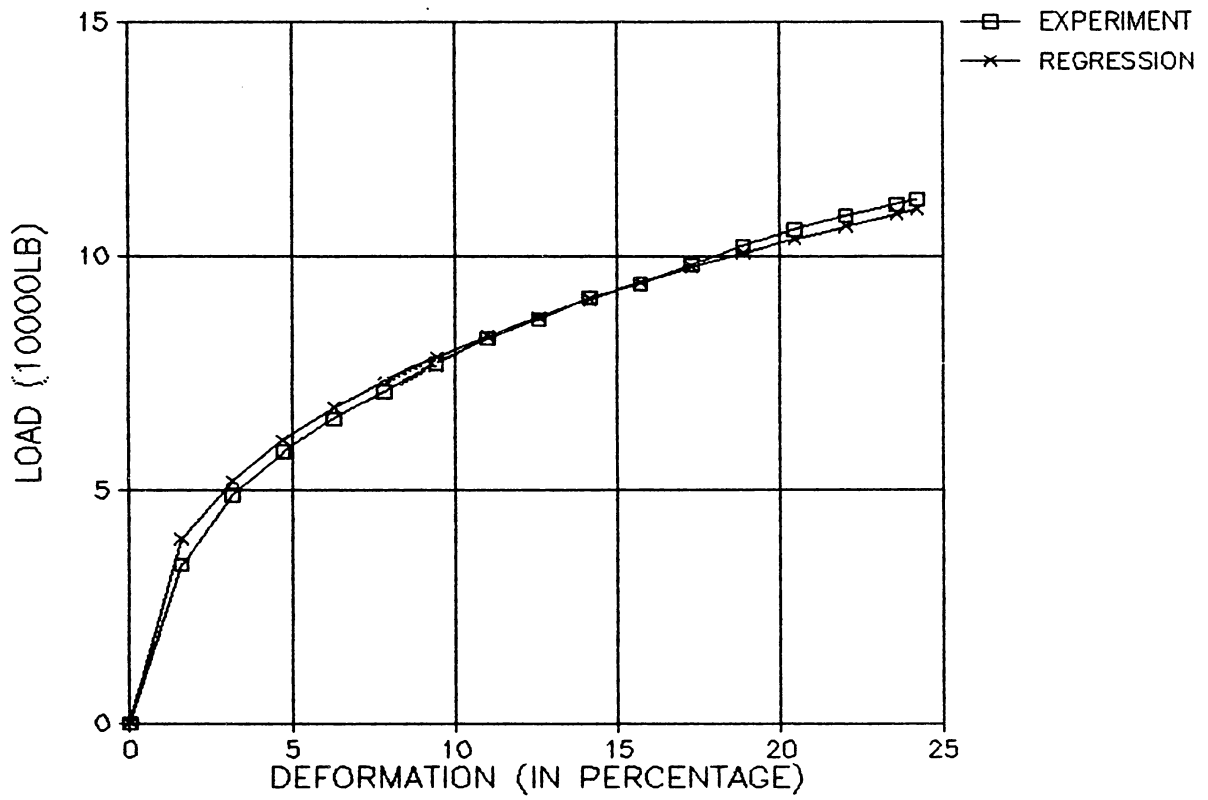


Figure 3.8. Load-deformation curve of a beech crib.

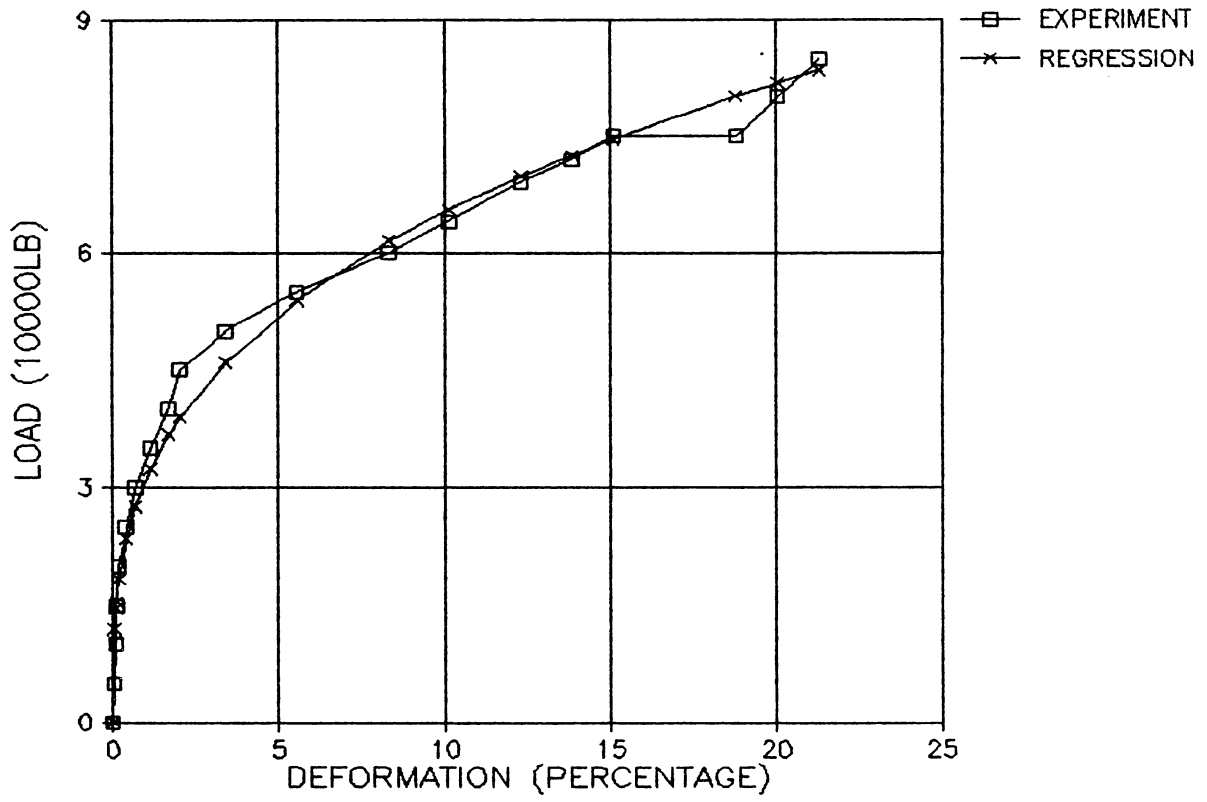


Figure 3.9. Load-deformation curve of an oak crib.

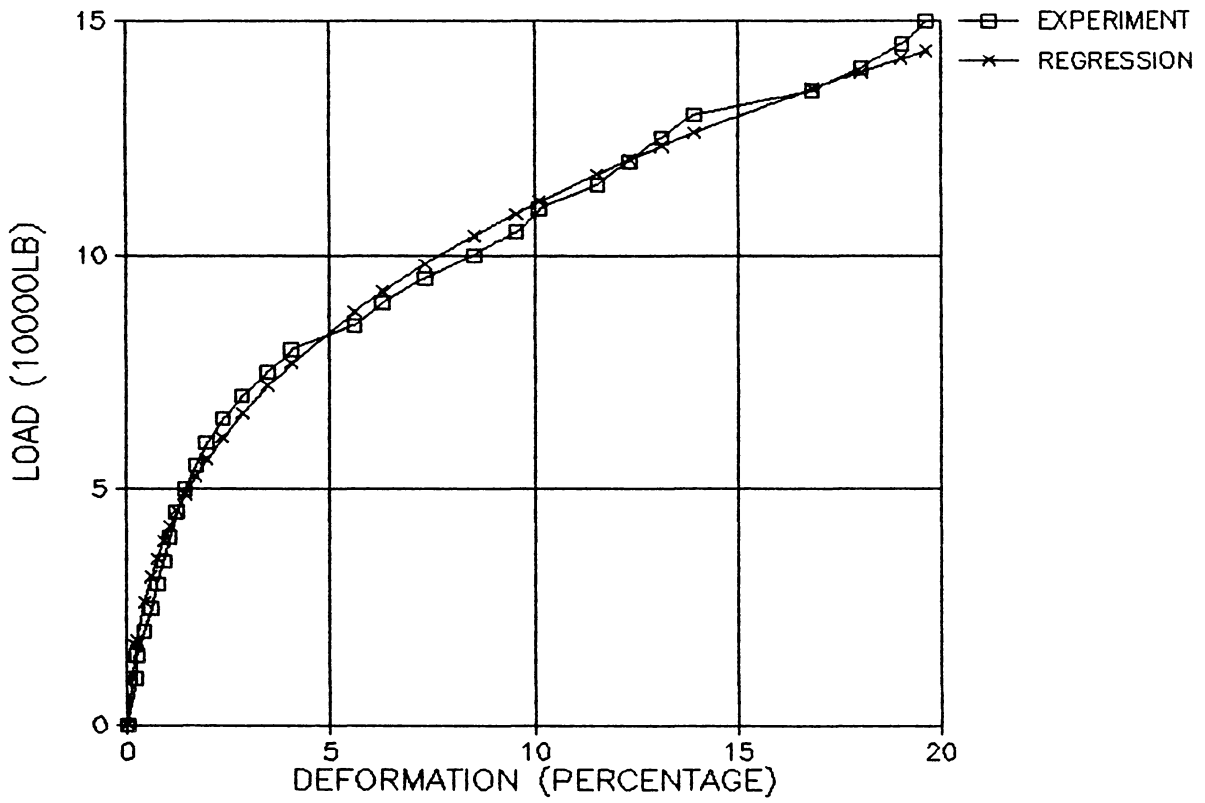


Figure 3.10. Load-deformation curve of a hickory crib.

Table 3.7 Regression Constants
For The L-D Curves of The Timber Crib Corners

Test	a	b	r
Hickory	6.017	-1.878	0.9935
Oak	2.946	0.175	0.9930
Beech	4.064	-0.760	0.9954

Chapter 2, timber cribs could be an ideal support.

The stability of the timber cribs is another important advantage of timber cribs. This can be seen from two points. First, the critical buckling load of the timber cribs is usually high. For example, a square post with sides S and length $10S$ has a critical buckling load:

$$P = \frac{\pi^2 E_L S^2}{4800}. \quad (3.14)$$

If the same kind of posts is used to construct a timber crib, the top view of which is shown in figure 3.11 and the height of which is also $10S$, then the critical buckling load for the crib is:

$$P = \frac{544\pi^2 E_R S^2}{4800}. \quad (3.15)$$

Suppose that the wood species is poplar, then from Table 3.3, $E_R = 0.092E_L$, and equation 3.15 can be written as:

$$P = \frac{50\pi^2 E_L S^2}{4800}. \quad (3.16)$$

From equations 3.16 and 3.14, it can be seen that in this example the crib is 50 times as stable as the post.

The stability of the cribs can also be appreciated when they are subjected to lateral load induced by the roof. The probability of collapse of the crib is much smaller than that of the posts since the resistant moment to rotation for the cribs is much larger than that for the posts.

Due to the way in which cribs are used, they are often required to last for a long time -- sometimes several years. Thus it is important to

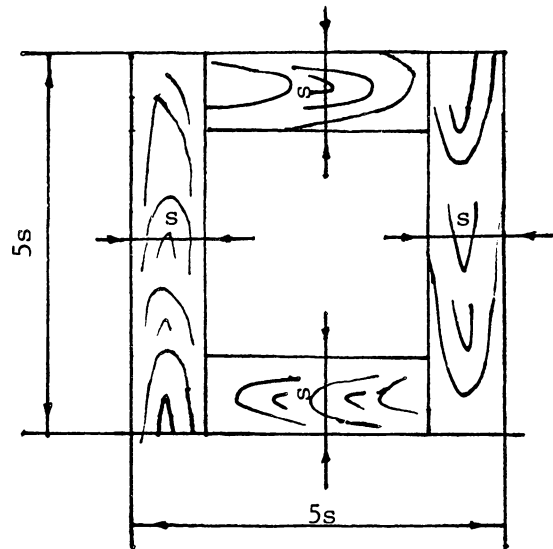


Figure 3.11. Plain view of the timber crib used for calculating the critical buckling strength.

take account of the shrinkage due to the loss of moisture content in the timber and the rheological properties of wood.

As mentioned earlier in this chapter, wood is dimensionally stable when the moisture content is above the fiber saturation point and it changes dimension as it gains or loses moisture below that point. It shrinks when losing moisture content and swells when gaining moisture content. It is the shrinkage that is our concern. Shrinkage of timber cribs can cause serious ground control problem since a very tight crib can relax due to shrinkage. For example, a 7 foot high hickory crib could shrink up to 3.22 inches when its moisture content changes from the fiber saturation point to 20 percent, that is, the shrinkage is equal to the deformation of a hickory crib under tens of thousands pounds of load. Based on the observations both in the lumber yards and in the coal mine, most timber supplied to the mines is green wood. Thus, most timber used in the mines will shrink to some degree, depending on the equilibrium moisture content which is a function of both the relative humidity and temperature of the surrounding air. In a coal mine the relative humidity and temperature of the air, and hence the equilibrium moisture content, change with location. Therefore the shrinkage of timber cribs will differ with location. In the intake airways where the temperature and relative humidity are relatively low, the shrinkage will be large while in the return airways where the temperature and relative humidity are high, the shrinkage will be smaller.

To predict the shrinkage of a timber crib, the relative humidity and temperature at the crib location should be known, and then the equilibrium moisture content can be found. Tables for finding

equilibrium moisture contents under various temperature and humidity conditions are available. Substituting the equilibrium moisture content for m into equation 3.1, the expected shrinkage is obtained.

The rheological properties of wood may also have profound effects on the performance of timber cribs. Rheological properties describe the time-dependent behavior of wood which includes creep and relaxation. Creep is defined as the time-dependent deformation exhibited by a material under constant load, while relaxation is the decreasing resistance to force in a material subjected to a constant deformation (Bodig, 1982). Figures 3.12 and 3.13 are creep and relaxation curves respectively under compression perpendicular to the grain. While creep may satisfy the yieldability requirement of the support, relaxation of the timber crib is a disadvantage.

The creep and relaxation of the timber cribs can be significant. For example, a 7 foot high red oak crib could deform up to 4.8 inches in 70 hours under 286 psi of load, and the resistance of a maple crib can drop 3.4 percent of its original value within 17 hours. Relaxation is dangerous in the sense that it will reduce the resistance of the crib to roof pressure. Unlike the shrinkage discussed above, relaxation is more difficult to predict. Various mechanical models such as Maxwell, Kelvin, and Burger have been developed to formulate the problem. However, formulae derived from those models may sometimes be useless since the constants involved are unknown. For instance, the formula for relaxation obtained from a Maxwell model is (Bodig, 1982):

$$P = P_0 e^{-t/\tau} \quad (3.17)$$

where P = the force at time t ,

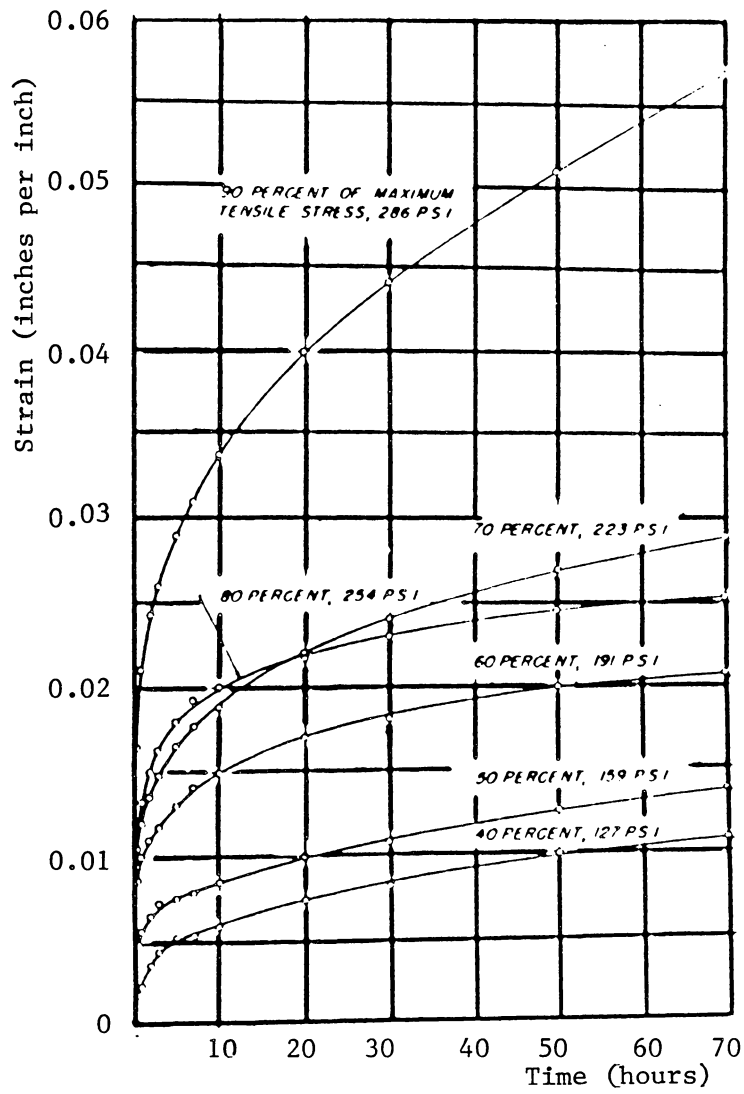


Figure 3.12. Compression perpendicular to grain creep of red oak at 82°C. (Bodig, 1982)

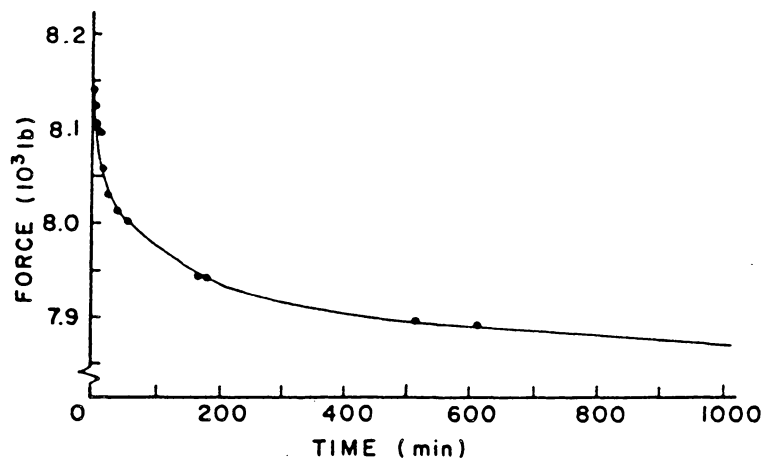


Figure 3.13. Relaxation of a compression force acting on sugar maple perpendicular to grain. (Bodig, 1982)

P_0 = the force at time $t=0$,

$\tau = r/k$,

r = damping constant,

k = the Hookean constant.

In this formula, since τ is not generally available, the application of the formula is limited. One way to find out τ is through experimentation. For one species of wood, the data from relaxation experiments can be fit into equation 3.17 by a statistical method. If the data follow the curve defined by equation 3.17 statistically, then τ can be obtained. Equation 3.17 can thus be used to predict the relaxation of the crib made of that species of wood.

In order to prevent the problems created by shrinkage and relaxation of the cribs, regular checking and maintenance of the timber cribs is important. If necessary, wedges and caps can be added to the cribs.

3.5 Timber Gallery Sets

Timber gallery sets usually consist of three parts; namely the top beam, the liners and the side posts or legs, as shown in figure 3.14. Sometimes, in order to reduce the span of the top beam, a middle post is set up at the mid-point of the beam span. Timber gallery sets are mainly used for entry support. The load acting on a timber gallery set underground is quite complicated. To analyze the stability and the strength of gallery sets, some assumptions have to be made, and the principles of mechanics are applied. Tests were conducted in this research to examine the load-deformation characteristics of timber posts

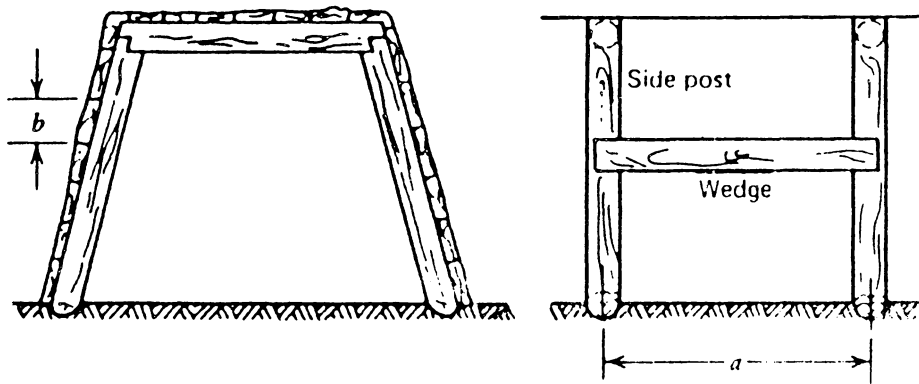


Figure 3.14. Timber gallery set.
(Biron, 1983)

with shoes, which resemble the load-deformation characteristics of a gallery set at the beam ends since both involve compression perpendicular and parallel to the grain.

There are not many literature references about timber gallery sets. Biron and Arioglu (1983) adopted the models shown in figure 3.15 for designing the top beam and the side posts. In the models the wooden set works as a simple beam supported at both ends, loaded uniformly. The deflection of the top beam is:

$$y = - \frac{q_t}{24EI} (x^4 - 2L_b x^3 + L_b^3 x) \quad (3.18)$$

and the bending moment is:

$$M = EI \frac{d^2 y}{dx^2} = 0.5q_t L_b x - 0.5q_t x^2 \quad (3.19)$$

where q_t is the vertical load per unit length induced by the roof, L_b is the span of the top beam, and EI is the bending stiffness. The maximum deflection and bending moment are at the middle point of the beam span

where $x = L_b/2$, and they are:

$$y_{\max} = - \frac{5q_t L_b^4}{384EI} \quad (3.20)$$

$$M_{\max} = \frac{q_t L_b^2}{8} \quad (3.21)$$

For the side posts, the deflection and bending moment can be obtained by substituting q_y and L_s for q_t and L_b respectively, where q_y is the lateral load per unit length and L_s is the span of the side beam.

Equations 18 through 21 may result in serious errors when used for estimating the actual deflections and bending moments in the top beam and

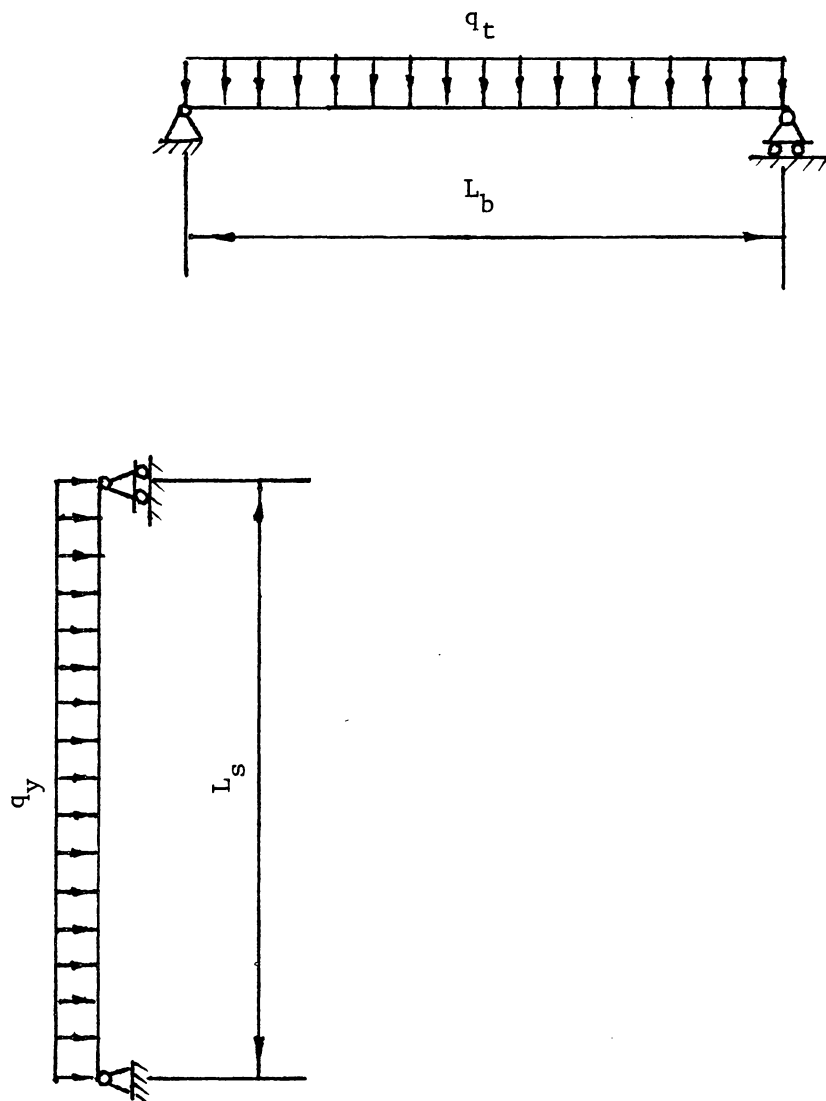


Figure 3.15. Model for calculating the deflection of a gallery set. (Biron, 1983)

side posts. To compensate for the deficiency of the models in figure 3.15, new models are proposed, as shown in figure 3.16. In the new models, the axial load is also considered in addition to the transverse load. Axial compression increases the deflection and bending produced by the transverse load while axial tension has the opposite effect. In the models proposed, the axial load is compression and it increases the deflection and bending moment. Thus the effect of the axial load can not be ignored.

To obtain the deflection and bending moment of the beam under both the transverse and axial loads, the effect of axial load alone can not be superimposed on the state produced by transverse load alone, and instead, axial and transverse loads must be considered simultaneously (Cook, 1985). For the beam in figure 3.16(a), let M_t represent bending moment caused by transverse load alone, as in Biron's model. (In general, M_t is the bending moment that prevails when all loads except axial force R_{ah} are applied.) Axial force R_{ah} is considered constant along the length, and is assumed to be less than the buckling load. Force R_{ah} has no eccentricity; that is, when lateral deflection y is zero, R_{ah} is directed through the centroids of the cross sections. When the beam has deflected, R_{ah} has a moment arm y below a point on the beam axis and produces a bending moment $R_{ah}y$. The standard moment-curvature relation of elastic small-deflection beam theory, $EI(d^2y/dx^2) = M$, becomes

$$EI \frac{d^2y}{dx^2} = -R_{ah}y + M_t. \quad (3.22)$$

The $R_{ah}y$ term is negative because positive R_{ah} and negative y are associated with positive curvature ($d^2y/dx^2 > 0$). If $R_{ah} = 0$, equation

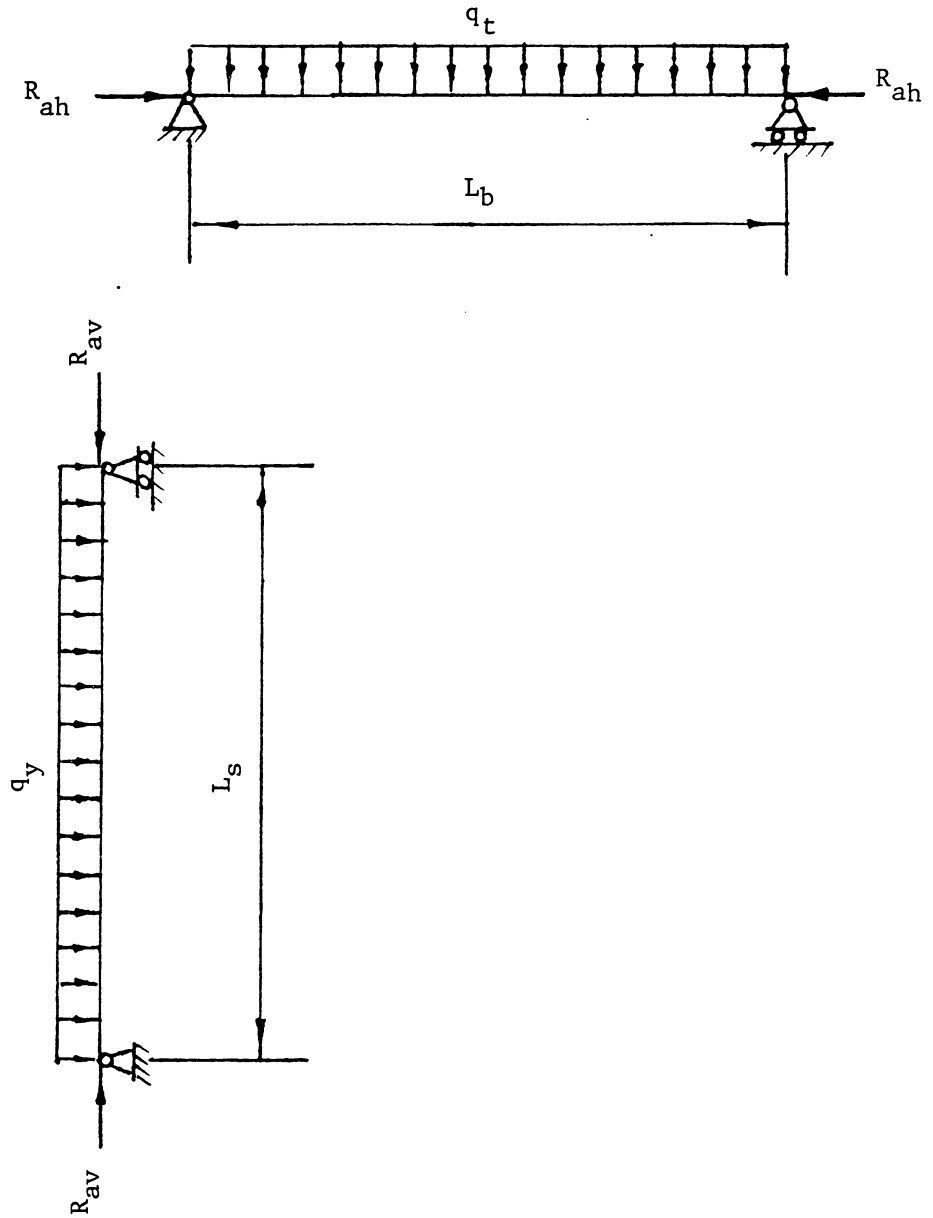


Figure 3.16. Modified model for calculating the deflection of gallery set.

3.22 becomes the standard equation for beam deflection analysis under transverse load alone. If $M_t = 0$, equation 3.22 becomes the equation used to establish the Euler buckling load of the column.

By rewriting equation 3.22, and then solving it with EI constant, the following can be obtained:

$$\frac{d^2y}{dx^2} + k^2y = \frac{M_t}{EI} \quad (3.23)$$

$$y = C_1 \text{Sinkx} + C_2 \text{Coskx} + y_p \quad (3.24)$$

where $k^2 = \frac{R_{ah}}{EI}$ and $R_{ah} = \frac{q_y L_s}{2}$.

C_1 and C_2 are constants of integration and y_p is a particular solution associated with M_t .

For the uniformly distributed load q_t in figure 3.16a, M_t is the same as in equation 3.19, and the particular solution is:

$$y_p = - \frac{q_t}{2EI k^2} (x_2 - L_b x - \frac{2}{k^2}). \quad (3.25)$$

Constants C_1 and C_2 in equation 3.24 must be chosen so that deflection y is zero at $x = 0$ and at $x = L_b$. After evaluating these constants and substituting them, the deflection of the top beam can be obtained:

$$y = - \frac{q}{EI k^4} [(1 - \text{CoskL}_b) \frac{\text{Sinkx}}{\text{SinkL}_b} + \text{Coskx} + \frac{k^2}{2} (x_2 - L_b x) - 1]. \quad (3.26)$$

The bending moment is

$$M = \frac{q_t}{k^2} [(1 - \text{CoskL}_b) \frac{\text{Sinkx}}{\text{SinkL}_b} + \text{Coskx} - 1]. \quad (3.27)$$

The maximum deflection and bending moment occur at $x = L_b/2$,

$$y_{Lb/2} = - \frac{q_t}{EI k^4} \left[\frac{1 - \cos(kL_b/2)}{\cos(kL_b/2)} - \frac{k^2 L_b^2}{8} \right] \quad (3.28)$$

$$M_{Lb/2} = \frac{q_t}{k^2} \frac{1 - \cos(kL_b/2)}{\cos(kL_b/2)}. \quad (3.29)$$

If R_{ah} is ignored, as in Biron's model (and therefore $k = 0$), these expressions approach the indeterminate form $0/0$. It can be shown that limiting values for $R_{ah} = 0$ are:

$$y_{Lb/2} = - \frac{5q_t L_b^4}{384EI}$$

$$M_{Lb/2} = \frac{q_t L_b^2}{8}.$$

These are exactly the same as in equations 3.20 and 3.21.

It can be seen from equation 3.26 that y becomes infinite when $kL_b = \pi$, that is, when $R_{ah} = \pi^2 EI/L_b^2$. This is the classical buckling load of Euler column theory.

The deflection and bending moment of the top beam can also be estimated by a simpler but less accurate approach. In equation 3.22, let $R_{ah} = 0$ and the equation becomes

$$EI \frac{d^2 y_t}{dx^2} = M_t \quad (3.30)$$

where y_t is the lateral displacement under transverse load alone.

Elimination of M_t between equations 3.22 and 3.30 yields

$$EI \frac{d^2 y}{dx^2} = EI \frac{d^2 y_t}{dx^2} - R_{ah} y. \quad (3.31)$$

Assume that the deflection curve has the same shape whether or not axial

force is present. Axial force R_{ah} is assumed to change only the amplitude of deflection. The deflection curve is approximated by a half sine wave:

$$y = \bar{y} \sin \frac{\pi x}{L} ; y_t = \bar{y}_t \sin \frac{\pi x}{L} \quad (3.32)$$

where \bar{y} and \bar{y}_t are the amplitudes of lateral deflection, respectively with and without the presence of an axial force. Substitution of equation 3.32 into equation 3.31 yields

$$\frac{\pi^2 EI}{L_b^2} \bar{y} = \frac{\pi^2 EI}{L_b^2} \bar{y}_t + R_{aqh} \bar{y}. \quad (3.33)$$

It is known that $\pi^2 EI/L_b^2$ is the column buckling load R_{cr} . Therefore the maximum deflection of the beam is

$$\bar{y} = \frac{\bar{y}_t}{1 - (R_{ah}/R_{cr})}. \quad (3.34)$$

Assuming that bending moments are proportional to deflections, then the bending moment is

$$M = \frac{M_t}{1 - (R_{ah}/R_{cr})}. \quad (3.35)$$

In the latter two equations the denominator acts to amplify the deflection \bar{y}_t and bending moment M_t produced by transverse load alone.

For the side posts, same kind of analysis can be done by using the model shown in figure 3.16(b). Substituting q_y , R_{av} , and L_s for q_t , R_{ah} , and L_b respectively in equation 3.22 through equation 3.35 will yield the desired results.

The deflection and bending moment of the liners can be obtained by using Biron's model since liners usually are not subjected to axial load.

In addition to deflection, the deformation at the end of the top beam and the liners is also important. For the top beam, the compression at its ends is both perpendicular and parallel to wood grain. Tests were conducted to determine the load-deformation characteristics of the wood set (post with shoe) involving compression both perpendicular to and parallel to the wood grain. In the tests, a post was put on top of a wood block with the grains of the post and the block perpendicular to each other, as shown in figure 3.17. The compression is parallel to the grain of the post and perpendicular to the grain of the block. The load-deformation curve of this set is similar to that of the timber crib as indicated in figure 3.18. Therefore it is reasonable to infer that the ends of the top beam will deform in roughly the same way as the wood sets tested since both cases involve compression parallel and perpendicular to grain.

The displacement of the liner ends includes both the deflection of the beam and its own deformation since the ends of the liner rest on the beam. Thus, when calculating the displacement of the liner, the deflection expressed in equation 3.26 and the deformation determined by equation 3.13 should be combined.

3.6 Factors Affecting The Strength and Stability of Timber Support

There are many factors affecting the strength and stability of timber supports. Here only some important ones are discussed.

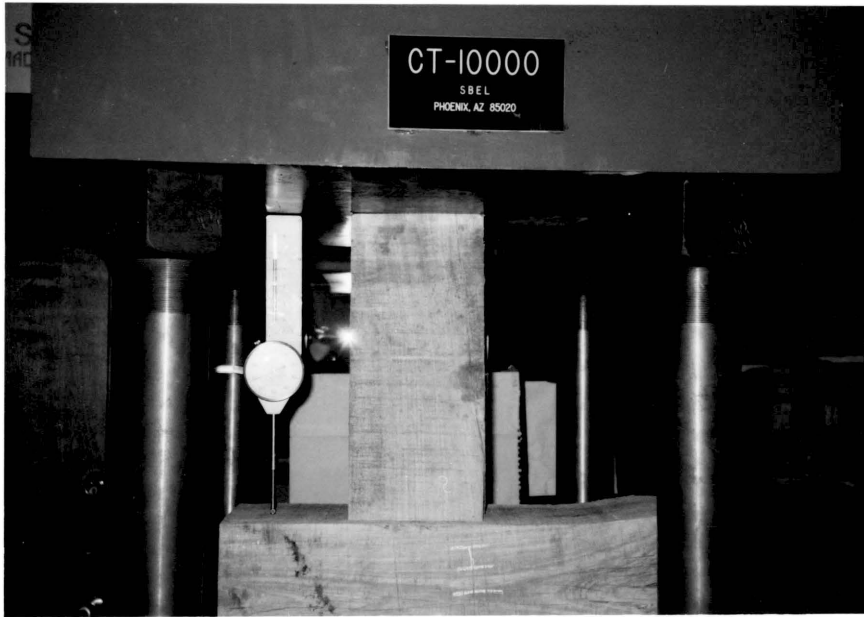


Figure 3.17. Post with shoe, under test.

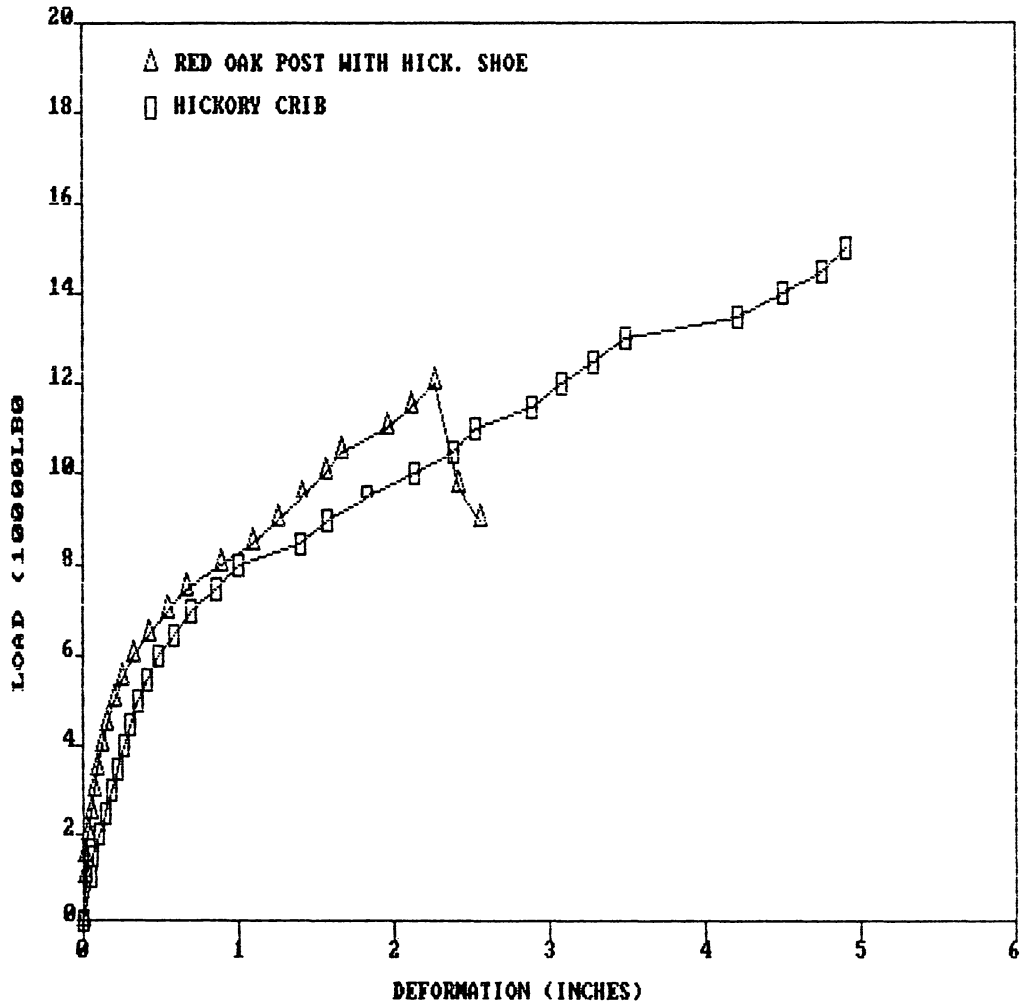


Figure 3.18. Comparison between the load-deformation curves of the timber crib and post with shoe.

Moisture content

Many mechanical properties of wood are affected by changes in moisture content below fiber saturation point. Most of these properties increase with decrease in moisture content. The relationship that describes these clear wood property changes in the vicinity of 70°F, is (Forest Products Lab., 1974):

$$P = P_{12} (P_{12}/P_g)^{-((M-12)/(M_p-12))} \quad (3.36)$$

where P is the property and M the moisture content in percent. M_p is the moisture content at which property changes due to drying are first observed. This moisture content is slightly less than the fiber saturation point. P_{12} is the property value at 12 percent moisture content and P_g is the property value for all moisture contents greater than M_p .

The above formula is a rough estimation of the mechanical properties of wood, since not all properties are affected by moisture content to the same extent. For underground timber supports the most critical properties are the compression strengths parallel and perpendicular to the grain, and the modulus of rupture. The changes in these three properties with moisture content are shown in figures 3.19 through 3.20. Although these properties are affected significantly by moisture content, it seems that shrinkage is more important than the change in strength, since most underground timber supports are saturated when put into place and hence their strength will increase as the moisture content decreases.

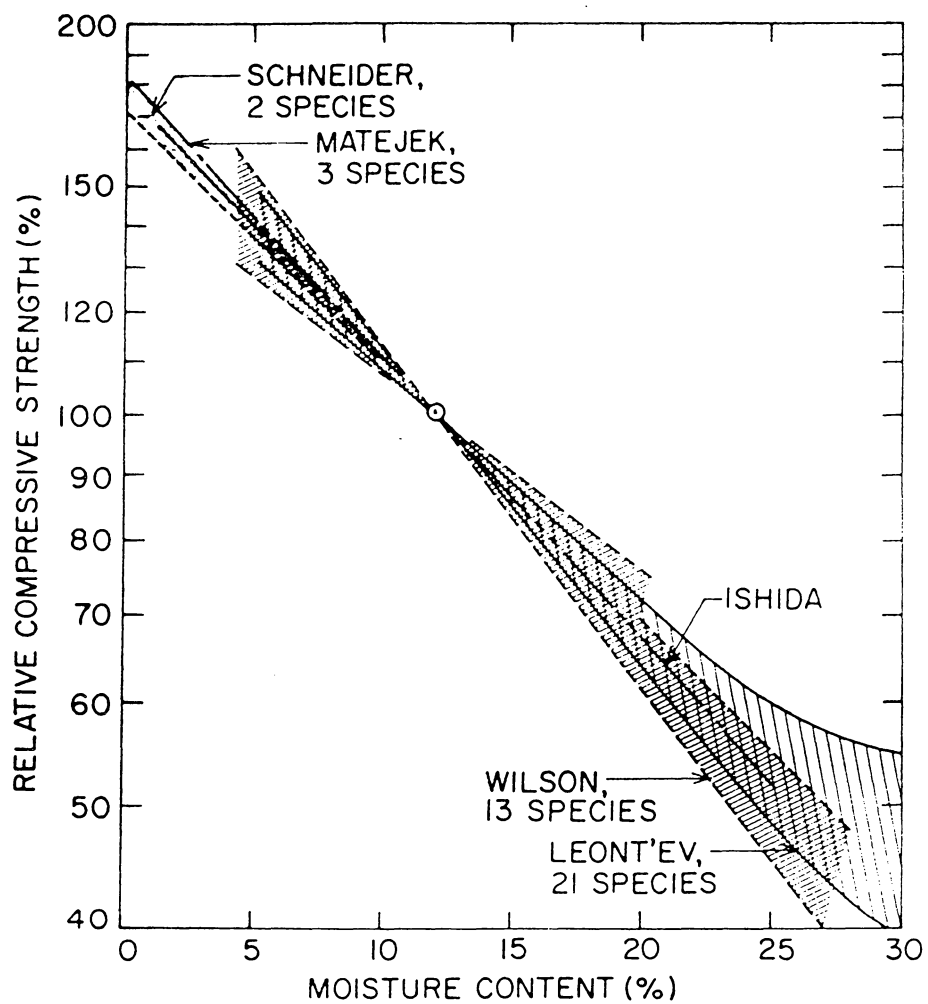


Figure 3.19. Effect of moisture content at about 20°C on compressive strength parallel-to-grain. 100% at 12% moisture content. (Gerhards, 1982)

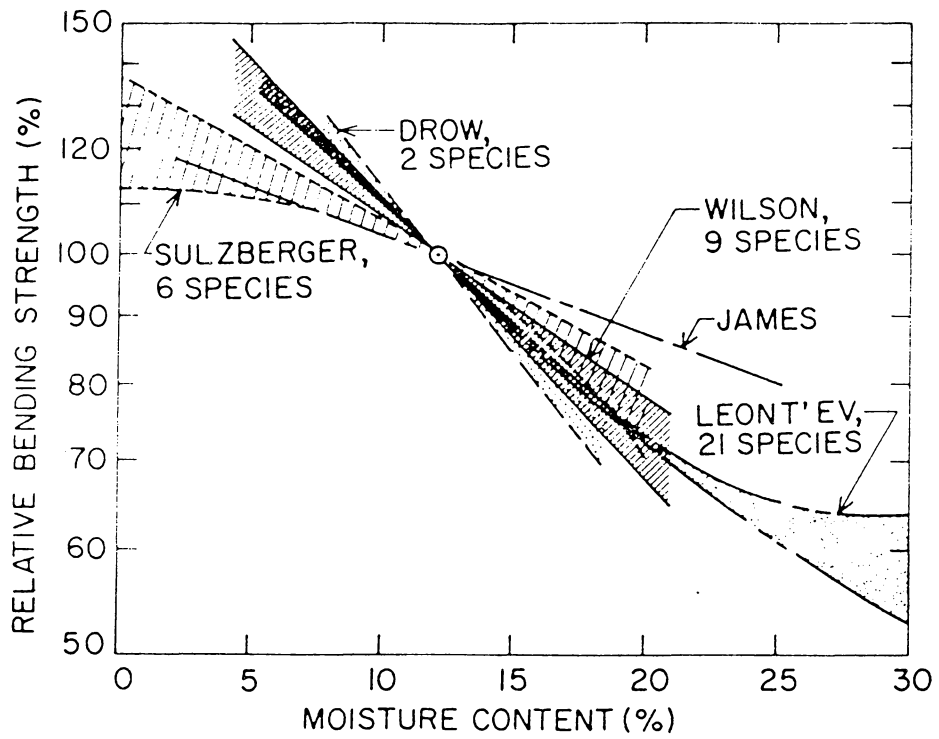


Figure 3.20. Effect of moisture content at about 20°C on bending strength of wood. 100% at 12% moisture content. (Gerhards, 1982)

Specific gravity

The substance of which wood is composed is actually heavier than water, its specific gravity being about 1.5 regardless of the species of wood (Forest Products Lab., 1974). In spite of this fact, the dry wood of most species floats in water, and it is thus evident that part of the volume of a piece of wood is occupied by cell cavities and pores. Variations in the size of these openings and the thickness of the cell walls cause some species to have more wood substance per unit volume than others and therefore to have a higher specific gravity. Specific gravity thus is an excellent index of the amount of wood substance a piece of dry wood contains. It is a good index of mechanical properties so long as the wood is clear, straight grained, and free of defects. It should be noted, however, that specific gravity values also reflect the presence of gums, resins, and extractives, which contribute little to mechanical properties.

The relationships between specific gravity and various other properties have been expressed, for clear straight-grained wood, as power functions. These relationships, given in Table 3.2, are only approximate. For any single species, more consistently accurate relationships can be obtained from specific test results.

Defects in the timber

As a natural material, wood has many defects caused by growing

conditions. Knots are among the most prevalent defects in timber. A knot is that portion of a branch which has become incorporated in the bole of the tree. The influence of a knot on the mechanical properties of timber is due to the interruption of continuity and change in direction of wood fibers. The influence of knots depends on their size, location, shape, attendant local slope of grain, and the type of stress to which they are subjected (Forest Products Lab., 1974).

Knots decrease most mechanical properties because (1) the clear wood is displaced by the knot, (2) the fibers around the knot are distorted, causing cross grain, (3) the discontinuity of wood fiber leads to stress concentration, and (4) checking often occurs around knots in drying. Conversely, knots actually increase hardness and strength in compression perpendicular to the grain and are objectionable in regard to these properties only in that they cause nonuniform wear or nonuniform stress distributions at contact surfaces (Forest product Lab., 1974).

Wood members loaded uniformly in tension are usually more seriously affected by knots than if loaded in other ways. The stress concentrations caused by knots depend not only on knot size but also on the location of the knots. Figures 3.21 and 3.22 show stress concentration factors varying with location when timber is subjected to tension.

In the top beam of the gallery set, knots on the lower side are placed in tension, and those on the upper side in compression. A knot has a marked effect on the maximum load a beam will sustain when on the tension side at the point of maximum stress; knots on the compression side are somewhat less serious.

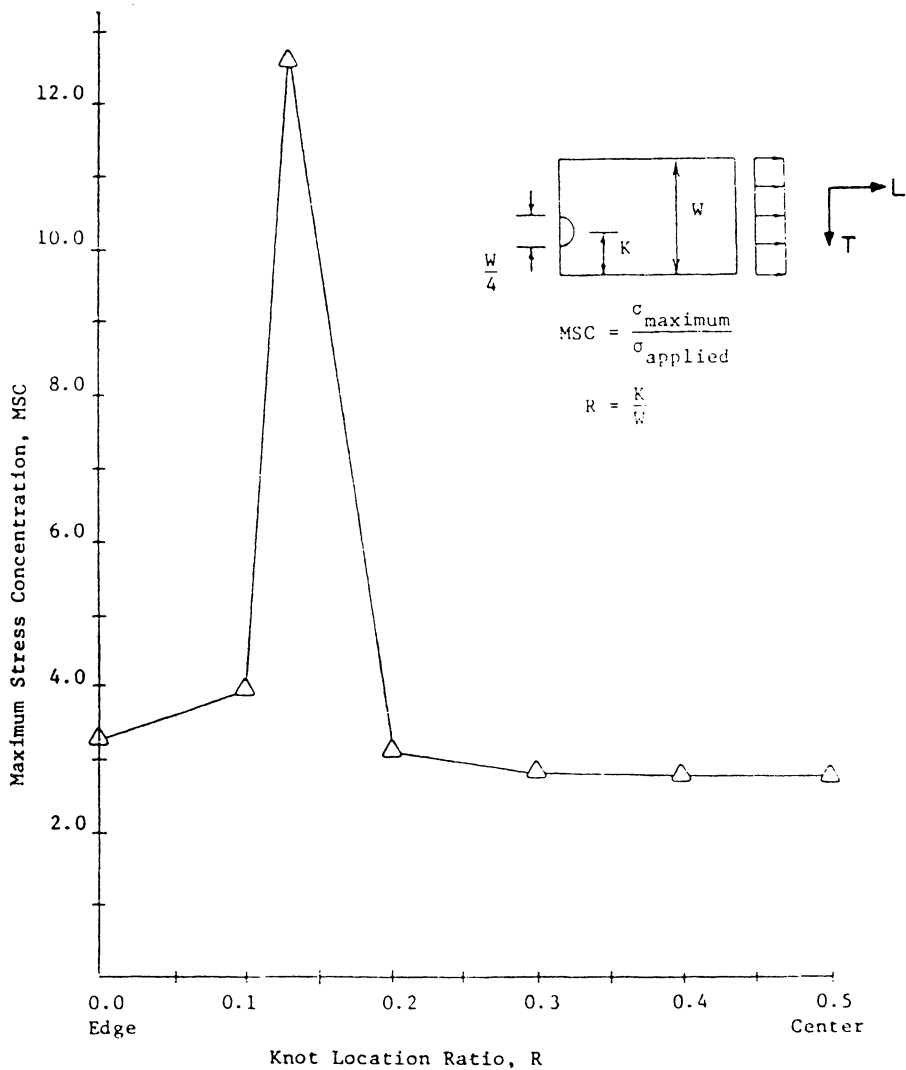


Figure 3.21. Longitudinal stress concentration factors for various knot locations. (Cramer, 1983)

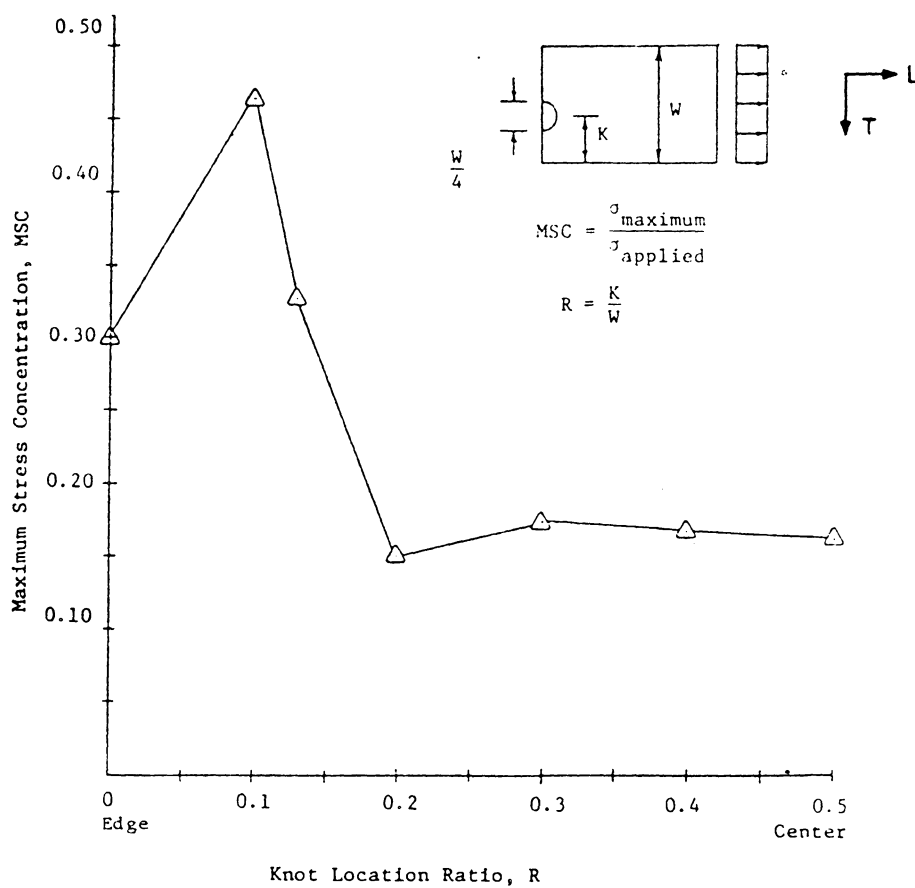


Figure 3.22. Transverse stress concentration factors for various knot locations. (Cramer, 1983)

In long square posts, knots are important in that they affect stiffness. In short or intermediate square posts, the reduction in strength caused by knots is approximately proportional to the size of the knot; however, large knots have a somewhat greater relative effect than do small knots. Tests have shown that failures in most timber posts begin at knots.

Natural bow

Natural bow is the inherent curvature of the post. When a post with natural bow is subjected to compression, the maximum compressive stress in the post is:

$$\sigma_{cc} = \frac{Q}{A} + \frac{Q.b.c}{A.e.r} \quad (3.37)$$

where Q, A and c have the same meaning as mentioned in Section 3.3, b is the arch height of the curved post, e the eccentricity of the neutral axis of pure bending and r the distance between the center of curvature and the point at which the maximum compressive stress occurs. Obviously the curvature of the post causes an additional stress term in the post. Therefore, whenever possible, straight posts ought to be used.

In this chapter, plain timber posts, timber cribs, and gallery sets are discussed. Plain timber posts represent the cheapest underground support. However, due to lack of yieldability, their use is limited. Thus, new types of yieldable timber supports are needed. This is the topic of next chapter.

CHAPTER 4 NOVEL TIMBER SUPPORTS

A conventional timber post exhibits a shortening of about 1.0 percent under compression before failing. Testing has shown that a four foot long timber post will fail in a buckling mode after yielding less than one inch (Faulkner, 1986). In many underground situations, a more yieldable support is needed. Timber cribs are one alternative. However timber cribs occupy more space than timber posts, their resistance to air flow is larger, and installation cost is higher. Therefore the use of timber cribs is also limited. Failure of the conventional timber supports to successfully deal with the roof control problems in some underground situations has resulted in the invention of some novel timber supports. Among others, the Micon Yield Capsule, the Super Post and the Wedge Prop are the latest developments.

The working mechanisms of these supports are discussed in this chapter, together with the results of the tests performed to determine their load-deformation characteristics. The results from the tests were analyzed by means of statistical and mechanical methods. Preliminary investigation indicates that these supports possess very good mechanical properties. Based on the preliminary investigation, suggestions are made for both the improvement of the supports and the method of investigation.

4.1 Micon Yield Capsule

The Micon Yield Capsule is used to improve the load-deformation characteristics of normal wooden posts.

The capsule, an aluminum cylinder that fits on the end of a post like a sleeve, is half-filled with a urethane foam. The foam has a cellular structure of elongated spherical cells with brittle cell walls. These cells are chemically designed to cure in such a way that they will collapse under a specific pressure. On loading, a layer of cells in the foam collapses. This allows a small amount of yield while the structure still maintains its load (Faulkner, 1985).

The Micon Yield Capsule is designed to behave as a hydraulic post while costing much less. A capsule may be used on the top or bottom of a post and installation is the same as for a regular post. In addition, the manufacturer claims that two posts with Micon Capsules will replace a crib set in a longwall tailgate. Other advantages are cost and labor savings and better clearance and ventilation. Also the posts may be designed for a specific system to provide needed yield-load characteristics in controlling roof failure.

The Micon Yield Capsule test was one of the first tests covered by this research. Consequently, the testing technique was rather simple and provided initial information for developing an organized and efficient testing procedure.

The capsules for this test were constructed from 12 inch high, 6 inch diameter aluminum cylinders. These had been filled in the factory with a 6 inch column of urethane foam designed to yield at a load of 35 tons during a deformation of 4.5 inches. The parameters of timber and yield capsule used in the test are listed in Table 4.1

The testing was carried out on the S.B.E.L. (T-10000), four-post, one million pound compression testing machine. A dial gauge was used to

Table 4.1 Parameters of Micon Yield Capsule Post

Parameters	Test 1	Test 2
Timber length	38.8	39.0
Timber girth	21.6	21.4
Capsule height	12.0	12.0
Inside diameter	6.0	6.0
Polyurethane height	6.0	6.0
Total length	45.3	45.0

(All units in inches)

record the deformation, while the load was observed from the testing machine load dial, which monitored the hydraulic pressure.

Prior to the testing, the oak timbers were trimmed to a length that would fit into the testing machine. Approximately 7 inches of bark was peeled off one end of each specimen to facilitate its snug insertion into the Micon Yield Capsule. The posts were assembled and the testing was carried out with the capsules on the top of the posts. Two standard wedges were used to "install" the post assembly in the testing machine as it would be installed in a mine.

During the test, each timber assembly was loaded at a constant rate while periodic readings of the load and dial gauges were recorded. The rate of loading in numerical terms is unknown, but the hydraulic pump was operated at its highest capacity during the testing to get the maximum rate of movement of the ram. These conditions might be comparable to a relatively quick increase or surge in the load on a timber support in an underground situation.

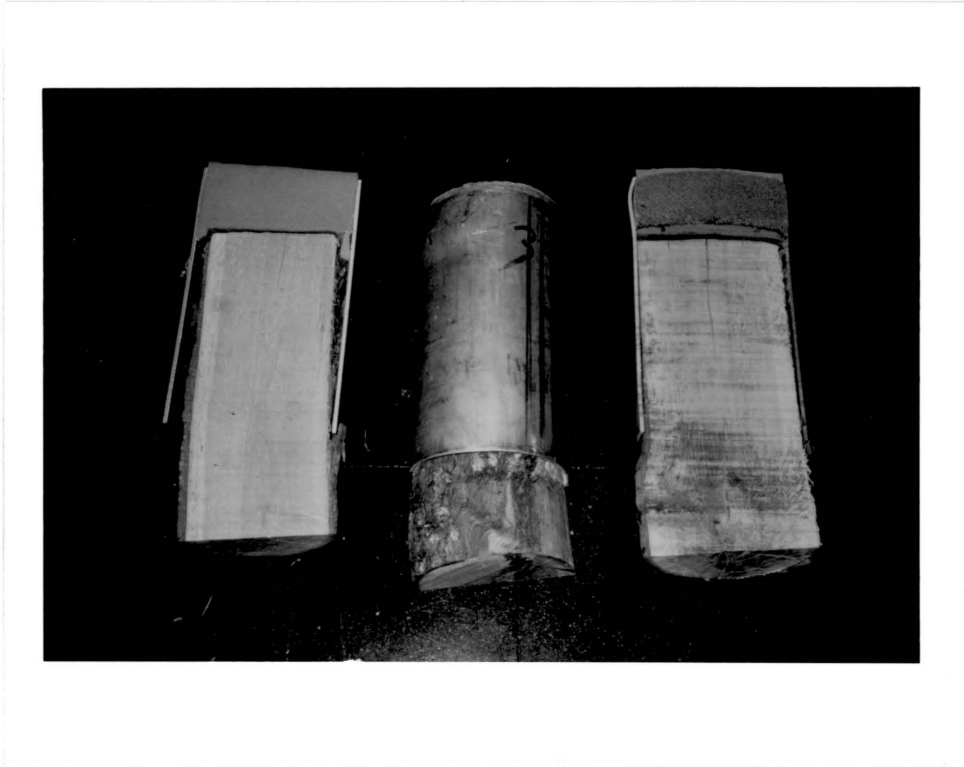
Due to the limit of extension of the hydraulic ram (4 inches), it was necessary in each test to unload the specimen midway through the test and install several inches of steel spacers to take up the yield that had already occurred. Each timber was then loaded to failure. Loading was continued after failure in order to determine post-failure load-deformation characteristics. The specimens were unloaded and removed at a point where further failure might cause damage to the equipment. Photographs of each post were taken after testing to show the failure effects on both the timber and the yield capsule. The capsule and the part of the timber inside it were sectioned longitudinally in

order to observe the internal effects of the high compressive load on the timber, urethane foam and the aluminum cylinder (figure 4.1).

The absolute deformation for each post was calculated from the changes in the dial gauge readings. Since this is a two stage test, an assumption was made in the data that the yield post did not deform in any way while the spacers were being inserted. In other words, the last deformation reading before installing the spacers became the first reading as timber was reloaded. In reality, the post would be relieving deformation during the time that the spacers were being installed.

The graphs in figures 4.2 and 4.3 were constructed from the data of the tests. The data used to draw the graphs has been revised from the original absolute deformation. The extraneous data collected due to installation of the spacers was eliminated from the original data. Furthermore, an assumption was made to shift the data from the second half of each test to the left to correspond with the highest load and deformation in the first loading. Each data point was manipulated to correspond with this assumption, therefore the graph for each post includes altered data points resulting in one continuous, smooth curve. These graphs are probably the closest approximation to the actual load and deformation that would occur during a one stage test.

Comparing figures 4.2 and 4.3 with figure 3.4, it can be seen that the Micon Yield Capsule posts are more yieldable than plain posts. For example, when the load was 95,000 lb., the plain wood post yielded only about 0.7 inches, while the Micon Yield capsule post yielded 3.7 inches. This characteristic of Micon Yield Capsule posts over plain wood posts can serve a very useful purpose in mine roof control. First, if the roof



4.1 Micon Yield Capsule.

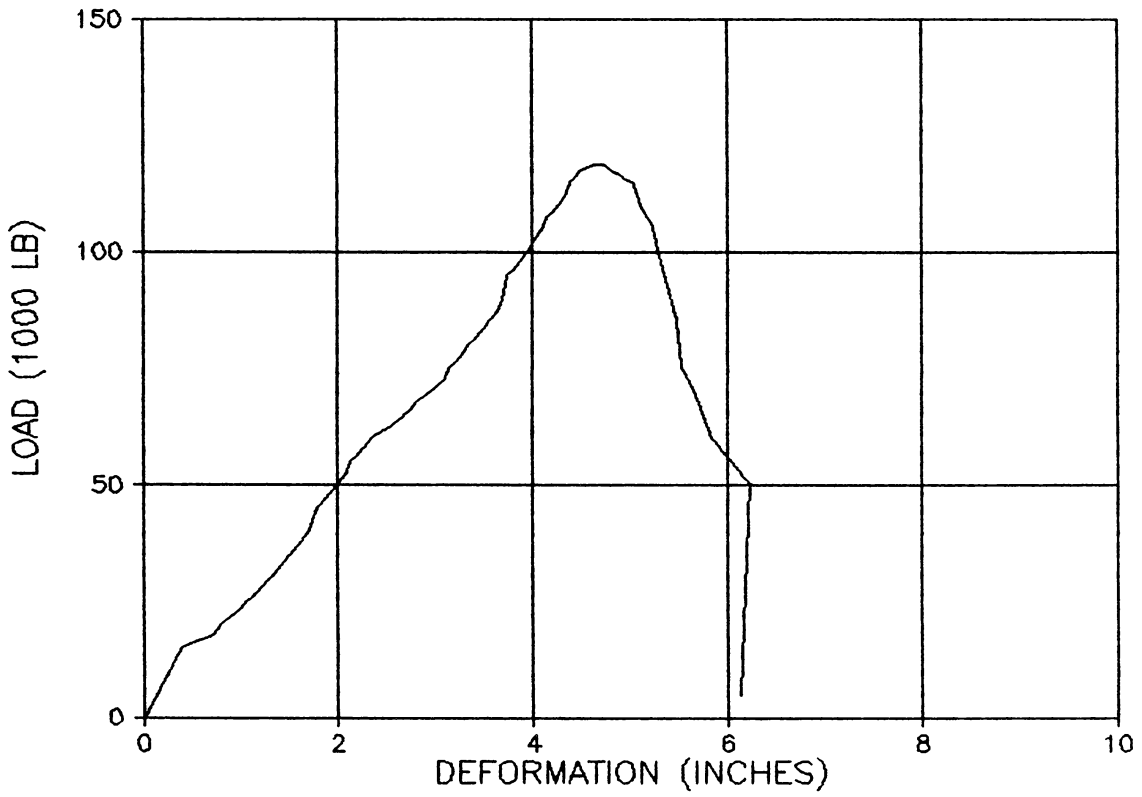


Figure 4.2. Load-deformation curve of Micon Yield Capsule, post 1. (Faulkner, 1985)

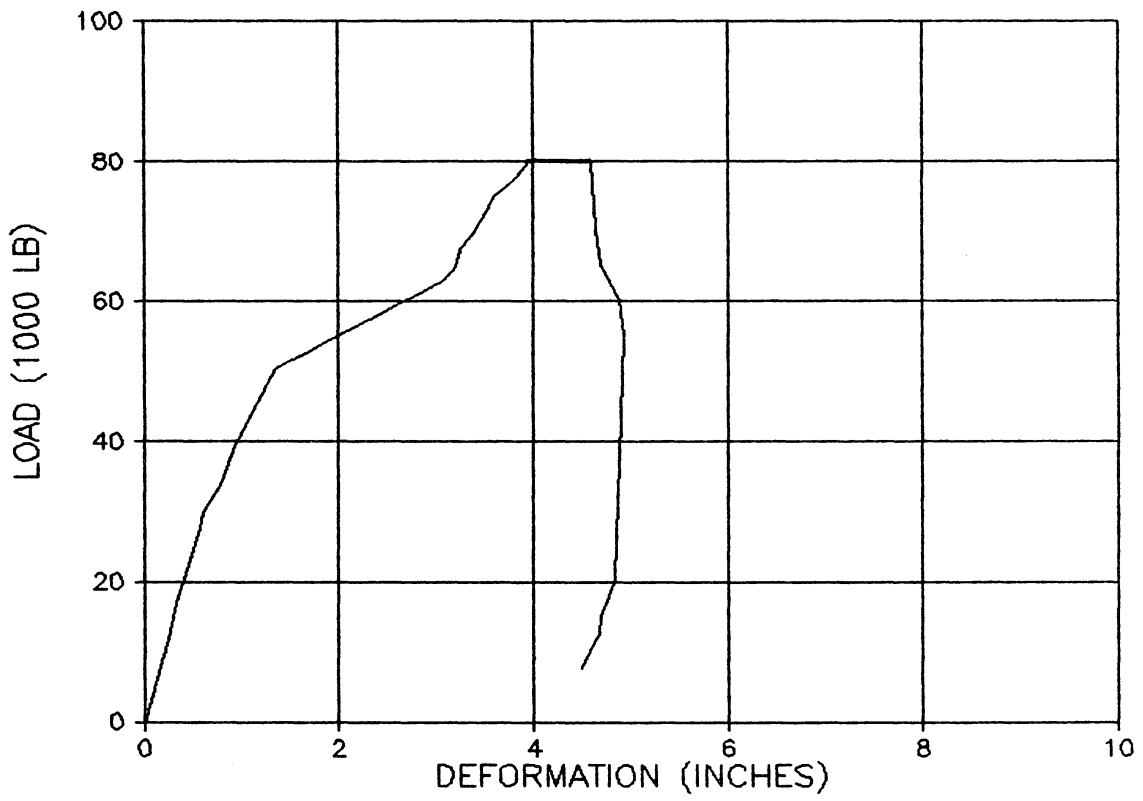


Figure 4.3. Load-deformation curve of Micon Yield Capsule, post 2. (Faulkner, 1985)

pressure is very large, the Micon Yield Capsule Post will yield very rapidly, giving an early sign of a possible problem, so that corresponding measures can be taken to avoid disaster. Second, under some conditions of weak or medium roof, a strong, rigid support can cause stress concentration in the support area, resulting in the weak roof breaking, while a more flexible support can avoid this problem.

The preliminary test has shown that the Micon Yield Capsule post has a similar load-deformation characteristic in the initial stage to the rapid-increasing resistance type of steel friction prop which will be discussed later.

The Micon Yield Capsule post is a relatively new development of the wood post. Except for the claims made by manufacturer, little has been known about its characteristics. In the preliminary tests defects still exist since the stroke of the test machine was too short for a one stage test and so the test procedure had to be accomplished in two stages. This test procedure and the consequent data process approach may cause the results presented to deviate from the actual situation. Also the number of tests carried out is not large enough to allow any positive conclusions to be made. Further laboratory testing should improve both the quality and quantity of the test, given planned improvements to the test machine and increasing the number of tests. Furthermore, some investigation needs to be undertaken underground to see the actual performance of the Micon Yield Capsule post in situ. Other factors, such as moisture content of the wood and specific gravity, will have to be considered.

4.2 The Super Post

Super Post is the trade name for a yieldable mine support that was to be manufactured in the United States by what was then the Stope Strata Corporation (now Minetech Industries Inc.).

The Super Post was developed a number of years ago in South Africa as the Volante Prop. It was developed as a type of elongate support for use in South African gold and uranium mines. Elongate supports are supports that use the natural strength of timber in compression along the grain. In addition, the timber is engineered, shaped, or encased in such a way that it can maintain its load while being compressed. The South African mining industry encountered a need for such supports because high stress conditions were encountered in the stopes of their very deep mines. The Volante Props have been used successfully in the support systems of South Africa to maintain the integrity of the hanging wall and footwall, and to prevent the separation of beds of rock strata. Increased productivity and lower support costs are noted advantages (Faulkner, 1985).

The Super Post is a 6 to 8 inch diameter straight log with a conical taper machined on one end. This taper also has concentric grooves in it over which fits a conical steel sleeve (see figure 4.4). The cone and grooves control the failure of the post during loading. The steel initially becomes more firmly seated on loading and then, as the load increases, the grooves close and the cone itself yields. The result is a stiff prop that yields a significant amount before failure.

The Super Post is designed to yield progressively in a stable manner

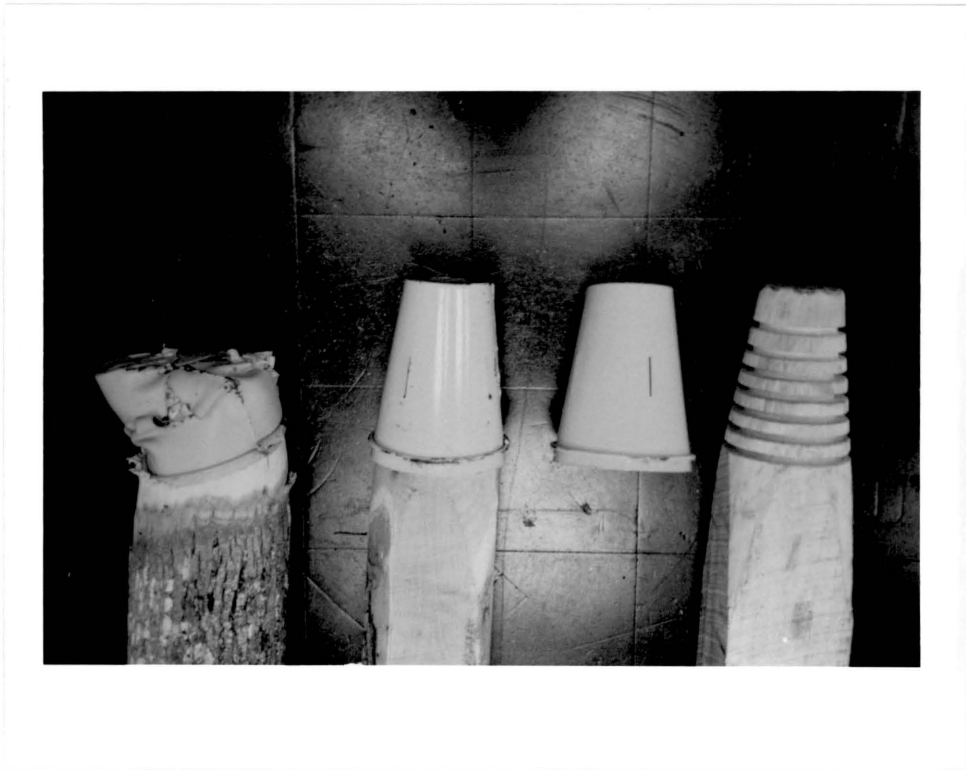


Figure 4.4(a). Structure of Super Post.
(Faulkner, 1985)

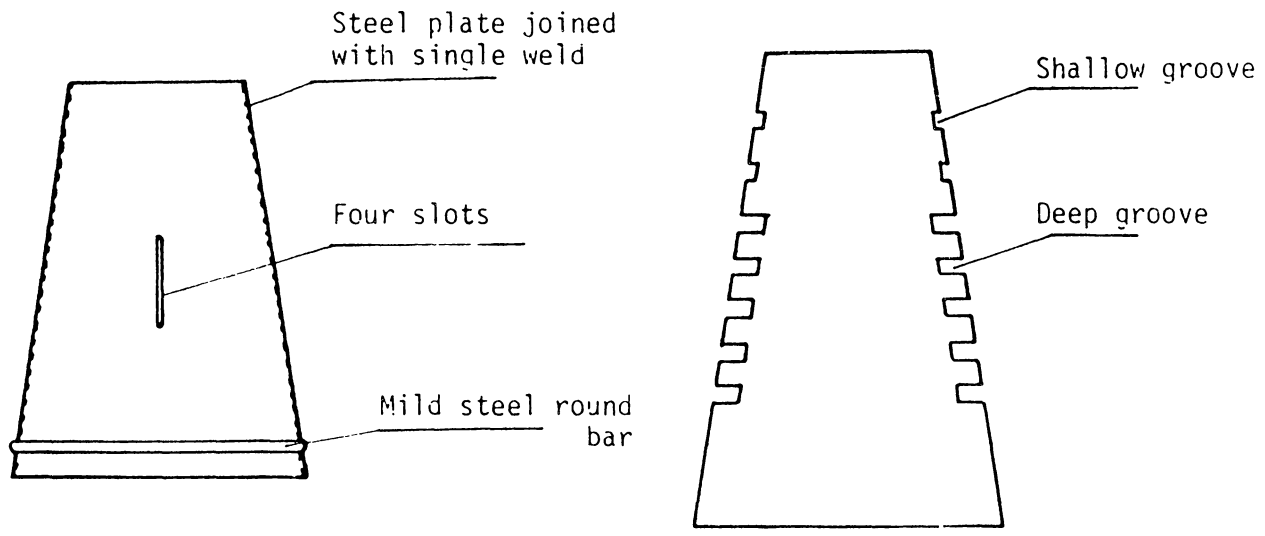


Figure 4.4(b). Structure of the Super Post.

at the machined end. Under normal loading conditions the controlled yieldability offered by the post is an advantage over a normal post which will buckle after only about one inch of yield. A number of steel cone and tapered end designs were used for Volante props in South Africa. The size, number of grooves, and shaping are dictated by particular support requirements, the depth of mining and stope sizes. The design for the Super Post in the United States is similarly based, but consideration has been given to the different mining conditions in the United States and to the use of different wood species.

Rigorous laboratory testing has shown that, on the average, an eight inch diameter Super Post will maintain a load of 50 tons as it deforms some six inches. These tests also indicated that a single Super Post was stronger than, more stable than, and carried twice the weight of a conventional wood crib over the same deformation. Consequently, from the manufacturer's report, use of the Super Post allows for greater maneuverability of men, equipment and materials and more adequate ventilation, since Super Posts take up less space than comparable cribbing and are easier to install. The labor cost-advantage of a Super Post over a crib is claimed to be 3 to 1, the in-mine transportation cost advantage is 6 to 1, and the materials cost advantage is approximately 2 to 1. The overall cost advantage is approximately 2.5 to 1, not including the difference in space requirements.

These claims would make the Super Post appear to be a viable option to cribbing that could be used extensively as a yieldable mine support. For coal mining in particular, the Super Post could be used for gateroad support in longwall mining, roof support in room and pillar mining, and

also during pillar extraction.

In this research, a sample of Super Posts of various wood types was tested in compression in a manner similar to that for the Micon Yield Capsule Posts. The Super Posts tested were of the Mark II variety. The cone steel was 14 gauge and the mild steel round bar welded to the base of the cone was 0.25 inches in diameter. The timber had a total of seven grooves machined into the end. The parameters of Super Posts tested are listed in Table 4.2. The test procedure and the data processing are similar to those for the Micon Yield Capsule. Figures 4.5 through 4.7 show three typical load-deformation curves derived from the test results.

In general, the load-deformation curve of the Super Post can be divided into two stages. The first stage is a slow yielding period. In this period the load increases rapidly, but the deformation changes little. The rigid metal cone is probably responsible for this phenomenon. When the load reached a certain value, the cone begins to yield and the deformation increases gradually. This is the second stage of the load-deformation curve of the Super Post. Through linear regression, the equations for each stage in each test are obtained as follows:

$$P = A + BL \quad (4.1)$$

The values of A and B are shown in Table 4.3. P and L are the load and deformation, respectively. The regression lines provide a reasonable approximations of the actual load deformation curve.

In the above equations, B is equal to $\Delta P/\Delta L$ which is the load to

Table 4.2 Parameters of Super Posts

Wood Type	Post	Length (in.)	Cross-section	Area (sq. in)
Poplar	A	41.4	Square	37.5
Locust	B	40.3	Round	44.2
Locust	D	39.5	Round	41.3
Locust	F	40.8	Square	36.0
White Oak	C	40.5	Round	34.5
White Oak	E	40.8	Square	36.0
White Oak	G	41.0	Square	36.0

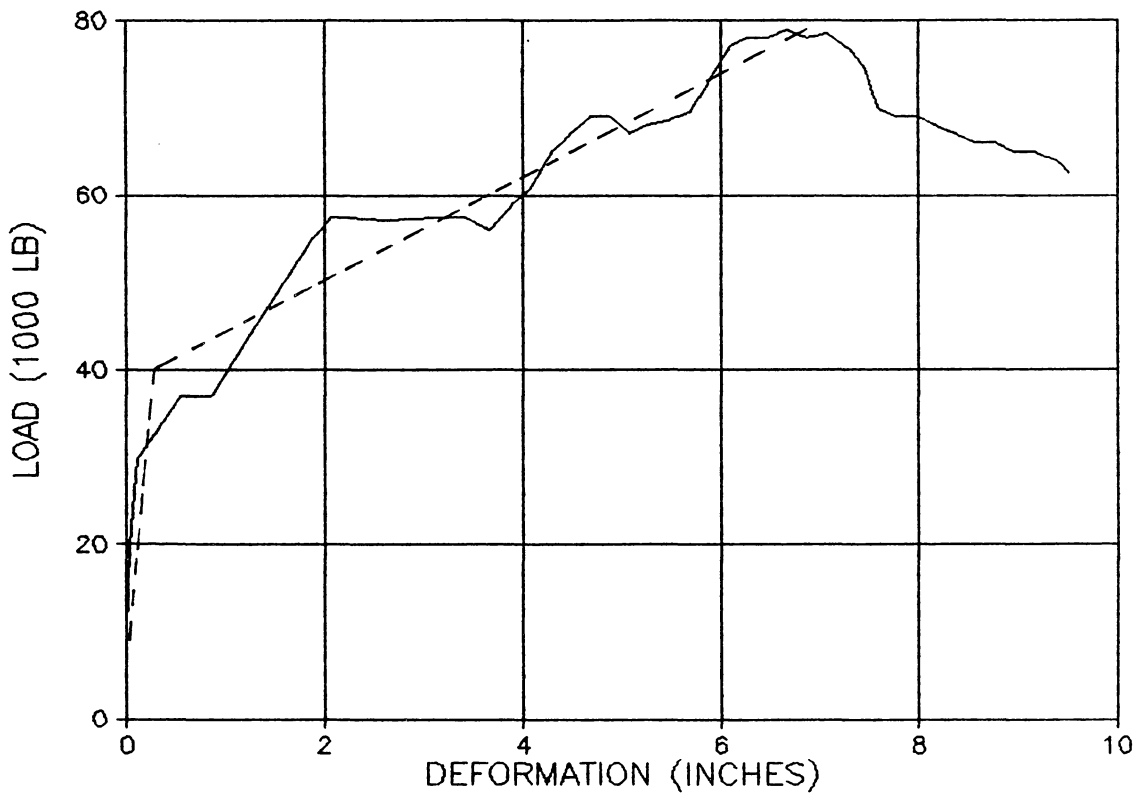


Figure 4.5. Load-deformation curve of Super Post, Square poplar A. (Faulkner, 1985)

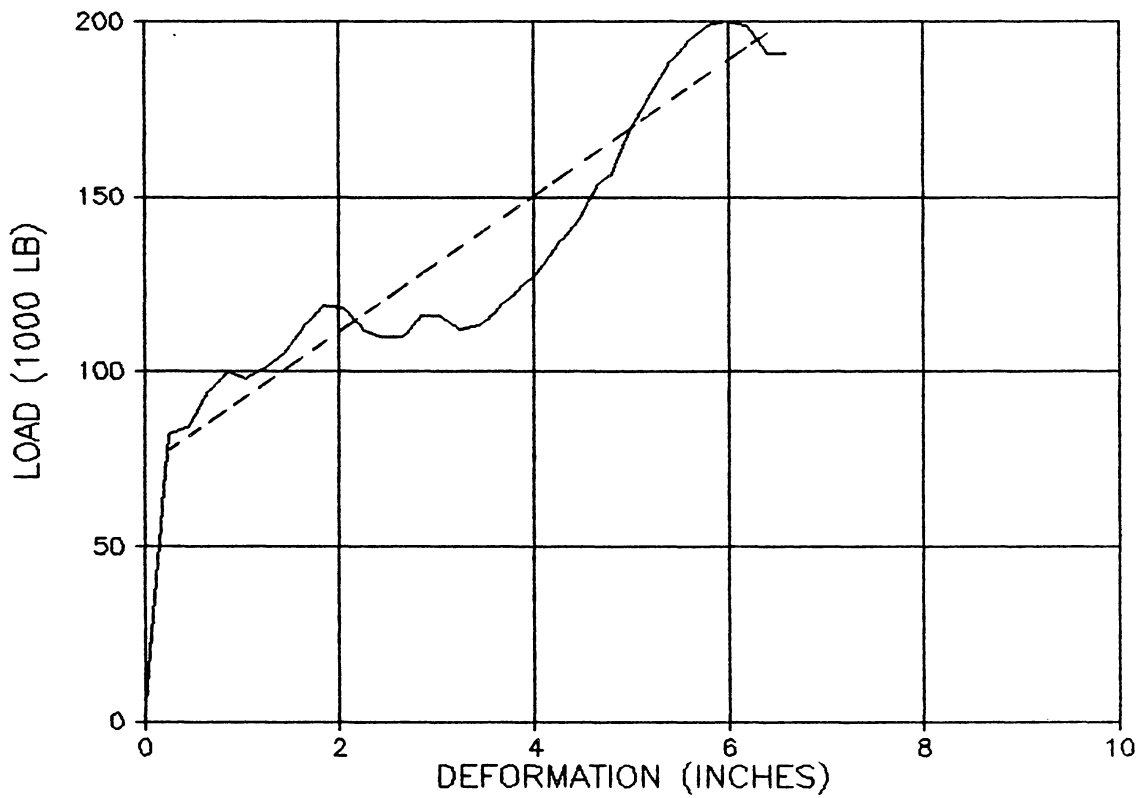


Figure 4.6. Load-deformation curve of Super Post, unfinished locust B. (Faulkner, 1985)

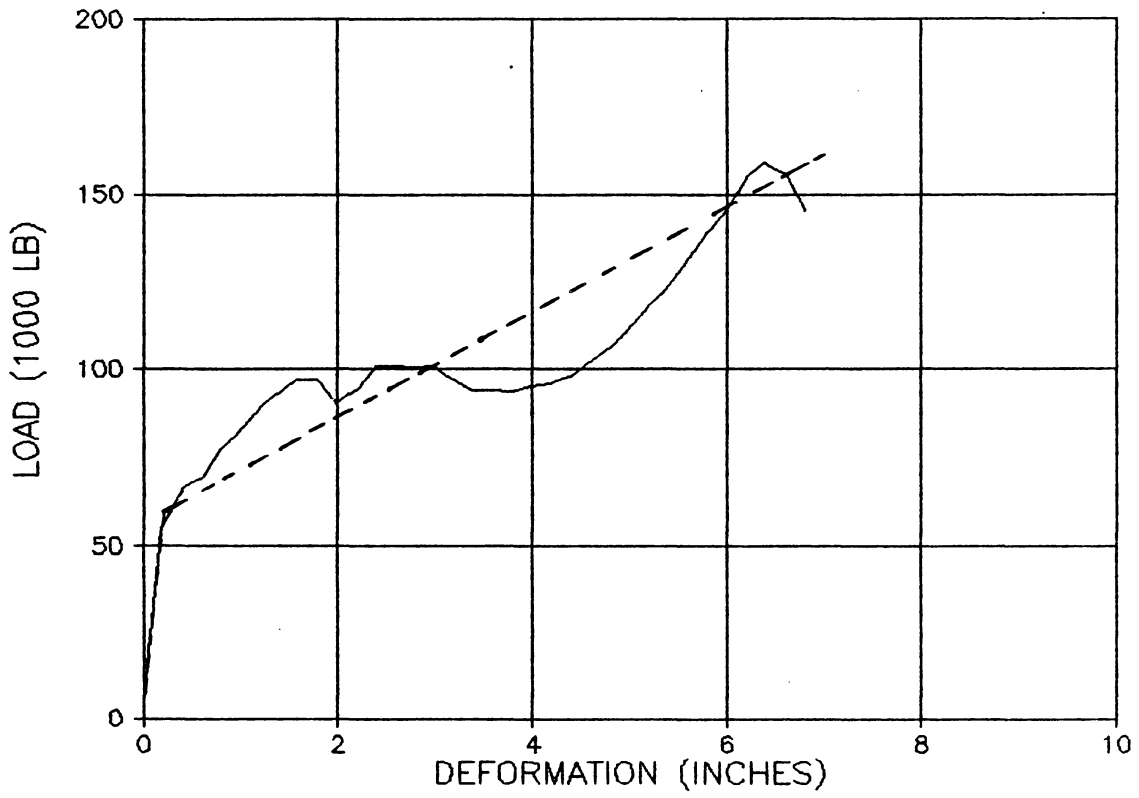


Figure 4.7. Load-deformation curve of Super Post, unfinished white oak C. (Faulkner, 1985)

Table 4.3 Constants From The Regression Equation

Timber Type	Stage	A (1000 lbs)	B (1000 lbs/in.)
Square Poplar A	1	15.06	140.34
	2	37.80	6.04
Unfinished Locust B	1	1.64	309.50
	2	68.23	18.96
Unfinished White Oak C	1	3.97	221.24
	2	66.08	11.31
Unfinished Locust D	1	-73.34	239.00
	2	51.93	27.10
Square Oak E	1	7.55	218.00
	2	58.64	18.19
Square Locust F	1	-2.75	217.50
	2	95.62	23.20
Square White Oak G	1	2.17	305.00
	2	63.92	13.07

deformation ratio. The smaller the ratio, the more yieldable the post. The locust Super Post is the least yieldable, oak was next and poplar yielded the most under the same loading condition. The slight differences in length and area of the specimens were ignored in the analysis process, but will be examined in future research.

The Super Posts exhibited average yields of between 5 and 7 inches at maximum load in the two-stage testing procedure. Some posts continued to yield after the maximum load was reached while still maintaining a very high load. Consequently, the qualitative performance of the Super Post as a yieldable support seems excellent.

During the Super Post tests the metal cone followed a consistent pattern to failure not dependent on wood type or cross-section. As loading progressed the cone initially exhibited a single bulging area around the circumference. This was probably due to the complete compression of the first groove in the machined end of the timber. As loading continued several more bulges were noted, probably corresponding to additional grooves. Usually two to three bulges had appeared before the metal cone began to tear along the vertical slots. Although a number of small undulations appeared consistently in the graphical plots, these did not seem to correspond very well with the visual observations of bulges in the cone; however, they do seem related. These graphical undulations continued even after the cone began to tear.

The metal cone tears and splits vertically in several places as testing continues. Some unfinished timbers began losing sap due to the high compression in the upper zone. Many popping and creaking noises were also noted. As the wood in the cone disintegrated, the metal cone

usually ripped completely down the side, leaving only the steel ring to confine the timber end. The remaining wood and metal was a deformed and crushed mass. In some tests the timber buckled and burred at this point or leaned so badly that testing could not continue. In a number of tests the steel band snapped loudly in tensile failure and the load dropped abruptly and then continued to decline. A predictable failure mode such as this is desirable in underground situations because the conditions of support can be visually monitored.

The general load-deformation graphs from the Super Post testing resemble that of a slow-increasing resistance type of steel friction prop which will be mentioned in Chapter 6. The second stage of the load curve of the Super Post is similar to that of a crib. The yield is gradual as the load increases and the top of the graph is rather flat and does not exhibit a sharp drop as a plain post would.

The general results of the tests seemed to be consistent and showed that the performance of the Super Post was as predicted. It is more difficult to draw specific conclusions and only a few slight trends were noted. Additional controlled testing will be necessary since the testing method needs to be improved and account should be taken of the other factors mentioned previously. Although some measurement of the moisture content in the posts has been done, nothing can be said about it since, to-date, little data has been obtained.

4.3 Wedge Props

The wedge prop is another novel underground mining support.

Although some initial tests have been done in South Africa, not much has been known about its mechanical behavior in the United States. In order to further explore the properties of wedge props, Minetech Industries Inc., which makes the wedge props in the United States, sent six prototypes of its product to the rock mechanics laboratory in the Department of Mining and Minerals Engineering at VPI and SU for laboratory testing.

The test results show that the wedge prop is very promising. In this section the specifications of the props are given, the test equipment and procedure described, the results analyzed and future improvement of the props and the test discussed. In order to have a better understanding of the test results, the working mechanism of the wedge prop is first discussed.

4.3.1 The Working Mechanism of Wedge prop

The structure of a wedge prop is shown in figure 4.8. Its working mechanism is not easy to discuss without making some assumptions since there are a large number of factors affecting its performance.

Suppose that the wood log of the prop is clear wood, the cross-section of the wood log is a circle, the thickness of the wedge bottom is negligible, and there is no prestress between the pod and the wedges. Then at the beginning of the loading, the pod take up most of the load and the wedges slide down slightly. As the load increases, the pod and the wedges begin to expand. If the expansion along the radial direction is u , then the steel band imposes a distributed load q on the

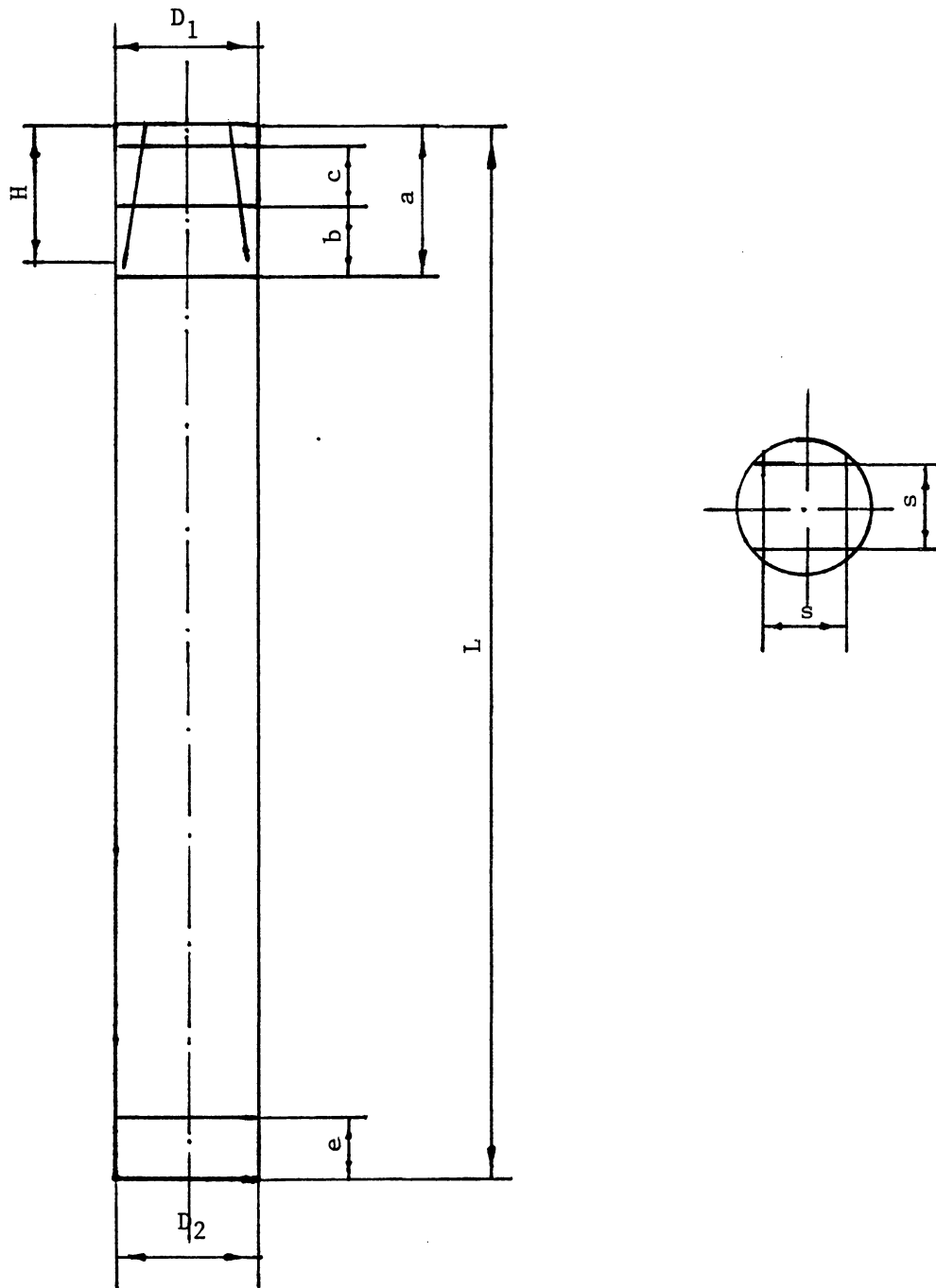


Figure 4.8. Structure of the wedge prop.

wedges. q can be expressed as:

$$q = \frac{4tE_s u}{D^2} \quad (4.2)$$

where

E_s = the Young's modulus of the steel band;

t = thickness of the band;

D = the diameter of the prop.

From figure 4.9 the total force normal to the inner plane of the wedge prop can be obtained by integration:

$$\begin{aligned} Q &= 0.5 \int_0^{\alpha/2} qwD \cos \theta d\theta \\ &= 0.5qwD \sin(\alpha/2) \end{aligned} \quad (4.3)$$

where

w = the width of the steel band;

α = arch angle of the wedge cross-section where the band is located.

In order to make the wedge slide down further, the load acting on the top of the wedge should be larger than F . From figure 4.10

$$\begin{aligned} F \cos \beta - Q \sin \beta - f(F \sin \beta + Q \sin \beta) &= 0 \\ F &= \frac{Q(\sin \beta + f \cos \beta)}{(\cos \beta - f \sin \beta)}. \end{aligned} \quad (4.4)$$

Substituting equations 4.2 and 4.3 into 4.4,

$$F = \frac{(2tE_s uw/D)(\sin \beta + f \cos \beta)}{(\cos \beta - f \sin \beta) \sin(\alpha/2)}. \quad (4.5)$$

When the load exceeds F , the wedge will slide down, the band will be

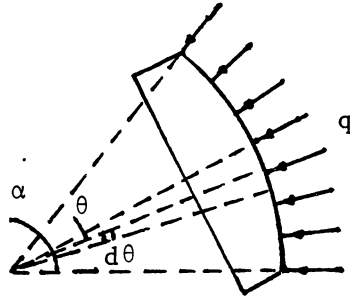


Figure 4.9. The distributed load created by the band.

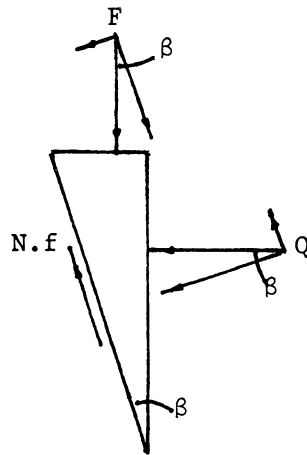


Figure 4.10. Freebody diagram of the wedge.

expanded further and u will increase. Thus the value of F will be raised and the wedge reaches a new equilibrium state. At the same time, the pod undergoes elastic deformation. The u and F values increase alternately until the pod yields. The portion of the pod above the top band will yield first. Upon the failure of the top section of the pod, the first band will be expanded severely. Eventually the band will break when its tensile strength is exceeded. A mushroom head will appear (figures 4.11 and 12). After the appearance of the mushroom head, the situation becomes more complex since the deformation is the result of compression both parallel and perpendicular to the wood grain. The second band will also break as load increases.

The third band is located in the solid wood section. The relationship between the load and the reaction of the band when it is expanded is:

$$q = \frac{[(4P\mu_w)/(\pi D^2)]}{((DE_w/2tE_s)+1-\mu_w)} \quad (4.6)$$

where

μ_w = the Poisson's ratio of wood;

E_w = the Young's modulus of wood;

P = the load acting on the prop;

and other symbols have the same meanings as mentioned previously.

The stress in the band can be expressed as:

$$\sigma = \frac{(4P\mu_w)/(\pi D^2)}{[E_w/E_s + (2t/D)(1-\mu_w)]} \quad (4.7)$$

It is known that



Figure 4.11. Side view of the mushroom head.



Figure 4.12. Top view of the mushroom head.

$$\sigma_w = \frac{4P}{(\pi D^2)} \quad (4.8)$$

and let

$$k = \frac{\mu_w}{[E_w/E_s + (2t/D)(1-\mu_w)]} \quad (4.9)$$

then

$$\sigma = k\sigma_w \quad (4.10)$$

where

σ_w = the compression stress in wood;

σ = the tensile stress in the steel band.

If the compression strength of the wood and the tensile strength of the steel are known, then, based on equations 4.7 through 4.10, it can be determined which material will fail first, the wood or the steel. These formulas can also be applied to design the wedge prop and to predict the failure mode of the remaining portion of the prop after the failure of the wedge section. For example, if the steel band is designed to fail first, the prop probably will fail in a split mode due to the tensile stress along the radial direction. Otherwise the prop may fail in buckling mode. Finite element analysis in this research indicates that, by tying the steel band around the post, the tensile stress along the radial direction can be reduced dramatically.

4.3.2 The Specifications of The Wedge Props Tested

The specifications of the wedge props are listed in Table 4.4 and

Table 4.4 Specifications of the Wedge Props

Prop Number	No.1	No.2	No.3	No.4	No.5	No.6
Wood Species	Red oak	Red oak	Hickory	Hickory	Locust	Locust
a	13.0	10.4	12.4	17.2	13.0	15.1
b	6.4	5.5	5.9	9.0	6.0	7.3
c	3.4	2.3	4.1	5.6	3.5	4.3
D1	6.0	5.9	6.8	7.0	6.0	6.0
D2	7.4	6.5	7.0	8.0	6.5	7.5
e	6.0	6.0	6.0	6.0	6.0	6.0
L	45	45	45	45	45	45
H	10.0	6.0	6.3	6.5	6.3	7.5
Band type	wire	strap	wire	strap	wire	strap

(All unit in inches)

the meaning of the symbols in the table are given in figure 4.8. The size of the pod top is 4 by 4 inches. The wire is made of mild steel and its diameter is 3/16 inch. The tensile strength of the wire is between 50,000 and 60,000 psi. The strap is made of steel and its thickness and width are 1/32 and 1.5 inch respectively. The tensile strength of the strap is less than that of the wire.

4.3.3 Equipment Used And Test Procedure

The tests were performed with a one million pound loading frame manufactured by S.B.E.L.. This machine has manual control of the hydraulic pressure applied to the load ram and the ram load is read directly from a hydraulic pressure gauge. The deformation is read from an AMES gauge which measures the displacement of the hydraulic ram.

The moisture content in the timber was measured before each test. All the props tested had a moisture content higher than thirty percent in the timber, indicating that the timber was saturated. The visible defects in the timber were also recorded. The wedge props were loaded directly between the upper and lower platens of the test machine. The average loading rate was 4000 lbs/min. Figures 4.13 and 14 show a wedge prop before and during testing, respectively .

Since the deformations of the wedge props are larger than the stroke of the hydraulic ram, it was necessary to unload the test specimen every time when the deformation exceeded 4 inches, and spacers were installed between the specimen and the testing platen to take up the space so that the specimen could be reloaded. Sometimes even this procedure could not



Figure 4.13. A wedge prop before testing.



Figure 4.14. A wedge prop under testing

make the prop fail on this testing machine because the deformed head of the wedge prop would spring back when unload, making the installation of the spacer difficult.

This test procedure complicated the results of the testing. In order to observe the load-deformation characteristics of the props, the additional data due to the cycling loading have been eliminated. The load-deformation curves for all the tests are plotted in figure 15 through figure 20. These curves may deviate from the results of a one-stroke test, except for in the case of wedge prop 2, which failed in a one-stroke test.

4.3.4 Analysis of The Result From The Tests

Based on the testing results shown in figures 4.15 through 4.20, the behaviors of the wedge props under uniaxial load can be classified into two categories. The main distinction between the two categories lies in the deformation characteristics of the prop after the pod fails. In the first category the load continues increasing as the prop deforms, after an initial decrease due to the failure of the pod. In the second one the load is approximately constant, with a certain degree of fluctuation after the pod fails. The two-category classification may not always be appropriate, but at least it can be applied to a normal wedge prop.

The mechanical behaviors of the wedge prop may be affected by many factors such as the distance between the bands, the strength of the band material, the depth of the sawcut, the tightness of the band, the properties of the wood log, etc. In the following section each test is

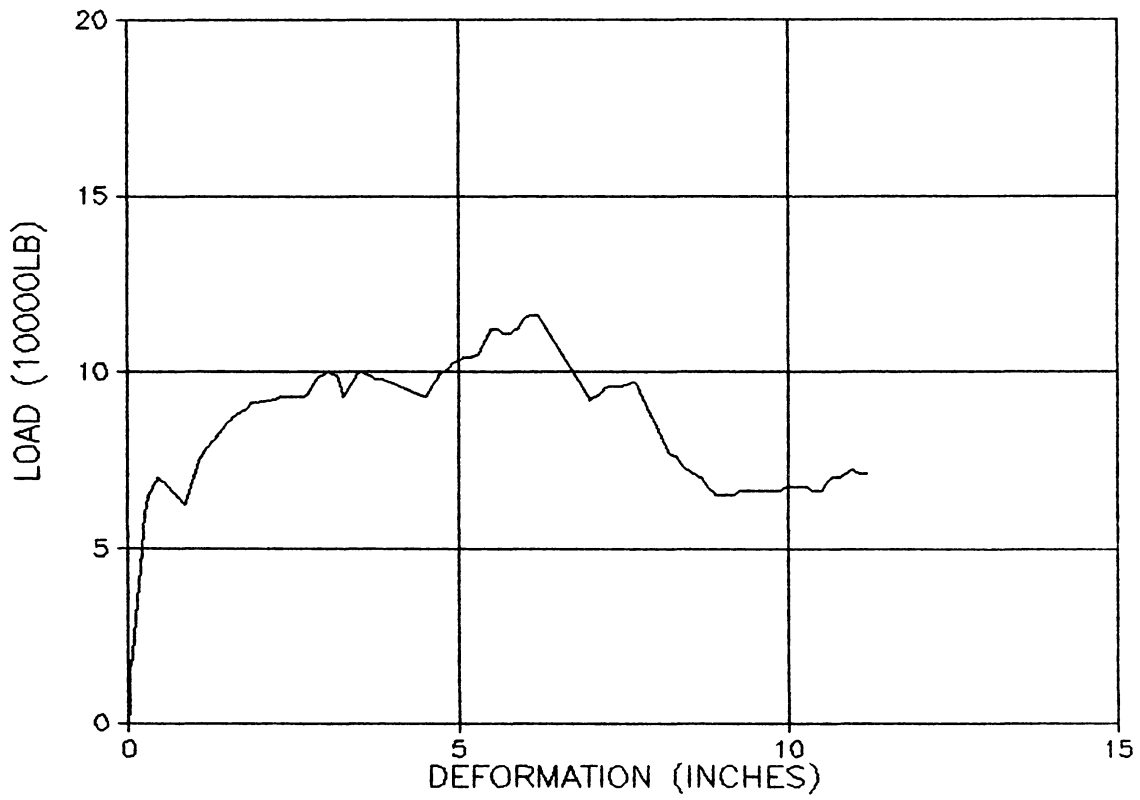


Figure 4.15. Load deformation curve of wedge prop 1.

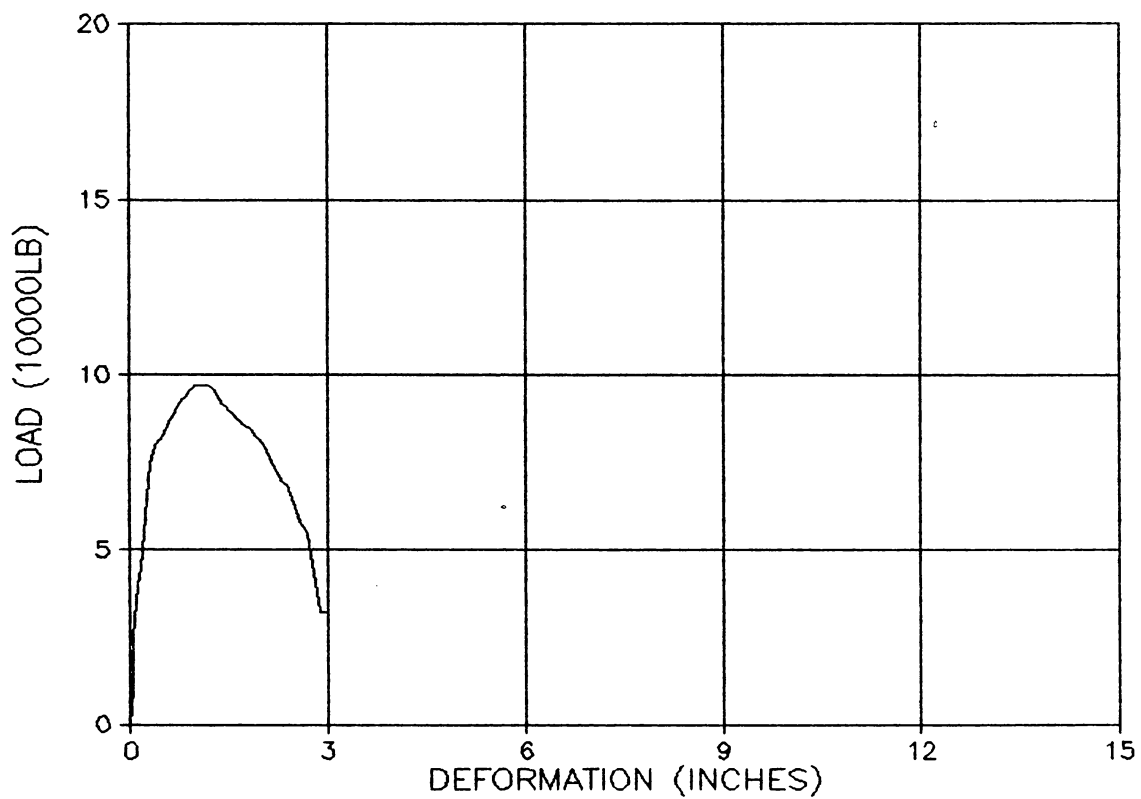


Figure 4.16. Load-deformation curve of wedge prop 2.

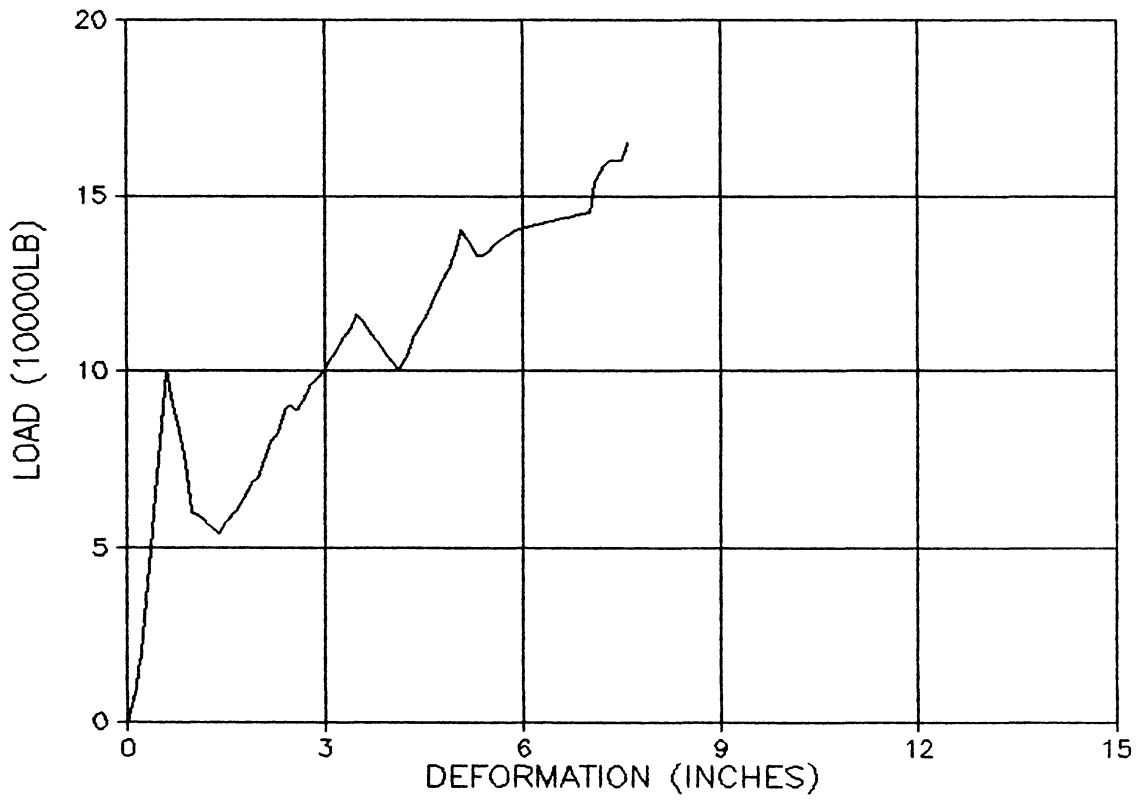


Figure 4.17. Load-deformation curve of wedge prop 3.

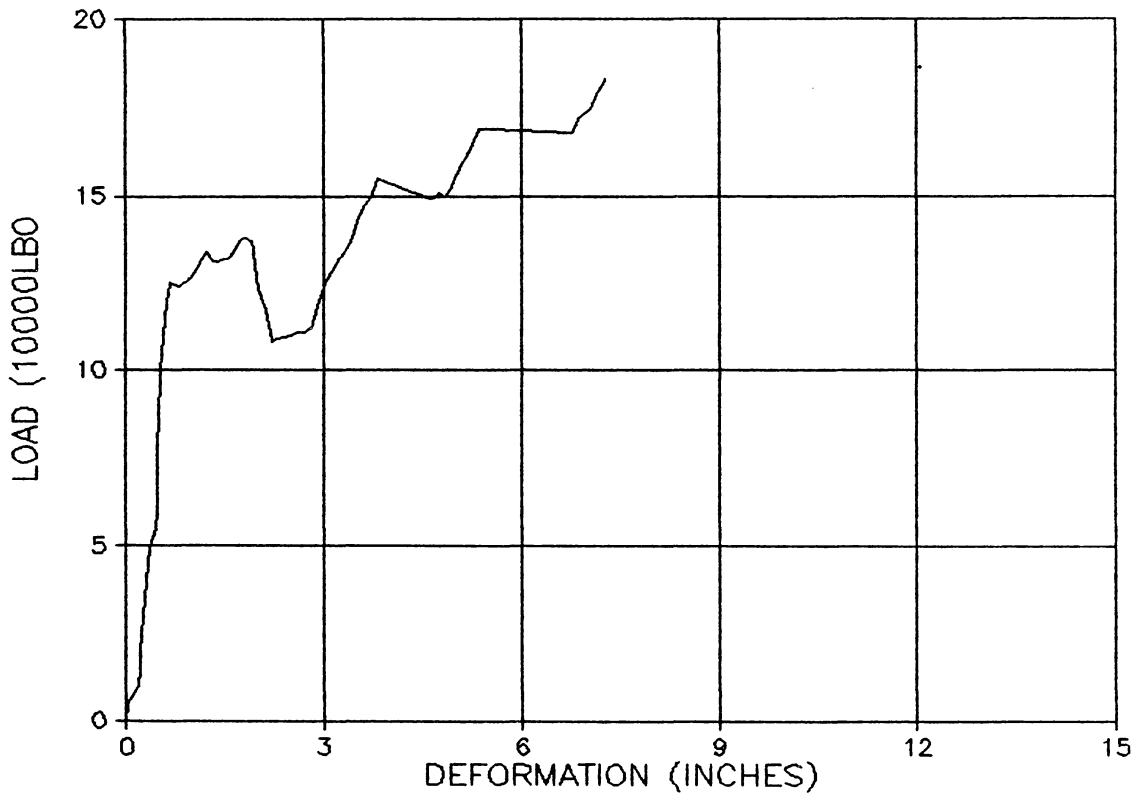


Figure 4.18. Load-deformation curve of wedge prop 4.

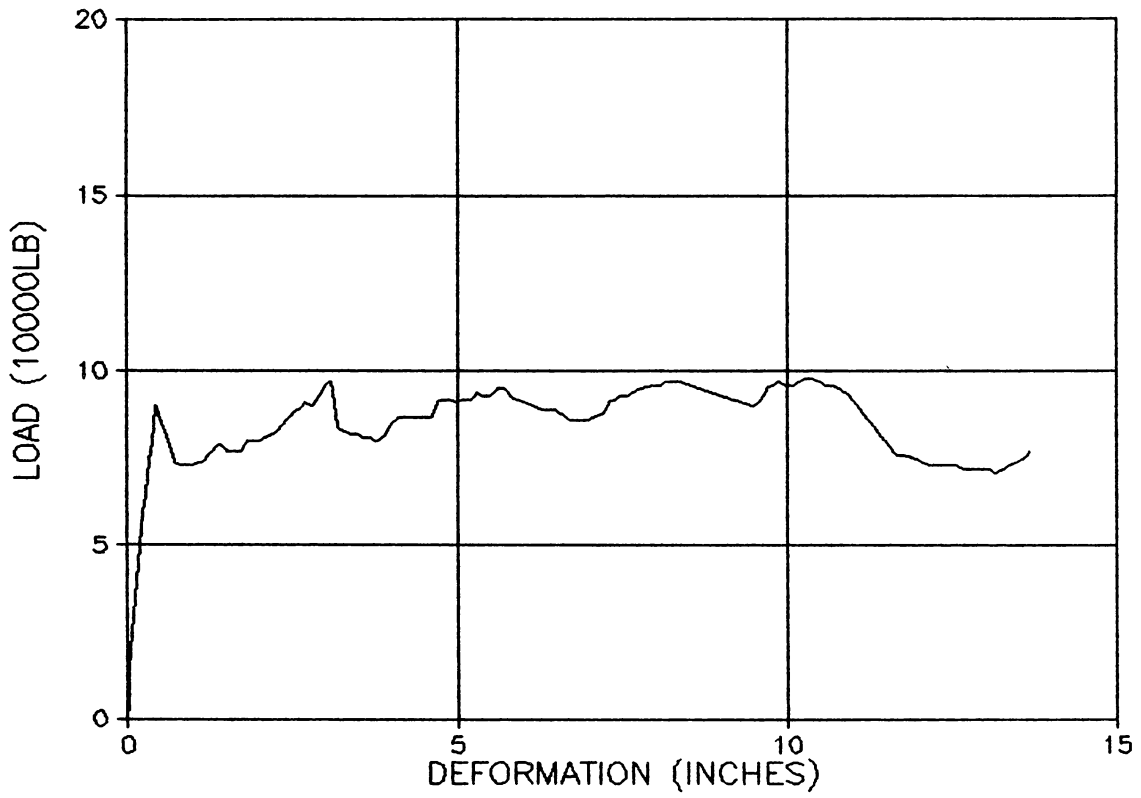


Figure 4.19. Load-deformation curve of wedge prop 5.

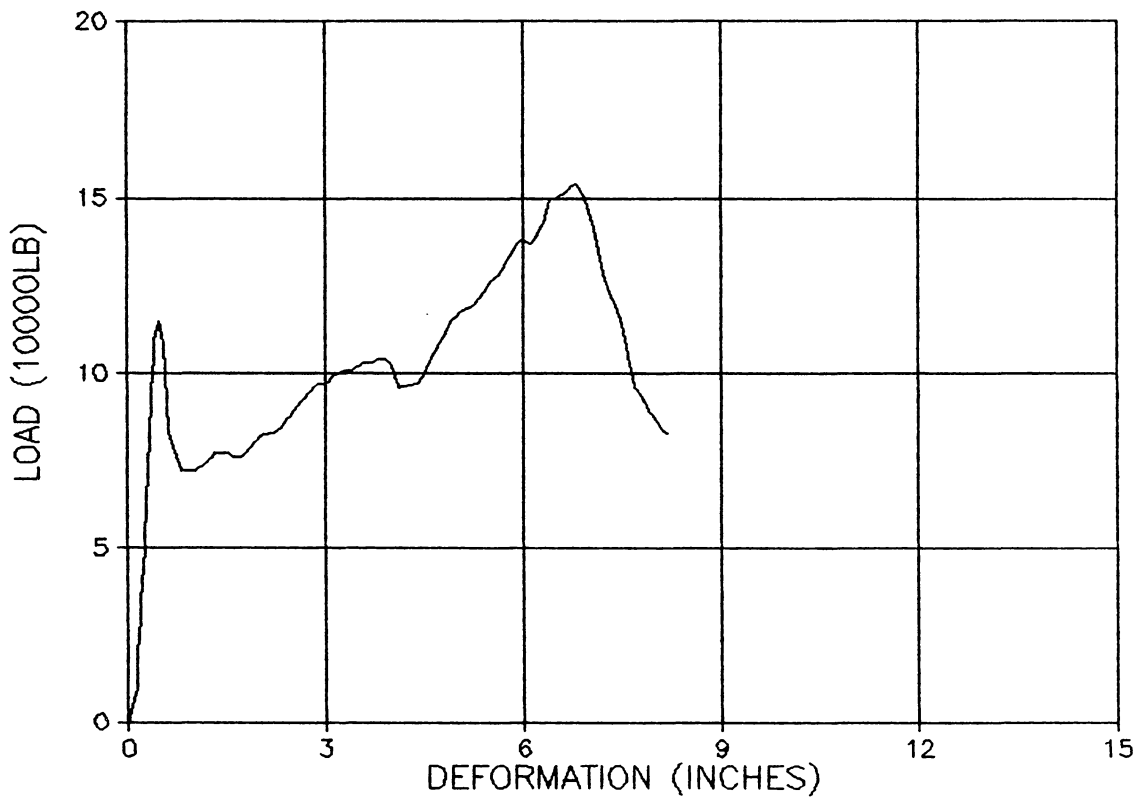


Figure 4.20. Load-deformation curve of wedge prop 6.

analyzed individually and possible factors attributed to the test results are discussed. Note that the period prior to the yielding of the pod is referred as the first stage and the period after the yielding is referred as the second stage.

Wedge prop 1

The load-deformation curve of this prop (figure 4.15) can be classified into the second category. The pod began to yield at 70,000 pounds. The stiffness of the prop in the first stage was 172 thousand pounds per inch. The load dropped only slightly upon the yielding of the pod, indicating that the wedges were properly tightened. After the pod yielded, the load fluctuated with an average load of 87,000 pounds and a standard deviation of 16,000 pounds. The maximum load at this stage was 116,000 pounds and the minimum was 62,000 pounds. The large standard deviation shows that the load was not very stable in the second stage.

The total deformation of this prop was 11.3 inches.

Wedge prop 2

This prop is an exception. Its load-deformation curve can not be classified into either of the two categories (figure 4.16). The prop head did not yield before the prop buckled. The stiffness of the prop was very low, only about 85 thousand pounds per inch which was the lowest among the six props. The maximum load was 95,000 pounds and the effective deformation only about 2 inches. Possible reasons for the

poor performance of this prop can be attributed to the following factors:

1. The three bands were placed too close to one another. The distance between the first and the second band was only 2.3 inches which was much shorter than other props.

2. The bands were placed too tightly on the wedges (figure 4.21). This made the head even stronger than the timber log itself.

3. Knots existed in the wood log.

Wedge prop 3

The load-deformation curve of this prop (figure 4.17) can be classified into the first category. The pod yielded at 100,000 pounds, and then load dropped dramatically. The reason for the load drop was that the sawcut was too wide (as shown in figure 4.22) and the bands were not tightened properly. The load eventually recovered from the drop and continued to increase as the head deformed. The stiffnesses of the prop were 184,000 pounds per inch for the first stage and 15 thousand pounds per inch for the second stage. The prop was 12 times stiffer in the first stage than in the second. According to the first criterion, this kind of mechanical properties of a support is ideal.

The maximum load was 165,000 pounds and the maximum deformation was about 7.6 inches. Note that those values can not be considered final since the load showed a trend of continuing increase. The reason for stopping the test was the limitations of the testing machine.



Figure 4.21. Wedge prop 2 after failure.
(Premature failure)



Figure 4.22. The head of wedge prop 3.
(Sawcut too wide)

Wedge prop 4

The load-deformation curve for this prop (figure 4.18) can be included in the first category. The pod yielded at 130,000 pounds. There was no sign of load drop after the yielding of the pod. This indicates that the top band was tightened perfectly. The first load drop corresponded to the breakage of the top band. The load recovered after slightly decreasing and continues to increase as the prop deformed. The stiffnesses of the prop were 135 thousand pounds per inch in the first stage and 10.5 thousand pounds per inch in the second stage. The ratio between the two was 12.8 which is very close to the value in test 3. The maximum load was 183,000 pounds and the maximum deformation was 7.25 inches. Those values can also not be regarded final for the same reason as mentioned for wedge prop 3.

Wedge prop 5

The load-deformation curve (figure 4.19) for this prop is thought to be a typical curve in the second category. The pod yielded at 90,000 pounds. The stiffness of the prop in the first stage was 195 thousand pounds per inch. The prop experienced its first load drop upon the yielding of the pod. The second load drop corresponded to the breakage of the top band. However the load drop were not severe, and after each drop the load recovered to the original value or to a value slightly higher. Generally speaking, the load was constant with some fluctuation as the prop deformed. Statistically, the average load in the second

stage was 85,000 pounds and the standard deviation was 8,700 pounds which was relatively small. The small deviation means that the load was stable. The maximum load in the second stage was 98,000 pounds and the minimum was 71,000 pounds. The total deformation of the prop was 13.4 inches which was the largest recorded among the six props. The prop finally failed in a splitting mode, indicating that the third band was not tight enough.

Wedge prop 6

The load-deformation curve (figure 4.20) of this prop actually has three stages. The first stage is the period prior to the yielding of the pod. The second occurs before the buckling of the prop and after the yielding of the pod, and the third after the buckling of the prop. Since the third stage is a failing period of the prop, the load-deformation curve has, practically, only two effective stages. Hence this curve is classified into the first category.

The pod yielded at 115,000 pounds. The load dropped sharply after the yielding of the pod. This may be attributed to the substantial height above the first band which was the largest among the six props. The load continued increasing after recovering from the drop until it failed in a buckling mode.

The stiffnesses of the prop were 305 thousand pounds per inch for the first stage and 12 thousand pounds per inch for the second stage. The maximum load was 154,000 pounds and the effective deformation was about 7 inches.

4.3.5 Summary and Recommendation

The preliminary testing of the wedge prop shows that it has very good load-deformation characteristics. Generally the load-deformation curves can be divided into two stages. Depending on the relationship between the load and the deformation in the second stage, the curves can be classified into two categories. In the first category, load increases as the prop deforms, and in the second, load does not change as the deformation increases.

For the six tests, the stiffnesses of the wedge props in the first stage were from 85 to 305 thousand pounds per inch. For the three props in the first category, the stiffnesses in the second stage were 10.5, 12, and 15 thousand pounds per inch respectively. For the two props in the second category, the average loads in the second stage were 87,000 and 85,000 pounds, and the standard deviations were 16,000 and 8,700 pounds respectively. The maximum loads for the props tested were between 95,000 and 186,000 pounds. The maximum deformations ranged from 7 to 13.4 inches, except for prop 2 which buckled prematurely.

The maximum load is affected by the wood species. Among the six props made of three different species of wood, hickory wedge props (No.3 and No.4) bore the largest maximum loads, and locust wedge props (No.5 and No.6) had the largest stiffnesses in the first stage. Factors such as the distance between the bands, the depth of the sawcut, the tightness of the bands and the strength of the bands material, all contribute to the mechanical properties of the wedge props.

From the theoretical point of view, the relationship between the stress in the wood log and that in the band can be established when the wedge prop is subject to uniaxial load. The relationship can be used to determine the possible failure modes of the wedge prop.

Based on the preliminary testing, some recommendations can be made. For example, the bands should be tight enough to close the sawcut, but without putting too much contact pressure between the pod and wedges. The height above the first band should not be too large, preferably between 2.5 to 3 inches. The proper value for the distance between the first and the second band may range from 3.5 to 4.5 inches, and that for the distance between the second and third band may vary from 5.5 to 6.5 inches. To prevent the splitting of the wood log, the third band ought to be tighter than the first two.

Since the props tested were shorter than normal posts, and the testing procedure was multi-stroked, the test results may deviate from what would be observed in actual underground conditions. In future testing, these shortcomings need to be corrected.

The Micon Yield Capsule, Super Post and Wedge Prop are all yieldable supports, but in some cases, their strengths may not be high enough to deal with specific ground control problem. Thus, supports with a higher material strength are needed. Concrete supports fall into this category, and will be discussed in the following chapter.

CHAPTER 5 CONCRETE SUPPORTS

As a material, concrete is designed mainly to withstand compressive stress. However, by including steel fiber or other materials and forming a new material known as reinforced concrete, tensile strength requirements can be met. Compared to wood and steel, concrete possesses several advantages as a supporting material:

1. It has a high compressive strength and the cost is low.
2. It is the safest material with respect to fire resistance.
3. It is resistant to rust and decay, and is least affected by atmospheric conditions.

However the plain concrete support has some disadvantages. First, without reinforcement, concrete has very low tensile strength. Second, it breaks suddenly without any warning and the yieldability is very poor. Another disadvantage is that broken concrete has no value and it can not be reused. In order to make up the deficiencies of plain concrete, various methods have been tried. To meet the tensile strength requirements, the steel fiber reinforced concrete crib was invented, and to meet the deformation requirements, the sandwich crib was developed. All these supports are discussed in this chapter.

5.1 Plain Concrete Supports

Since the load limit of some wood cribs may easily be exceeded by roof pressures in certain areas of mines, concrete blocks have been stacked to replace the timber pieces. Although the plain concrete crib

is cheaper in material costs and can bear a much higher load than a timber crib, it fails suddenly and violently when its strength is exceeded. In this section the mechanical properties of the concrete are discussed and various factors affecting the performance of the plain concrete are considered.

Plain concrete consists of coarse and fine aggregate, cement, and water. The materials are mixed together until a cement paste is developed, filling most of the voids in the aggregates and producing a uniform, dense concrete. The plastic concrete is then placed in a mold and left to set, harden, and develop adequate strength (Hassoun, 1985). Therefore, concretes are multiphase materials. Two-phase models of mechanical behavior are acceptable approximations, however, as long as the dimensional level at which the behavior is being considered is large compared with the maximum particle size in the matrix. Thus certain phases are assumed homogeneous and isotropic. For example, concrete may be treated as a two-phase composite of aggregate and cement mortar, mortar as a two-phase composite of sand and cement paste, paste as a two-phase composite of gel and gel pores, etc. Thus, at their respective dimensional levels, concretes, mortars, and cement pastes can all be considered as two-phase materials having a 0.3-0.6 volume fraction of coarse particles, roughly spherical in shape, embedded in a somewhat homogeneous matrix. In each case statistical homogeneity and isotropy for the two phases under consideration are assumed (Nicholls, 1976).

Based on the two-phase assumption, the Young's modulus of plain concrete can be expressed as

$$E = \frac{E_c E_d}{v_c E_d + v_d E_c} \quad (E_d > E_c) \quad (5.1)$$

where v_c = the volume fraction of the cement mortar,

v_d = the volume fraction of the aggregate,

E_c = the Young's modulus of the cement mortar,

E_d = the Young's modulus of the aggregate.

Generally, the Young's modulus of the concrete is high and its Poisson ratio is low. Thus, when loaded, concrete usually does not deform much before its ultimate strength is exceeded. Figure 5.1 shows the load-deformation curve of a plain concrete crib.

Concrete subjected to any stress state can support loads up to 40-60 percent of ultimate without apparent distress. Above this level, noises signifying internal disruption can be heard until, at about 70-90 percent of ultimate, small cracks appear on the surface. The cracks spread and interconnect until, at the ultimate load, specimens typically fracture into many pieces (Nicholls, 1976).

Several stages of cracking can be distinguished and they are:

1. Crack initiation. Under initial loading, microscopic cracks appear at points of high tensile strain concentration.

2. Stable crack propagation. As the load is increased, cracks propagate, but if the stress level is maintained as a constant, crack propagation ceases.

3. Unstable crack propagation. Cracks become self-propagating under constant applied load, and failure occurs whether or not the load increases. This stage occurs at 70-90 percent of ultimate stress and is accompanied by a dilation of the structure.

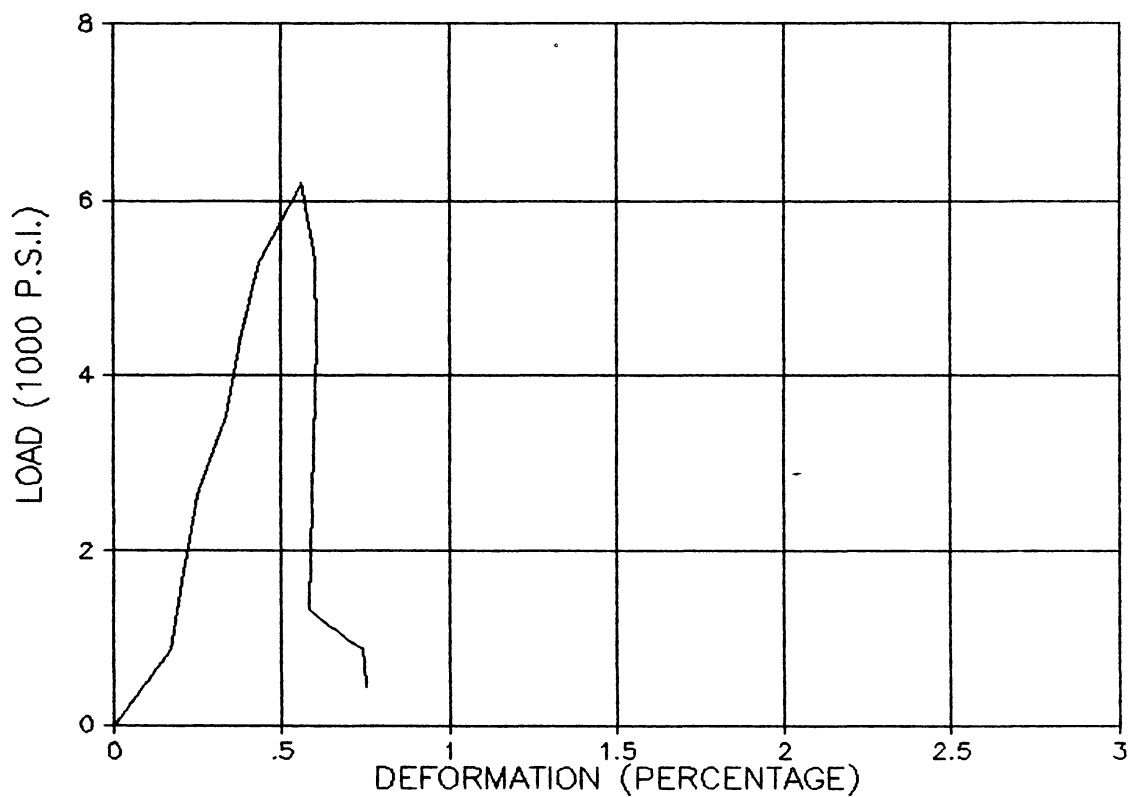


Figure 5.1. Load-deformation curve of a plain concrete crib.
(Anderson, 1980)

The crack patterns which develop under a specific load depend principally on (1) the state of the applied load and (2) the relative elastic moduli and Poisson ratios of the continuous and discrete phases. The stress state influences the overall crack pattern, and the relative moduli and Poisson ratios influence the geometry of crack development in the vicinity of individual aggregates.

Typically, cracks develop normal to the plane of maximum tensile stress. They may occur:

1. At the aggregate-paste interface.
2. In the cement paste.
3. In the aggregate particles.

The strength of concrete depends upon many factors and may vary within wide limits with the same production method. The main factors that affect the strength of plain concrete are discussed below (Hassoun, 1985).

Water-Cement Ratio

The water-cement ratio is the most important factor affecting the strength of concrete. For complete hydration of a given amount of cement, a water-cement ratio (by weight) equal to 0.25 is needed. A water-cement ratio more than 0.1 higher is needed for the concrete to be reasonably workable. This means that a water-cement ratio of more than 0.35 must be chosen. This ratio corresponds to 4 gallons of water per sack of cement (94 lbs). Good workability is attained when the ratio exceeds 0.5. The relationship between water-cement ratio and compressive

strength of normal weight concrete is shown in figure 5.2. Many formulas are available for expressing compressive strength in terms of water-cement ratio. According to Abrams (Biron, 1983)

$$\sigma_b = \frac{A}{B^\alpha}. \quad (5.2)$$

According to Bolomey (Biron, 1983),

$$\sigma_b = K \left(\frac{1}{\alpha} - 0.5 \right). \quad (5.3)$$

According to Graf (Biron, 1983)

$$\sigma_b = \frac{K_n}{c\alpha^2} \quad (5.4)$$

where σ_b = compressive strength,

α = water-cement ratio,

A = coefficient for 28 days of curing, 950,

B = coefficient for 28 days of curing, 9,

K = coefficient for 28 days of curing, 180, and for 7 days of curing, 150,

K_n = compressive strength of cement,

c = coefficient of workmanship, good: 4; medium: 6; poor:8.

The properties and proportion of concrete constituents

The ratio of cement to aggregate, grading, surface texture, shape, strength, and stiffness of aggregate particles, and maximum size of aggregate all affect the strength of the concrete. Other factors partially or totally independent of water-cement ratio, which influence

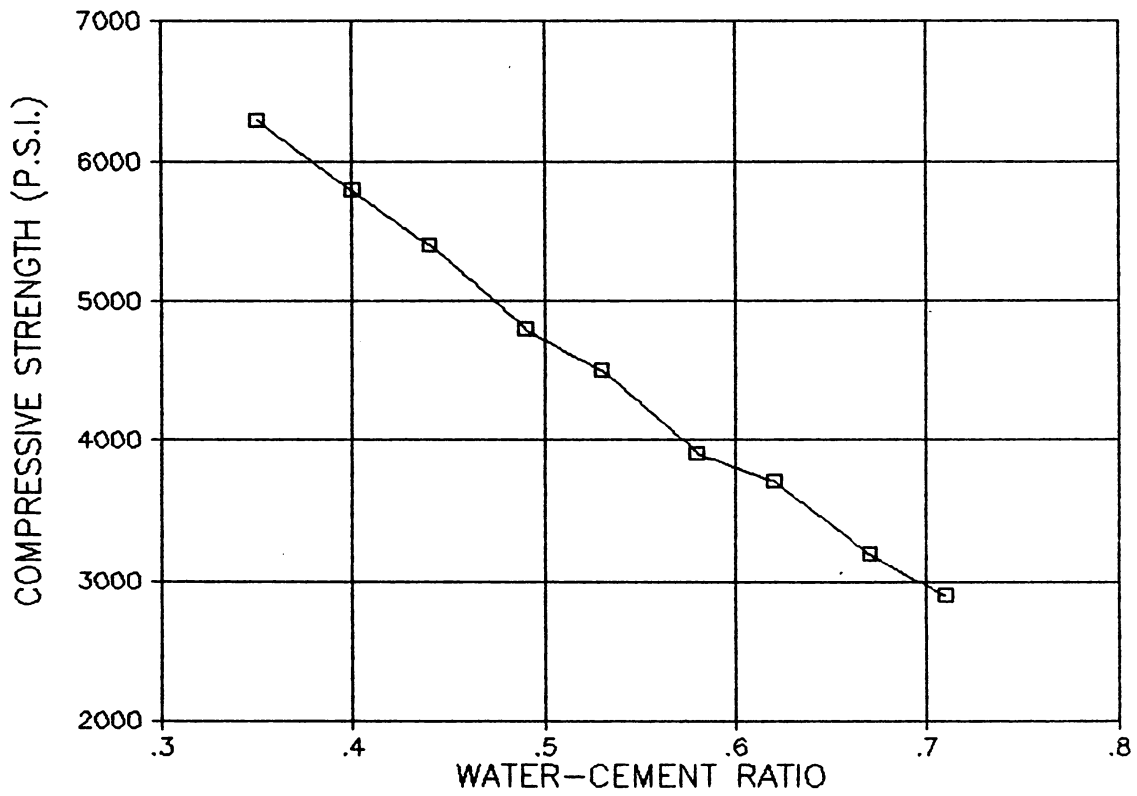


Figure 5.2. Relationship between water-cement ratio and compressive strength of the concrete. (Hassoun, 1985)

the strength of the concrete, are (1) type and brand of cement, (2) amount and type of admixture and (3) mineralogic makeup of aggregate.

The method of mixing, placing, and degree of compaction

The use of mechanical concrete mixers and the proper amount of mixing time both have favorable effects on the strength of concrete. Also, the use of vibrators produces dense concrete with a minimum percentage of voids. A void ratio of 5 percent may reduce concrete strength about 30 percent. Feret gave the following relationship between compressive strength and the compaction of concrete (Biron, 1983):

$$\sigma_b = K \left(\frac{V_c}{1-C+V_c} \right)^2 \quad (5.5)$$

where σ_b = compressive strength of concrete after a known curing time,
K = coefficient, changing according to curing time and granulometry of aggregates,
 V_c = volume of cement in 1 unit volume of concrete,
C = compaction of concrete.

Curing condition and the age of concrete

The curing conditions exercise an important influence on the strength of concrete. Both moisture and temperature have a direct effect on the hydration of cement. The longer the period of moisture storage, the greater the strength. Figure 5.3 shows the age-compressive strength

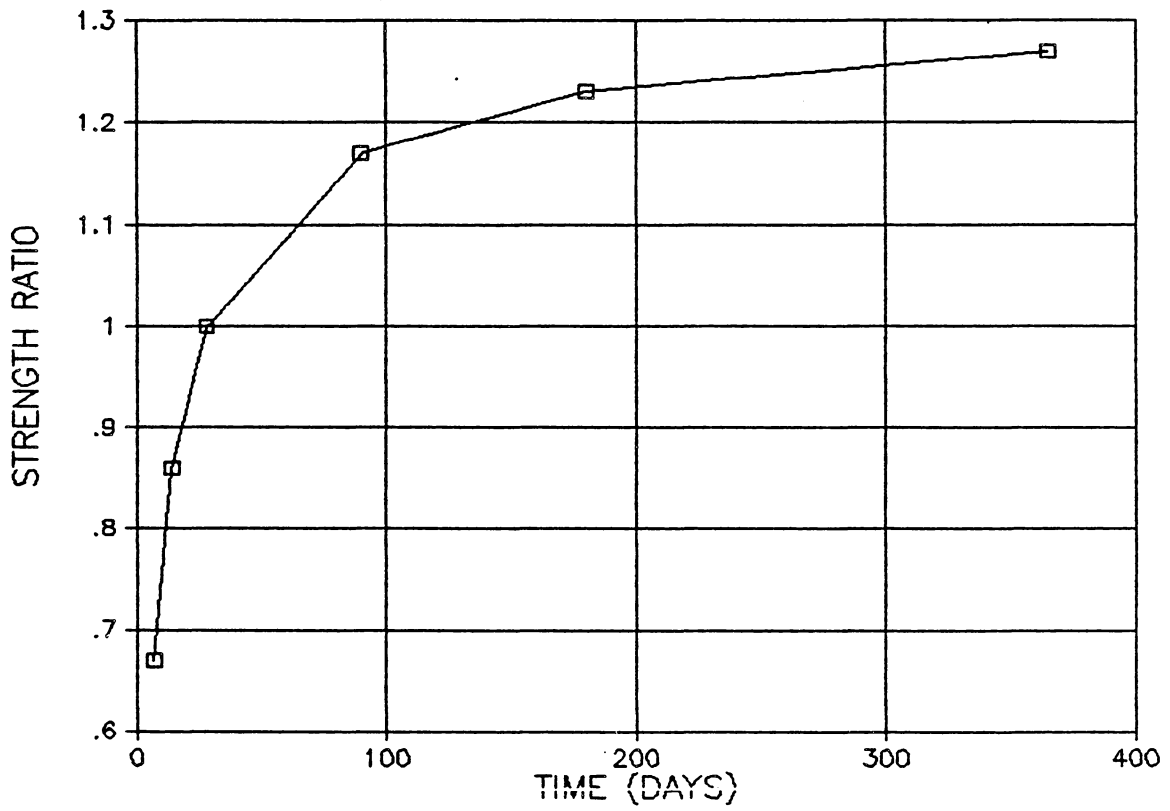


Figure 5.3. Relationship between the age and the strength of concrete. (Hassoun, 1985)

relationship.

Higher early strengths may be achieved through use of High-Early-Strength cement. Principal advantages occur prior to 7 days. At a 40°F curing temperature, the early advantages of this type of mixture are more pronounced and persist longer than at higher temperatures.

Figure 5.4 shows the effect of high concrete curing temperatures on compressive strength. These tests, using identical concretes of the same water-cement ratio, showed that while higher curing temperatures increase early strength, at later ages the reverse is true. If the water content had been increased to maintain the same slump (without changing the cement content), the reduction in strength would have been even greater (Fintel, 1985).

Strength gain practically stops when moisture required for curing is no longer available. Concrete that is placed at lower temperatures (but above freezing) may develop higher strengths than concrete placed at high temperatures, but curing must be continued for a longer period. It is not safe to expose concrete to freezing temperatures at early periods. If freezing is permitted within 24 hours, a much lower strength will result.

Loading conditions

The compressive strength of concrete is estimated by testing a cylinder or cube to failure in a few minutes. When situated under sustained loads for years, the ultimate strength of concrete is reduced

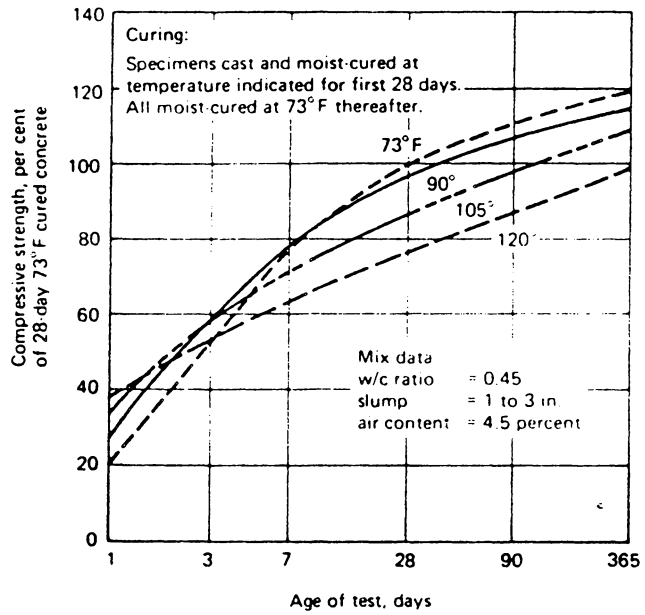


Figure 5.4. Effect of high temperature on compressive strength at various ages. (Fintel, 1985)

by 30 percent. Under 1-day sustained loading , concrete may lose approximately 10 percent of its compressive strength. Sustained loads, as well as dynamic and impact effects, should be considered in the design of concrete supports.

Plain concrete supports in mines take many forms. Shotcrete, concrete cribs, and concrete gallery sets are some of the common ones. Concrete is also used in shafting lining, gallery lining, and for artificial roofs. In some applications, it is subjected to compression, and in others it is subjected to tension. If concretes are used under tension, it is advantageous to reinforce them, since the tensile strength of the plain concrete is very low.

5.2 Steel Fiber Reinforced Concrete Supports

The addition of steel fibers to concrete can solve the problem of brittle failure and increase the tensile strength of the concrete block.

Steel fibers have a Young's modulus 10 times as that of concrete, have a reasonably good bond, and have high elongation at fracture. With about 4 percent fibers by volume, flexural strength can be doubled and compressive strength can also be increased (Nicholls, 1976).

The micro steel wires used in radial belted tires are available in diameters as low as 0.003 inch and have strengths as high as 500,000 psi. However, the wire cost increases significantly for finer diameters, and it is probable that fine steel wire having a high carbon content may not survive corrosion in the cement paste.

A major limitation in the use of steel fibers is segregation and

balling during mixing, even with wire lengths considerably below the critical length. Balling is related to three factors: the aspect ratio, the volume percentage of fibers, and their rigidity (rigid fibers are more trouble than flexible ones). Typically, to reduce balling and segregation during mixing to a level within the tolerable limits, steel fibers significantly shorter than the critical length must be used, giving low fiber tensile efficiency. As tensile reinforcement, improvement by fibers is therefore inferior to improvement by the same volume of conventional reinforcing rods, because fibers are (1) more easily pulled out, (2) randomly oriented, and (3) dispersed throughout the cross section of the block.

Characteristically a plain mortar with a slump of 7 in. will have a slump of only 1 in. with 2.5 percent by volume of fibers having an aspect ratio of 90. Mixing is very difficult with fibers having aspect ratios greater than 100 or fiber volumes larger than 4 percent. Mixing problems are generally increased, and improvements due to fiber addition decrease with increasing aggregate size (Nicholls, 1976).

Little is known about the bond mechanisms between cements and steel fibers. The limited amount of steel-fiber-reinforced concrete research to date has nearly all been experimental. Thus, even an approximate treatment of the problem in terms of classical mechanics may be useful in determining which factors are important in the strength of the steel-fiber-reinforced concrete. In order to perform the analysis, the following material property assumptions will be made (Nicholls, 1976):

1. Cement mortar undergoes brittle failure.
2. Steel fiber undergoes either brittle or ductile failure.

3. Tensile failure strain is lower for mortar than for the steel fiber.

4. The limiting bond stress between mortar and fiber is the interfacial shear strength, rather than the shear strength within either the mortar or the steel fiber.

If interfacial shear strength, τ , is assumed to obey the Coulomb equation, then

$$\tau = c + n \tan\phi \quad (5.6)$$

where c is the static cohesion between steel fiber and mortar, n is the interfacial radial pressure, and ϕ is the friction angle. The radial pressure can be caused, for example, by the curing shrinkage of the cement paste. The fiber tensile stress in the vicinity of a mortar crack is then,

$$\begin{aligned} \sigma_x &= \sigma_{x0} - \frac{2}{r} \int_0^x \tau_x dx \\ &= \sigma_{x0} - \frac{2}{r} \int_0^x (c + n_x \tan\phi) dx \end{aligned} \quad (5.7)$$

where σ_{x0} is the fiber tensile stress at the mortar crack, x is the distance along the fiber away from the crack, and c is a constant, but is equal to zero where fiber necking (or tapering) is sufficient to eliminate contact between the fiber and its cavity. The radial pressure is

$$n_x = n_{x0} - \sigma_x \mu \quad (5.8)$$

where n_{x0} is the radial pressure when $\sigma_x = 0$, and μ is the fiber Poisson ratio, assumed to remain constant throughout both elastic and plastic

deformation of the fiber. Substituting equation 5.8 into equation 5.7,

$$\sigma_x = \sigma_{x0} - \frac{2x(c + n_{x0} \tan\phi)}{r} + \frac{2\mu \tan\phi}{r} \int_0^x \sigma_x dx, \quad \sigma_x \geq 0. \quad (5.9)$$

This is an integral equation of the Volterra type, that is, the wanted function appears under the integral sign. Solving the equation,

$$\sigma_x = \sigma_{x0} + \frac{c + n_{x0} \tan\phi}{\mu \tan\phi} (e^{-2x\mu \tan\phi/r} - 1), \quad \sigma_x \geq 0. \quad (5.10)$$

The fiber critical length, l_c (neglecting the crack width), can be obtained by setting $\sigma_{x0} = \sigma_f$, the fiber tensile strength, and solving for the value of x ($= l_c/2$), which makes $\sigma_x = 0$ in equation 5.10:

$$l_c = \frac{r}{\mu \tan\phi} \ln\left(\frac{\sigma_f \mu \tan\phi}{c + n_{x0} + \tan\phi}\right). \quad (5.11)$$

Equation 5.11 represents a lower bound critical length, or a critical length in the case of only a single mortar crack at the fiber midpoint. For cases of more extensive cracking the critical length is greater.

The steel fiber reinforcement primarily improves the postcracking characteristics of the concrete. The stress-strain behavior in steel-fiber-reinforced concrete may be divided into two regions: (1) below the strain level at which the mortar begins to crack and (2) above this level.

In region 1, both steel fiber and mortar are assumed to behave elastically, and the simple mixture law is applied. The lower bound of the Young's modulus of the steel-fiber-reinforced concrete is:

$$E_c = E_f v_f + E_m v_m \quad (5.12)$$

where E_f = the Young's modulus of the steel fiber,

E_m = the Young's modulus of the cement mortar,

v_f = the volume fraction of the steel fibers,

v_m = the volume fraction of cement mortar.

In region 2, the cement mortar progressively cracks until, at the limit, the entire tensile load may be carried by the fibers. For this limiting condition,

$$E_c = \frac{d\sigma_f}{d\varepsilon_f} v_f \quad (5.13)$$

where $d\sigma_f/d\varepsilon_f$ is the stress-strain curve slope of the fibers, whether deforming elastically or plastically. Equations 5.12 and 5.13 indicate the lower and upper bound limits of the deformation behavior for the region of mortar cracking, where the mortar contribution decreases with increasing strain, in the manner of a brittle coating on a fiber which undergoes progressive cracking as the fiber is stretched. In region 2, the behavior of steel-fiber-reinforced concrete is quasi-elastic due to progressive mortar cracking. These two regions of stress state exist simultaneously in adjacent micro-areas of the composite; i.e., quasi-elastic where the mortar is cracked and the fibers are in a local state of pull out and elastic at locations between cracks.

Steel-fiber-reinforced concrete can fail in the following modes:

1. Cement mortar fails; fibers then fail in tension or bond at a lower stress level.

2. Cement mortar fails; fibers then fail in tension at a higher stress level.

3. Cement mortar fails; fibers then fail in bond at a higher stress level (Nicholls, 1976).

The U. S. Bureau of Mines conducted some tests on steel-fiber-reinforced concrete cribs (Anderson, 1980). The mix design that they used is shown in Table 5.1. The crib configuration and the dimensions of the crib members are shown in Table 5.2. The full-scale cribs were tested on a hydraulic 5 million-pound-capacity testing machine located at the Bureau of Reclamation in Denver, Colorado. The deformation rate was maintained at about 0.1 inch per minute. The typical load-deformation curves of steel-fiber-reinforced concrete from each configuration are shown in figure 5.5. In comparing figure 5.1 with figure 5.5, it can be seen that the post-failure characteristics of the concrete crib are improved dramatically by the reinforcement of the steel fibers. This is an important advantage of the steel-fiber-reinforced concrete.

The use of steel-fiber-reinforced concrete blocks to build cribs is based on the same principle as the use of wood. That is, longitudinal, rectangular blocks are stacked in layers in a crisscross manner. The blocks are positioned at right angles to the blocks of the layer below. With this arrangement, the possibility of misalignment exists when the concrete blocks at the base are not placed exactly parallel or when the blocks at the base are subject to unequal settlement. Such misalignments may create localized, high stress areas which reduce the load capacity of the cribs.

Recognizing the problem of misalignment, the Underground Supports Division of Commercial Shearing, Inc., conceived a circular,

Table 5.1 SFRC Crib Member Mix Design (Anderson, 1980)

Material	Quantity per yd ³
Cement (Type III)	470 lb. (5 bag)
Water	221 lb.
Sand	1,500 lb.
3/8 gravel	1,700 lb.
Wire fiber	80 lb. (bend-end, 0.02 x 1.97 in)
Air entrainment solution	3/4 oz per bag cement
Accelerator	1 to 4 qt. (varied for form-reuse sequence.)

Table 5.2 Dimension of the SFRC Cribs Tested (Anderson, 1980)

Crib configuration	Cross-section area (in. ²)	Actual height (in.)	Crib member dimension (W x H x L)
10 by 30	300	73	10 by 3 by 30
20 by 20	400	73	10 by 3 by 20
* 30 by 30	800	73	10 by 3 by 30
* 30 by 30	800	73	10 by 3 by 10

* Assembled crib contained a 10 by 10 in. hollow core.

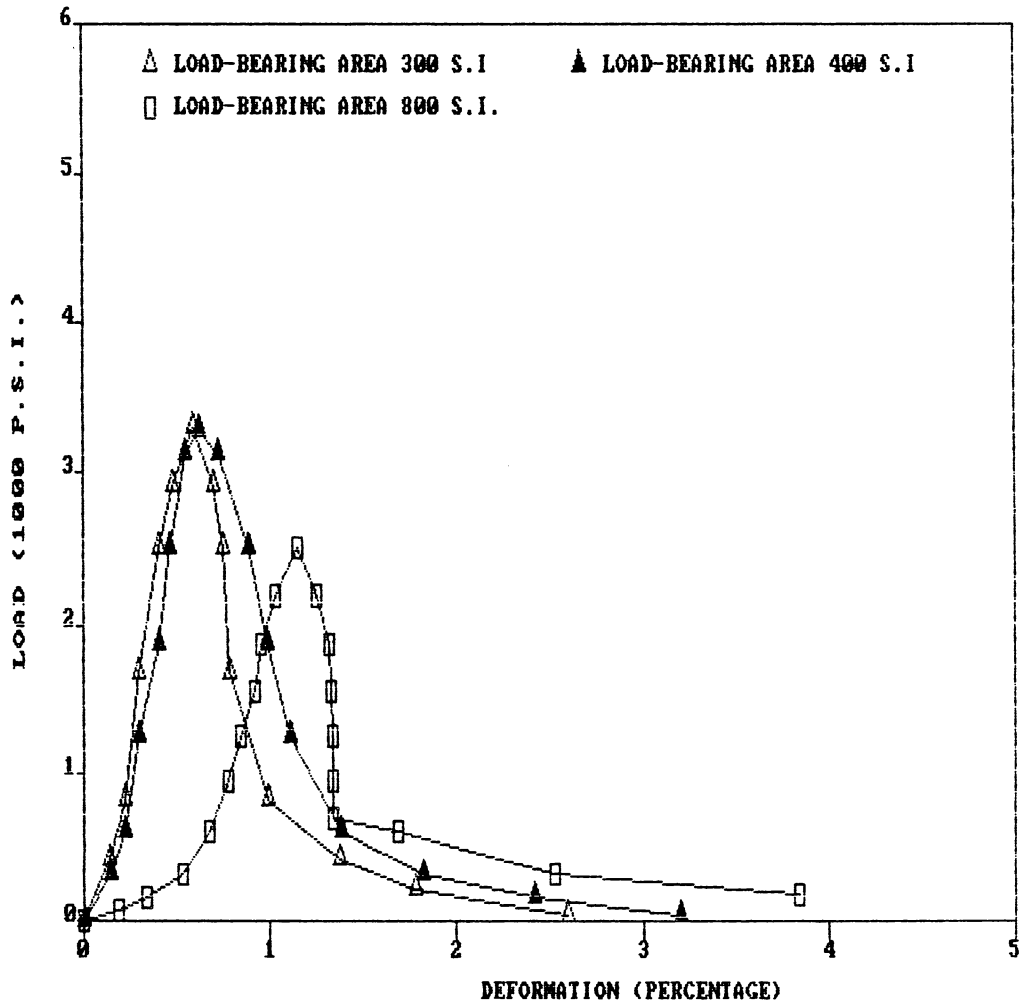


Figure 5.5. Load-deformation curve of steel-fiber-reinforced-concrete crib. (Anderson, 1980)

one-piece-per-layer, steel-fiber-reinforced concrete cribbing which is being marketed under the name "Donut Cribs" (Chlumecky, 1986). The manufacture claims that Donut Cribs eliminate the possibility of misalignment and provide 100 percent bearing between layers of stacked cribs. Figure 5.6 shows some Donut Crib pieces.

Tests on the steel-fiber-reinforced concrete block cribs and Donut Cribs were conducted in a 1.2 million pound capacity Tinius Olson machine at Pittsburgh Testing Laboratories (Chlumecky, 1986). A load-deformation curve from each type of crib is shown in figure 5.7. It seems from figure 5.7 that both the load capacity and the deformation of the Donut Crib are superior to those of the block crib. However, the results may be biased since there are open spaces between the layers of the block crib. If the block crib were solid-walled, the results would probably not be much different. Nevertheless, Donut Cribs still have two advantages that block cribs can not match:

1. 40 percent fewer pieces are needed for the construction of Donut Cribs than for that of block cribs. This is a major advantage where material handling is a significant cost factor, such as in deep shaft mines.

2. The round cross section of Donut Cribs has less resistance to ventilating air flow.

In comparison with block cribs, Donut Cribs also have some disadvantages. They are less flexible than block cribs. Thus when the floor is not level, bending moments will result due to the vertical load, and the loading capacity of the crib will be reduced. Another problem is that, other things being equal, the critical buckling load of the

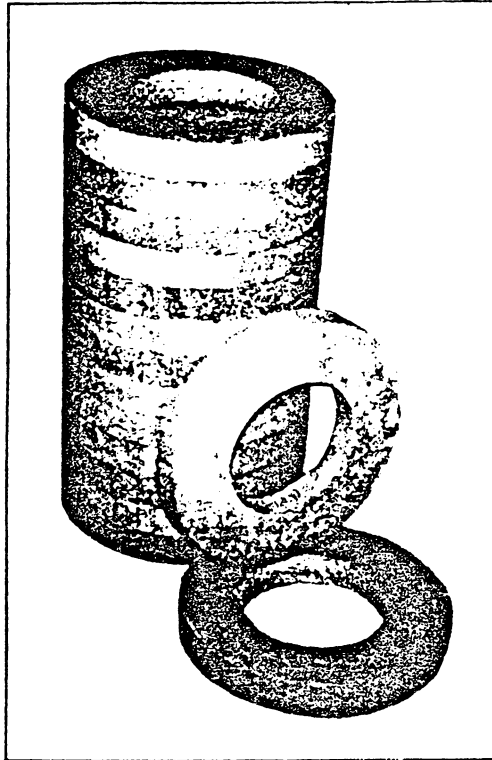


Figure 5.6. Donut Crib. (Chlumecky, 1986)

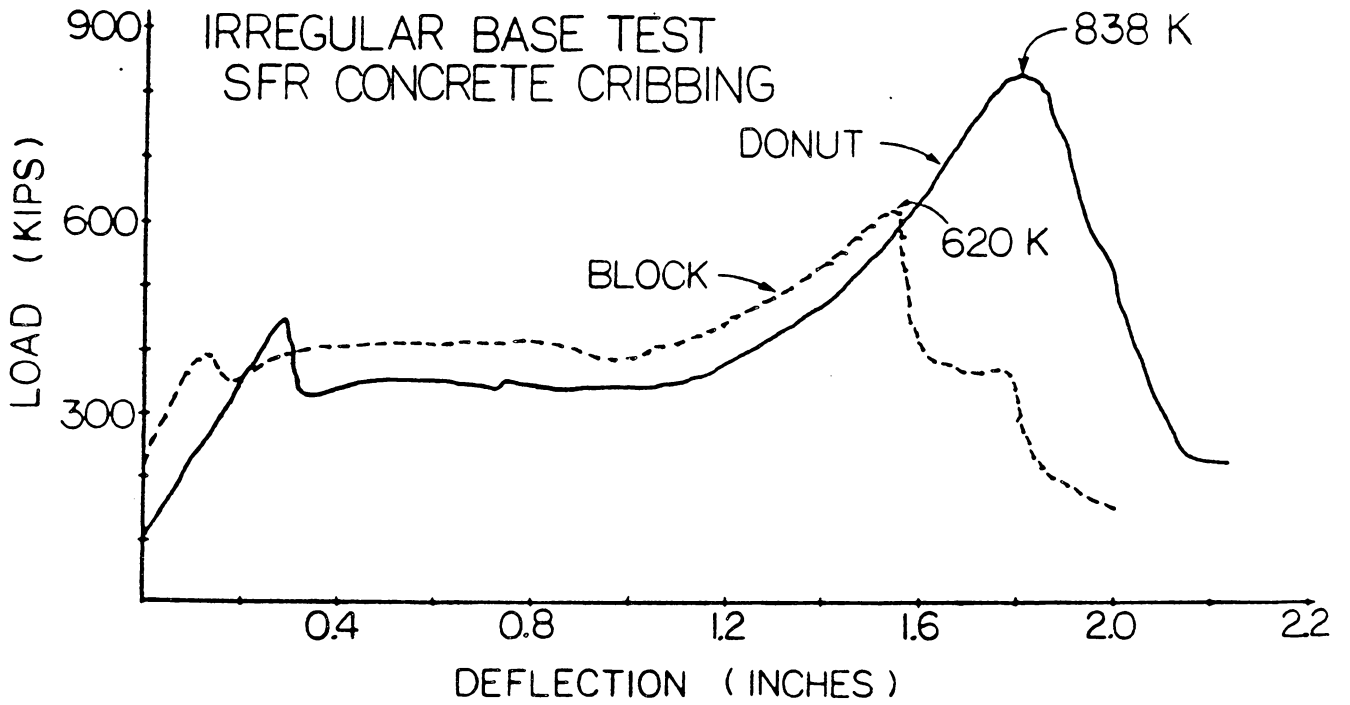


Figure 5.7. Comparison between the load-deformation curve of Donut Crib and that of the steel-fiber-reinforced-concrete block crib. (Chlumecky, 1986)

circular crib is less than that of the square crib, although the difference may not be significant.

The fibers in the steel-fiber-reinforced concrete help to improve the mechanical properties of the concrete, but they may also pose handling problems since protruding fibers are hazardous. This is the only disadvantage of the steel-fiber-reinforced concrete over the plain concrete.

5.3 Sandwich Cribs

Although the post-failure characteristics of steel-fiber-reinforced concrete cribs are much better than those of plain concrete, steel-fiber-reinforced concrete cribs still have very poor yieldability. They fail at a deformation much lower than that of wooden cribs when subjected to compression, but at a load several times higher than that of wooden cribs. In order to have a crib more yieldable and, at the same time maintaining a higher resistance, concrete blocks and wood or other yieldable materials have been combined to form another type of crib, the sandwich crib. The sandwich crib incorporates the properties of concrete and wood in a more complicated pack.

A sandwich crib is constructed in such a way that the concrete and wood layers overlap, one on top of another, as shown in figure 5.8. The sandwich crib as a whole can be treated as two-phase composite of concrete and wood. The Young's modulus of the crib can be calculated by:

$$E = \frac{E_c E_w}{v_c E_w + v_w E_c} \quad (5.14)$$



Figure 5.8. Sandwich crib.

where v_c = the volume fraction of concrete,

v_w = the volume fraction of wood,

E_c = the Young's modulus of concrete,

E_w = the Young's modulus of wood.

It is obvious from equation 5.14 that, as the wooden portion of the crib increases, the crib will become more yieldable. Thus the yieldability of the crib can be controlled by adjusting the volumes of the components.

The use of sandwich cribs can be traced back to the 1960's. During the latter half of 1965, a timber shortage was experienced in a South Africa gold mining company. It was decided that a substitute for some of the timber should be sought in order to allow for building up the stock to a safer level and to minimize the effect of any further reduction in timber supply (Petersen, 1966). Concrete was selected as a possible substitute because of the availability of sand, stone, and cement. It was realized that a complete concrete support may disintegrate under normal pressure in the stopes, but it was felt that the replacement of a portion of the timber in a crib would stiffen the support and still allow the remaining timber to absorb the closure of the hanging wall and footwall. In an effort to establish the feasibility of using concrete interlaced with timber as a form of underground support, tests were performed. From the tests, it was concluded that:

1. A crib composed of alternating layers of timber and concrete was feasible.

2. The concrete blocks introduced a stability lacking in the purely timber crib.

3. The addition of concrete blocks into the timber cribs increased the rigidity of the crib.

In 1978, Ortlepp published a paper discussing the essential engineering principles that determine the behavior of sandwich cribs. In his paper, Ortlepp listed various factors affecting the behavior of the sandwich crib. Following are some of the factors:

1. The strength of the concrete blocks. Figure 5.9 shows the load-deformation curve of the sandwich cribs with different concrete strengths. From figure 5.9, it can be seen that the strength of the concrete block has a relatively small effect on overall crib characteristics.

2. Shape of the concrete blocks. A convenient way to improve crib stiffness by increasing the concrete component is to increase the height of the concrete block. However, because of the greater free surface available between the reinforcing timber layers, the concrete spalls and fails earlier and at considerably lower loads. This effect is displayed in figure 5.10 for blocks 125 mm (4.92 inches) high (curve 1) and blocks 100 mm (3.94 inches) high (curve 2).

3. Uniformity and surface finish. To avoid point-loading, which can cause premature fracturing of the concrete, the concrete blocks must be perfectly regular prisms with loaded faces, in particular, plane and parallel. Projecting pieces of large aggregate in the concrete can weaken the timber by penetrating and cutting the fibers. Crushed stone of 10 (0.39 inch) to 12 mm (0.47 inch) maximum size, when used in a suitable blockmaking machine, provides a sufficiently smooth surface finish and regularity of shape.

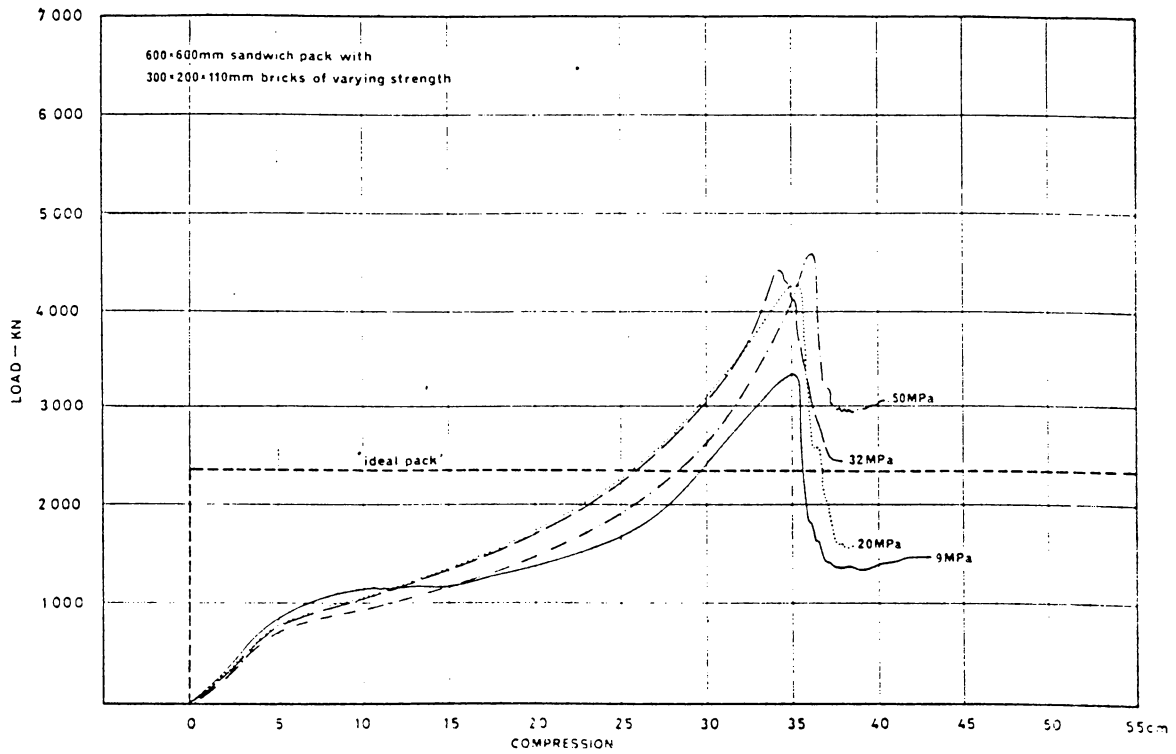


Figure 5.9 The effect of concrete strength on sandwich crib characteristics. (Ortlepp, 1978)

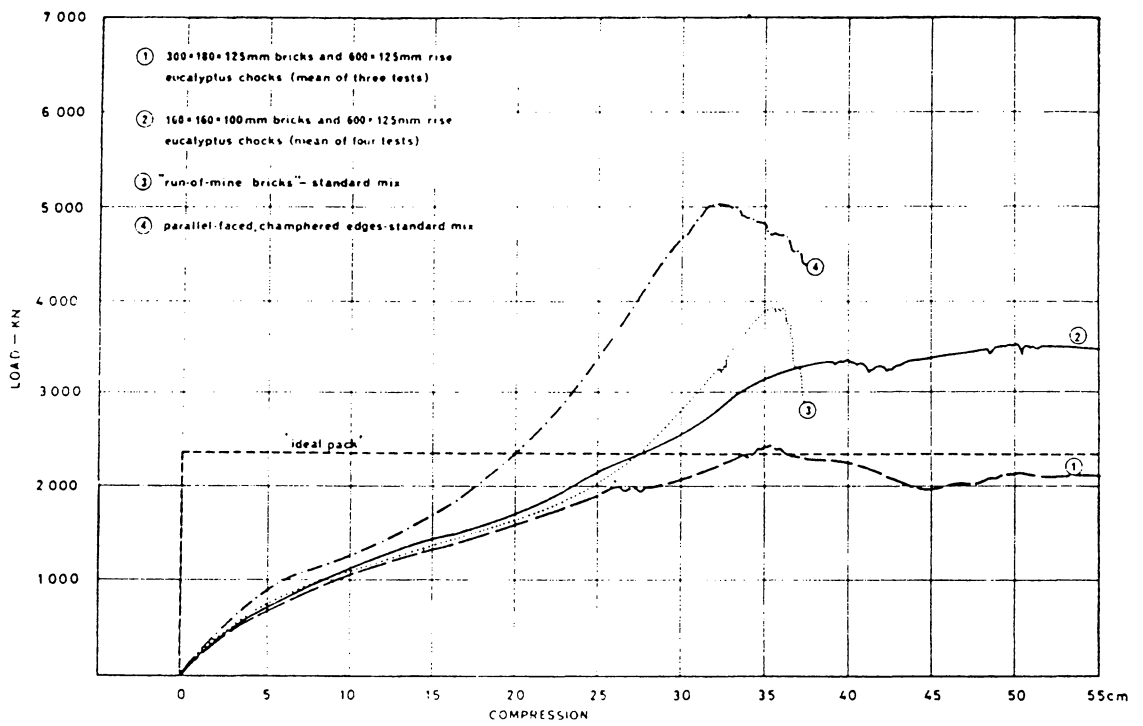


Figure 5.10. The effect of the block height and surface finish on sandwich crib characteristics. (Ortlepp, 1978)

4. The species of timber. Figure 5.11 shows the load-deformation curves of sandwich cribs constructed with planks of various timber species. It can be noticed from figure 5.11 that timber species have a profound effect on the overall performance of sandwich cribs. Timber species is perhaps the most important factor affecting the load-deformation characteristics of sandwich cribs.

5. The size of the timber members. The stiffness of the sandwich crib is increased by decreasing the vertical height of the timber, as indicated by equation 5.14.

6. Tensile strength (perpendicular to grain) of the timber. Careful observation of a destructive test of a sandwich crib reveals that the function of the timber is not only to accommodate entry convergence by yielding but also, equally importantly, to provide transverse reinforcement to the crib. Because of its very anisotropic nature, the timber has a somewhat ambivalent effect in this regard. As it crushes during the yielding phase, the timber spreads at right angles to its fiber direction - an exaggerated Poisson effect. This actually promotes initial failure of concrete by pulling the block apart and causing the characteristic vertical split. Later, when large concrete fragments expanded laterally, the very high tensile strength and modulus of the timber bind the crib together and prevent the pieces from abjectly slumping into the angle of repose. The overriding importance of this effect can be dramatically illustrated when the sandwich crib being tested has the fibers in its successive layers pointing in the same direction.

7. Creep of the timber. The liability of the sandwich crib to

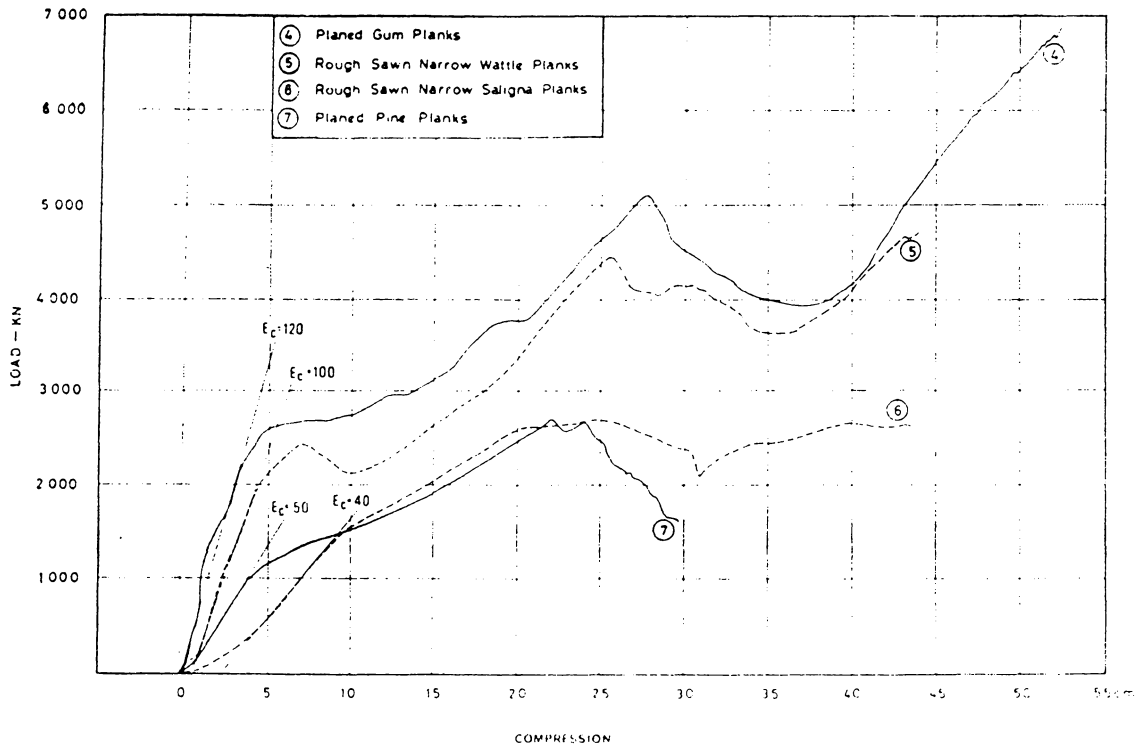


Figure 5.11. The effect of timber species on sandwich crib characteristics. (Ortlepp, 1978)

creep is decreased by decreasing the vertical content of timber and by increasing its area.

When designing a sandwich crib, all of the above factors should be kept in mind.

In addition to wood, other yieldable materials can also be used in the construction of sandwich cribs. One type of sandwich crib, used in a Pennsylvania coal mine, consists of concrete blocks and particle board. A test was conducted to determine the load-deformation characteristics of this type of crib. The test was performed on a one million pound loading frame. The test specimens were randomly selected from the coal mine. The size of the concrete blocks used in the test was 6 x 8 x 16 inches and that of the particle board was 0.25 x 8 x 16 inches. The concrete blocks and the particle boards were interlaid one on top of the other to form the crib. Four layers of particle board were installed at the top of the crib, as used underground. The total height of the crib was 19.25 inches and the cross-section was 8 x 16 inches. Figure 5.12 shows the crib before testing. During the test, a long crack appeared at sixty degrees to the horizontal when the load increased to 1760 psi. The crib deteriorated along the crack as the load increased until the load reached its maximum value and the crib failed violently. Figure 5.13 is the crib after failure and figure 5.14 is the load-deformation curve of the crib. Comparing figure 5.14 with figure 5.1, it can be noticed that, although particle boards only constitute 9 percent of the total crib volume, the yieldability of the crib has been improved significantly over that of a concrete crib.

Another type of crib similar to the sandwich crib is the grouted



Figure 5.12. Sandwich crib before testing.



Figure 5.13. Sandwich crib after testing.

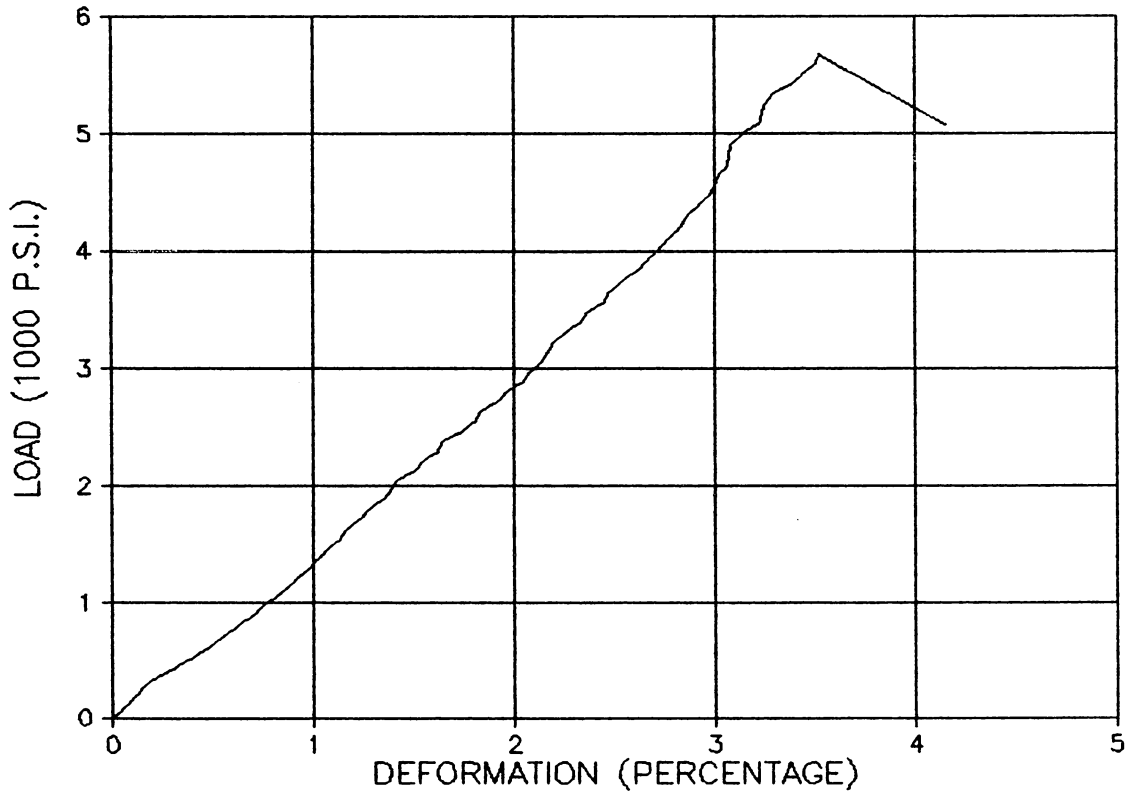


Figure 5.14. Load-deformation curve of a sandwich crib.

skeleton crib (Spengler, 1978). The crib was engineered in South Africa. An exploded view of the grouted skeleton crib is shown in figure 5.15.

The main components are as follows:

- (1) a normal timber crib,
- (2) a rectangular knitted polyethylene bag with a draw-string at the open end,
- (3) a knitted polyethylene cover, and
- (4) grout with a sand : cement ratio of 2:1.

To build the crib, the bag is rolled down and placed on the floor, and a timber skeleton crib is built in the bag to within a few millimeters of the roof. The cover is pulled over the top of the crib to overlap the timber members by approximately 15 cm (5.9 inches) , and the crib is wedged in the normal manner. The bag is then pulled up to overlap the cover, and the draw-string is tightened. Finally, the grout is injected. To prevent ballooning of the bag when the grout is being injected, another skeleton crib can be built around it, a suitable rope wound around it, or shuttering erected (Spengler, 1978).

Two 125 x 60 x 60 cm (49.2 x 23.6 x 23.6 inches) grouted skeleton cribs were tested in a 1000 ton press by researchers in South Africa. Figure 5.16 shows the load-deformation curves of grouted skeleton cribs and a 120 x 60 x 60 cm (47.2 x 23.6 x 23.6 inches) standard sandwich crib. The curves for the skeleton cribs show a difference in behavior in the 25 to 45 cm (9.84 to 17.7 inches) convergence range, which can possibly be attributed to the method of construction rather than to the quality of the pack. As shown by the graphs, the initial load-bearing and controlled yield characteristics of the skeleton cribs were far

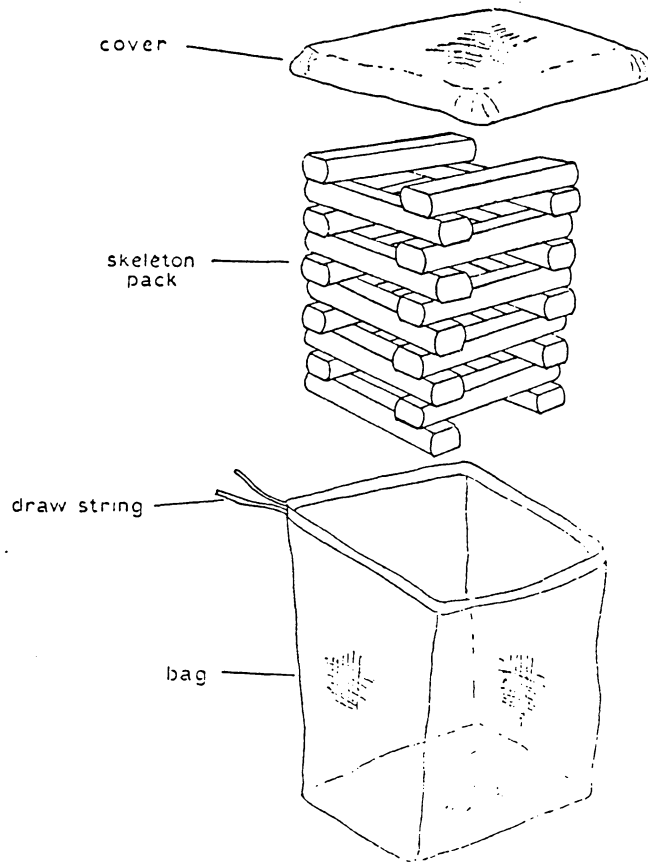


Figure 5.15. Skeleton crib.
(Spengler, 1978)

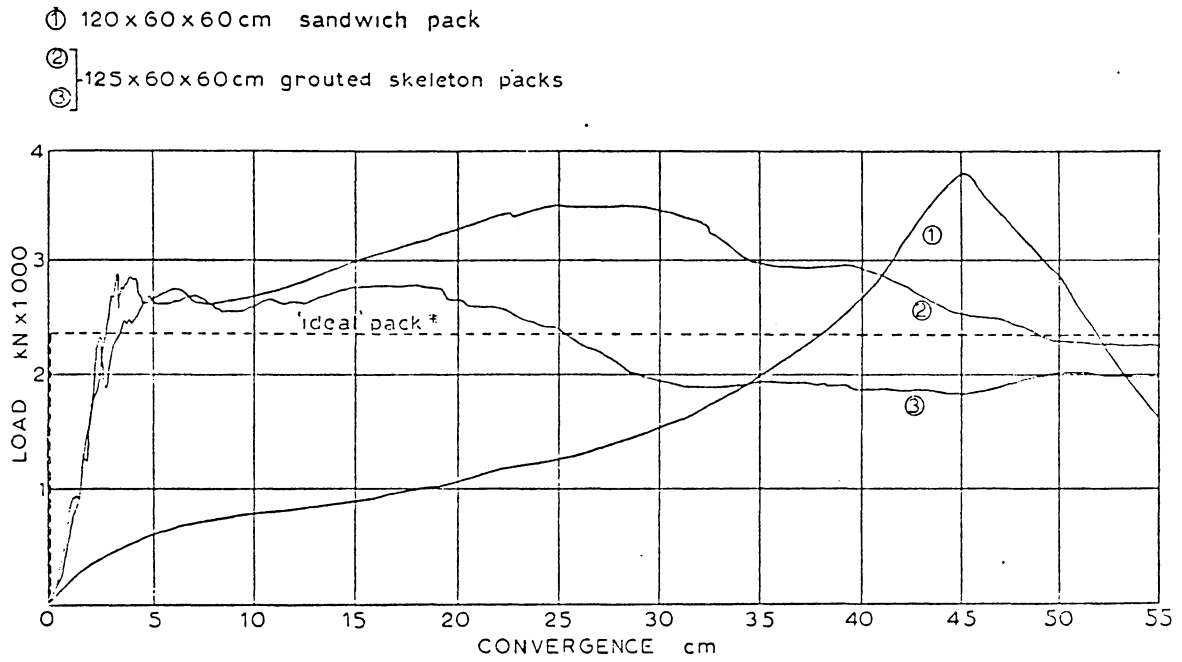


Figure 5.16. Comparison of the load-deformation characteristics of the sandwich crib and skeleton crib. (Spengler, 1978)

superior to those of the sandwich crib. As the rigid core of the grouted skeleton crib was in direct contact with the platens, the crib accepted a high initial load with very little initial convergence. The timber in the crib acted, to a large degree, as reinforcing rather than load-bearing. In this way, the fractured grout was contained to provide a satisfactory yield.

Although the load-deformation characteristics of the grouted skeleton crib are better than that of sandwich crib, its use may be limited since it is expensive and time-consuming to build. However, in some cases, it may be the only tenable means of ground control.

Concrete supports have been shown to have a higher compressive strength than timber supports, but it is difficult to make concrete into a mechanism. Thus, the use of concrete is also limited. Steel can compensate for this disadvantage, and steel support is the topic of the following chapter.

CHAPTER 6 STEEL SUPPORTS

The qualities of steel as a supporting material have caused it to be used as a replacement for wood in many supporting areas, especially in the longwall face where steel supports, including powered supports, are almost exclusively used. Steel supports also play a very important role in entry support. The basic characteristics of steel can be summarized as follows (Biron, 1983):

1. Steel is a very homogeneous material, free of natural defects, allowing lower safety factors to be used in designing.
2. Compared with timber supports, steel supports are resistant to fire.
3. Steel has a Young's modulus much greater than that of any other structural material, giving it an advantage against buckling.
4. Steel can be manufactured in various of alloys to meet high requirements set in the design.
5. Steel is the material least affected by atmospheric conditions such as temperature and humidity.
6. Some steel supports are reusable. Completely deformed supports can be reclaimed as scrap.

Steel is, however, an expensive material. In order to give the support a desired load-deformation characteristic, steel has to be manufactured into a complex mechanism, which further increases the cost. Roadways supported by steel arches and the like represent a major capital investment.

In this chapter, three kinds of steel supports are discussed, namely

yielding steel posts, steel friction props and steel arches.

6.1 Yielding Steel Post

A yielding steel post with a capacity of 45 tons and a closure allowance of 24 inches in a 6 to 7 foot seam height has been developed by the U. S. Bureau of Mines (Dunford, 1986). The post mechanism is a three piece unit consisting of a top and bottom leg made from standard steel pipe and separate foot brackets. The post develops its load carrying ability when the lower pipe, with an attached interference ring, is forced into the larger top leg. The walls of the top leg are deformed radially and along the axis. Yield continues until the unit bottoms out. Laboratory and field tests on the post have been conducted by the Bureau of Mine.

In an attempt to provide a reduced profile, high strength, low cost, and yielding support, the Bureau examined various options. Several concepts and designs were studied. All used steel components, because of the strength and availability of the material. Different shapes and yield mechanisms were used to obtain the desired load and yield characteristics. The most successful design consisted of an interference ring welded to the outside of the smaller pipe. The two pipes were then forced together until the ring caused the larger pipe to deform radially (figure 6.1). The yielding procedure of the post is similar to the extrusion process for manufacturing seamless pipe.

Although the ring yield mechanism worked well for the initial tests, there was consistent failure due to buckling in the 6 to 8 foot posts.

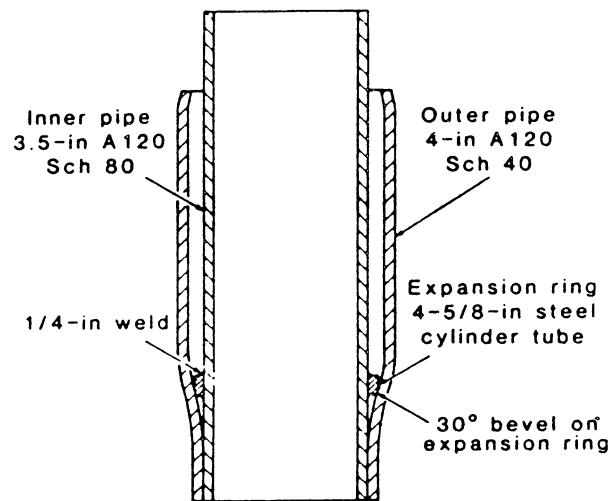


Figure 6.1. Structure of a yield steel post.
(Dunford, 1986)

The joint in the middle of the column adds to the problem by creating an offset which promotes buckling failure. Several changes in the design were made by the Bureau to provide an acceptable load-deformation curve without the buckling induced failure. The size and shape of the interference ring were specified, and a bevel was added to the leading edge of the interference ring to eliminate the plowing action of a sharp edge. The original 90 degree angle at the upper edge of the expansion ring would imbed in the large pipe and cause an immediate stress rise by gouging the metal, thus causing failure due to buckling. After a number of tests, it was found that a 30 degree bevel along half an inch of interference between the inner diameter of the large pipe and the outer diameter of the interference ring resulted in an acceptable load curve and a smooth yielding mechanism (Anderson, 1986). During the testing, a heavy grease was applied to some of the units, and although it did not change the general shape of the loading curve, it lowered the load value that could be obtained with a given interference. For example, for an interference of 0.545 inch, without grease, a 55 ton load could be developed before buckling, but for the same interference, with grease, only 45 tons could be developed. Further testing showed that, by increasing the interference and greasing the ring area, higher loads could be developed with less chance of buckling. In several cases a 0.565 inch interference was used and loads of greater than 65 tons were achieved (Dunford, 1986).

In addition to the changes made based on the physical tests, mechanical theory was also applied to the post design. The method of yielding in the larger pipe is analogous to the metallurgical process of

tube expansion. In this process a tube is pushed or pulled over a mandrel to increase the tube diameter, as shown in figure 6.2. A detailed mathematical analysis of the process of tube expansion has been developed by Avitzur (1968). This analysis is based on the elasticity theory, an application of VonMises' yield criterion, and upper bound theorem. The assumptions required for the Avitzur analysis are:

1. A solid, rigid mandrel.
2. A constant friction force during deformation.
3. A constant angle of attack between the mandrel and the tube.

From the Avitzur's analysis, the stress in the unexpanded portion of the outer pipe and the deformation rate of that portion have the following relationship:

$$\begin{aligned} \frac{\sigma_{xb}}{(2/\sqrt{3})} = & - \frac{1}{(R_o/R_i)-1} \left\{ \frac{\sqrt{3}}{2} F_2(r) \ln\left(\frac{v_o}{v_f}\right) - \left(\frac{\alpha}{\sin^2 \alpha} - \cot \alpha\right) + \right. \\ & + m \left[\frac{1}{2} \cot \alpha \ln\left(\frac{v_o}{v_f}\right) + \frac{L}{R_{if}} \right] + \\ & \left. + \left(\frac{R_o}{R_i}\right)^2 \left(\frac{\alpha_o}{\sin^2 \alpha_o} - \cot \alpha_o\right) \right\} \end{aligned} \quad (6.1)$$

where

$$\begin{aligned} F_2(r) = & \frac{1}{\sin^2 \alpha} \left[\cos \alpha \sqrt{1 - (11/12) \sin^2 \alpha} - \right. \\ & - \cos \alpha_o \sqrt{1 - (11/12) \sin^2 \alpha_o} + \\ & \left. + \frac{1}{\sqrt{132}} \ln \frac{\sqrt{11/12} \cos \alpha + \sqrt{1 - (11/12) \sin^2 \alpha}}{\sqrt{11/12} \cos \alpha_o + \sqrt{1 - (11/12) \sin^2 \alpha_o}} \right] \end{aligned}$$

and $\alpha_o = \sin^{-1}\left(\frac{R_o}{R_i} \sin \alpha\right)$

where m is a shear factor, L is the length of land of the mandrel and all other symbols are illustrated in figure 6.2. Equation 6.1 is the basic equation for the design of a steel yielding post. Theoretically, the optimum angle of the interference ring can be found by differentiation of equation 6.1 if the dimension of the pipes and the deformation rate of the outer pipe are known, and vice versa.

Laboratory tests were performed by the Bureau of Mines to measure the load required to cause the post to yield. The measured yield forces were lower than those predicted by the tube expansion theory. This result can be attributed to the non-rigid action of the expansion ring and the anisotropic behavior at the tube welded seam.

The Bureau of Mines also conducted two field trials. In the first trial, ten prototype units were built. The posts were designed to be used in seams with a height of 72 to 80 inches. The posts had a total potential yield of 23 inches, an expected load capacity of 50 tons, and a weight of 112 pounds. These units were installed as supplemental support in the tailgate of a western U. S. coal mine. At that time, the mining company was having great difficulty maintaining air flow and escapeway clearance through the entry because of massive floor heave between the crib rows. As the longwall face proceeded past the test area, all of the posts yielded between one and three inches. Five of the posts exhibited significant yield and one of them buckled, leading to the conclusion that the post capacity should be reduced. After reviewing the laboratory test data, the researchers concluded that a 10 percent reduction in load capacity would insure column stability. In the second trial, the amount of interference between the expansion ring on the inner pipe and the

inner diameter of the outer pipe was decreased. This lowered the yield capacity from 50 tons to 45 tons and thus decreased the possibility of column buckling. An additional 12 inch-square plate was welded to the 7 by 7 inch roof plate, to increase the bearing area which proved to be too small in the first trial. The posts were installed in two configurations. First, the posts were placed on a single track located in the center of the entry. These posts were installed on two-foot centers. The second configuration had the posts on two parallel tracks, centered in the entry. The posts were placed on two-foot centers but not aligned with one another on the rails. This placed the posts on four-foot centers on each rail but provided the same roof bearing support as the first configuration. Under 1500 feet of cover (over the trial site), loads of 12 tons per linear foot were expected. During the first month after installation, loads of 10 tons per linear foot were measured. After six months the average load was nearly 12 tons. A inspection of the site found that the section supported by yielding steel posts was more open than the section of entry supported by cribs only.

The Yielding Steel Post has shown in laboratory and field testing that it is a workable mechanism for supporting ground. With further improvement in its design, the post may gain wide acceptance in underground mining.

6.2 Steel Friction Props

Steel friction props combined with articulated caps were the main supporting system in the early longwall faces and, in fact, that system

is still widely used in some developing countries. As modern technology advances, the system is being replaced by powered supports. However, this does not mean that the steel friction prop is disappearing and it is still used as an entry support due to its yieldability.

In this section, two types of steel friction prop are considered. One is a slow-increasing resistance type and the other is a rapid-increasing resistance type.

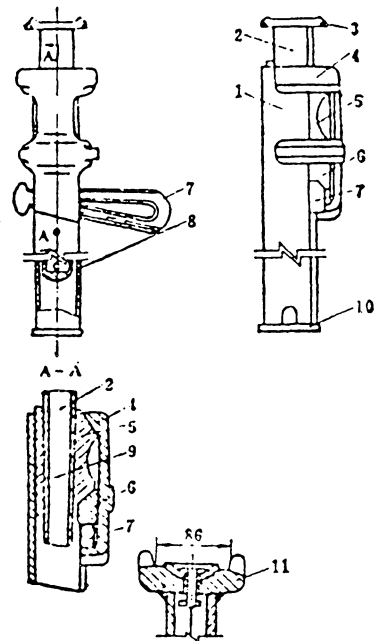
6.2.1 HZJA Rapid-Increasing Resistance Steel Friction Prop

The HZJA is a kind of rapid-increasing resistance steel friction prop manufactured in China (Song, 1983). Its structure is shown in figure 6.3. Its working mechanism is quite simple. When the load on the prop exceeds the friction force between the moving rod and friction plate, the rod begins to retreat. Since the moving rod has a certain slope with the upper end wide and lower end narrower, the locking band is expanded as the rod retreats. The locking force, and hence the friction between the moving rod and the friction plate, increase. Therefore, the working resistance of the prop increases gradually as the rod is retreating. A typical load-deformation curve is shown in figure 6.4.

The locking force N , which is the force normal to the rod, consists of two parts:

1. After installation of the horizontal wedge, the locking band will expand a distance S_1 , and the reactive force of the locking band to the rod is

$$N_1 = KS_1 \quad (6.2)$$



- 1 - prop body, 2 - moving rod, 3 - cap
4 - locking band, 5 - vertical wedge
6 - medium wedge, 7 - horizontal wedge
8 - limiting block, 9 - friction plate
10 - pedestal, 11 - connecting cap.

Figure 6.3. The structure of the HZJA steel friction prop. (Qian, 1983)

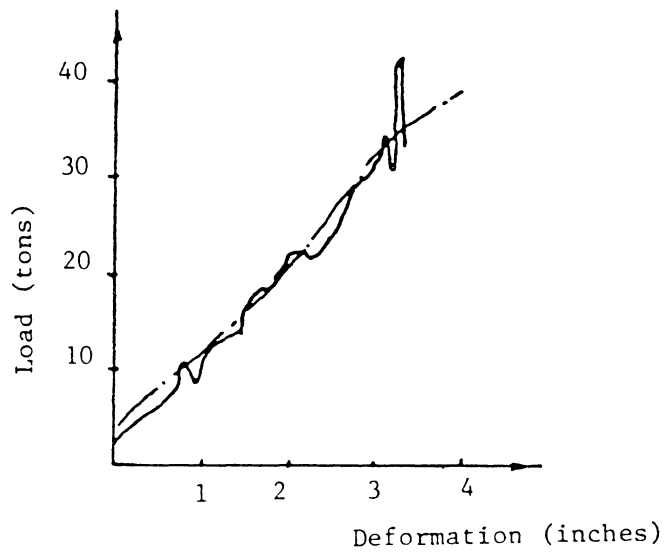


Figure 6.4. The load-deformation curve of a HZJA prop. (Qian, 1983)

where K is the rigidity modulus of the locking band.

2. As the rod retreats it expands the locking band for a distance of S_2 , and the reactive force is:

$$N_2 = KS_2 = K\epsilon_m \delta \quad (6.3)$$

where δ is the slope of the rod and ϵ_m is distance that the rod has retreated.

Therefore, the resistance of the prop at any ϵ_m position is:

$$\begin{aligned} R &= 2Nf \\ &= 2f(N_1 + N_2) \\ &= 2Kf(S_1 + \epsilon_m \delta) \end{aligned} \quad (6.4)$$

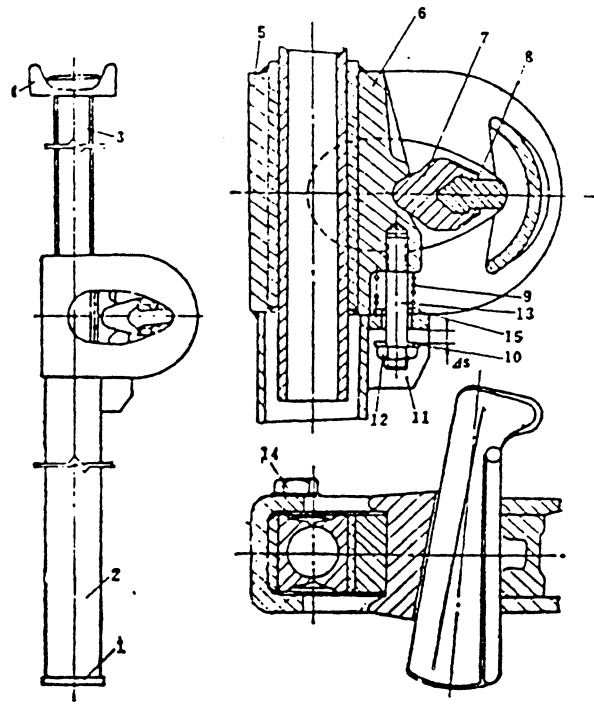
where f is the friction coefficient.

Since the largest yielding value of the HZJA prop is 4 inches, it is not suitable for use in a mine where a large yielding value of the support is needed for roof control.

Comparing figures 6.4 and 4.2 one can see that the initial stage of the load-deformation curve of the Micon Yield Capsule post is very close to that of the HZJA.

6.2.2 HZWA Slow-Increasing Resistance Steel Friction Prop

The HZWA is another kind of steel friction prop (Song, 1983). Its structure is shown in figure 6.5. Its working mechanism is also uncomplicated. When the horizontal wedge is inserted into the locking band, the prop begins to bear load. Initially, the sliding block is pushed upward by the spring causing the wedge group, including horizontal and medium wedges, to tip upward about 6 to 8 degrees. After bearing a



- 1 - pedestal, 2 - prop body, 3 - moving rod
4 - cap, 5 - locking band, 6 - sliding block
7 - medium wedge, 8 - horizontal wedge
9 - spring, 10 & 15 - washers, 11 - buttress
for screw, 12 - screw nut, 13 - screw bolt
14 - screw.

Figure 6.5. Structure of the HZWA steel friction prop. (Qian, 1983)

certain load, the wedge group begins to turn downward, together with the sliding block, as the moving rod retreats. The load at this point, R_0 , is called the initial moving load (usually 5 to 8 tons). As the load continues to increase, the wedge group gradually turns to a horizontal position. The load at the moment when the wedge group becomes horizontal is called the initial working resistance R_A . R_A is usually between 22 or 28 tons. Thereafter, the rod continues to retreat while the wedge group does not move anymore. The resistance increases slowly, and is dependent upon the slope of the moving rod. Finally the rod retreats to its final position, its retreated distance is ϵ_B and the final working resistance is R_B , (see figures 6.6 and 6.7).

In general, The resistance of the HZWA is obtained through following three procedures:

1. After inserting the horizontal wedge (see figure 6.5), the locking band has a deformation of S_1 . The reactive force is:

$$N_1 = KS_1. \quad (6.5)$$

Therefore,

$$\begin{aligned} R_0 &= N_1 \sin\theta + 2N_1 f \cos\theta \\ &= KS_1 \sin\theta + 2KS_1 f \cos\theta \\ &= KS_1 (\sin\theta + 2f \cos\theta) \end{aligned} \quad (6.6)$$

where K and f have the same meaning as mentioned before. θ is the upward angle of the wedge group (see figure 6.6). Apparently the more tightly the horizontal wedge is inserted, the larger the R_0 value is.

2. As the wedge group turns downward, the locking band deforms further and produces a reactive force N_i .

$$N_i = KS_i$$

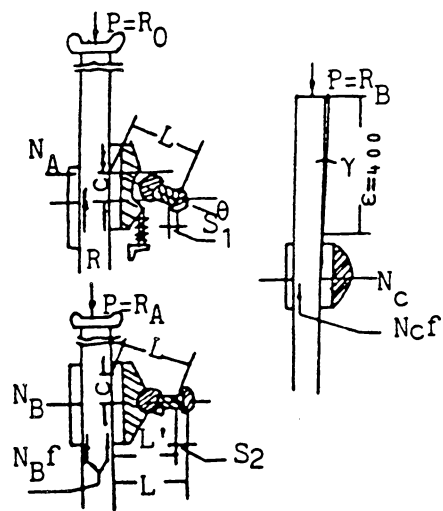


Figure 6.6. Sketch for load-deformation analysis of HZWZ steel friction prop. (Song, 1982)

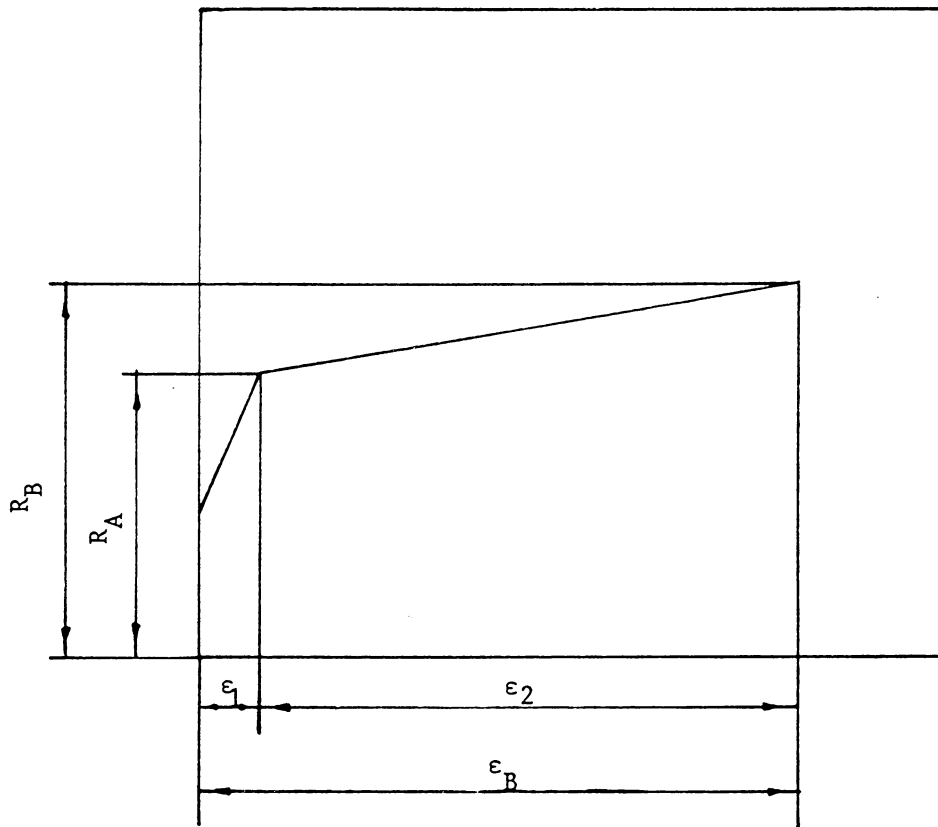


Figure 6.7. Stages of the load-deformation curve of a HZWA prop. (Song, 1982)

$$= KC(\cot\theta - \cot\theta\cos\theta/\cos\theta_i) \quad (6.7)$$

The resistance is:

$$R_i = R_0 + KC\cot\theta(1 - \cos\theta/\cos\theta_i) (\sin\theta_i + 2f\cos\theta_i) \\ (R_0 \leq R_i \leq R_A) \quad (6.8)$$

where C is the distance retreated by the sliding block during the time when the wedge group turns from the original position to the horizontal position, and θ is the original upward angle of the wedge group while R_i and θ_i are the resistance and the upward angle of the wedge group, respectively, at any position during its turning process. When $\theta_i = 0$, $R_i = R_A$, the initial working resistance. If there is no relative movement between the rod and the sliding block, $C = \varepsilon_1$, the retreated distance of the rod in the corresponding period.

3. After the wedge group becomes horizontal, the moving rod continues to retreat itself and expand the locking band since it has a slope of 1/1250. Theoretically the reactive force of the locking band to the rod N_3 is:

$$N_3 = KS_3 \\ = K\varepsilon_i \delta \\ = K\varepsilon_i / 1250. \quad (6.9)$$

Therefore, the resistance is:

$$R_i = R_A + K\varepsilon_i f / 1250 \\ (R_A \leq R_i \leq R_B) \quad (6.10)$$

where S_3 and ε_i are the deformation of the locking band caused by the retreating of the moving rod and the retreated distance of the rod respectively after the wedge group stops moving, and δ is the slope of the moving rod.

A typical load-deformation curve of the HZWA prop is shown in figure 6.8. The curve is very similar to that of the Super Post.

6.3 Steel Arch

The steel arch is another category of steel support used in underground entries. There are three types of steel arches, namely the rigid arch, the articulated arch, and the yielding arch. The distinctions between the three lie in the connections between the arch segments. For the rigid type, no movement at the connection points, neither rotation nor sliding, is allowed. For the articulated type, rotation can take place but not sliding. In the yielding type, sliding between segments is expected. In this section the mechanical behaviors of steel arches are analyzed.

The stress in the rigid or continuous arch was analyzed by Arioglu (1982). He determined that the maximum stress in the arch is:

$$|\sigma| = \frac{q_t r}{F} + \frac{A_y (h' + 0.5A_y/q_t)}{W} \quad (6.11)$$

where $|\sigma|$ = the absolute stress value, in psi,

F = section area of the profile, in square inches,

W = section modulus of the profile, in cubic inches,

q_t = uniform roof load, in pound per inch,

h' = height of the vertical section of the arch, in inches,

r = radius of the arch, in inches,

$$A_y = \frac{(0.785h' + 0.666r) q_t r^3}{0.666h'^3 + \pi r h'^2 + 4h' r^2 + 1.57r^3}$$

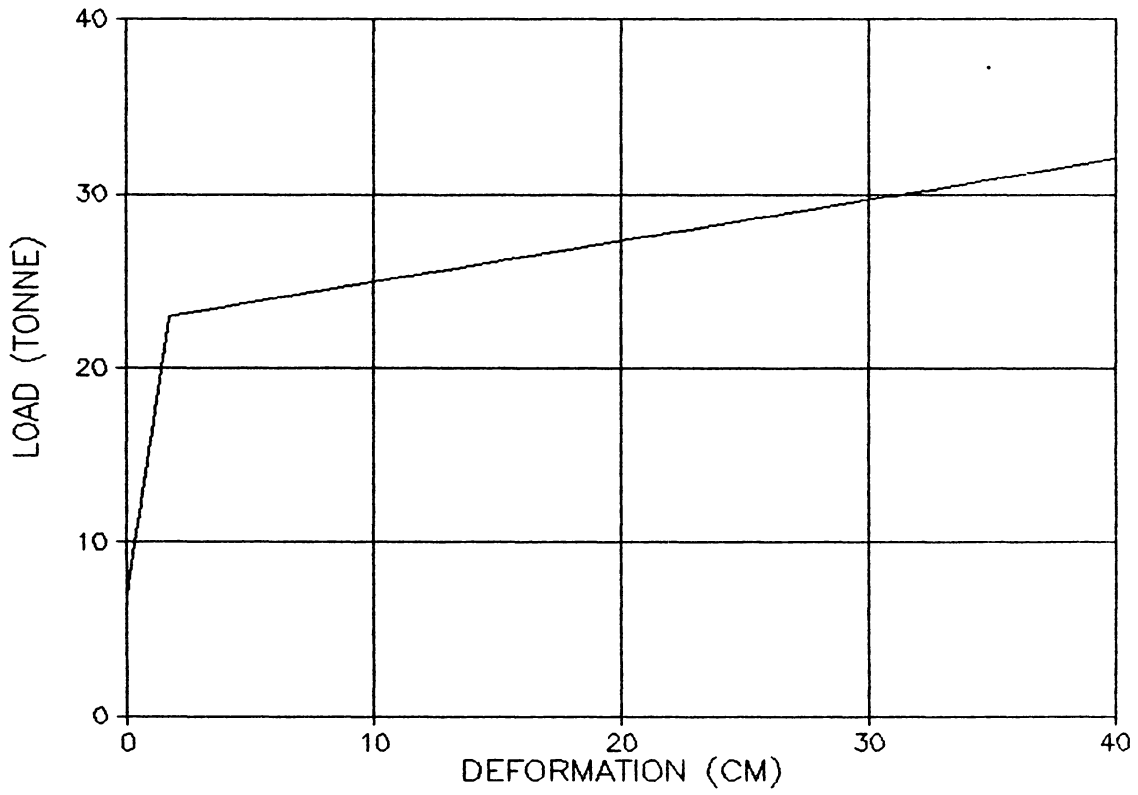


Figure 6.8. A typical load-deformation curve of a HZWA prop.
(Song, 1982)

In rigid arch design, the strength of the steel should be larger than the value defined in equation 6.11.

Arioglu and Biron (1983) also analyzed the stress in the articulated (Moll) arch. They gave following formula:

$$|\sigma| = \frac{q_t r}{F} + \frac{0.09 q_t r^2}{W} \quad (6.12)$$

for two articulations and

$$|\sigma| = \frac{q_t r}{F} + \frac{0.125 q_t r^2}{W} \quad (6.13)$$

for three articulations, where q_t , r , F , and W have the same meanings as in equation 6.11.

The Mechanical Testing Branch at the MRDE of the British National Coal Board conducted some tests on rigid arches (Sadler, 1984). The arches were tested on the roadway test rig. The loading condition is single-point load at the top of the crown. In order to gain information on differences in performance, comparative tests were made on arches of the same profile (3.4m x 2.4m) and section (102mm x 102mm H-section), but of different constructions, namely:

1. an arch with a welded crown joint to represent a continuous arch,
2. a three-piece arch (four-bolt fishplated joints),
3. a two-piece arch (four-bolt fishplated joint), and
4. an arch pin-jointed at the crown.

The load-deformation curves of the four arches tested are shown in figure 6.9. The following points can be noticed from figure 6.9:

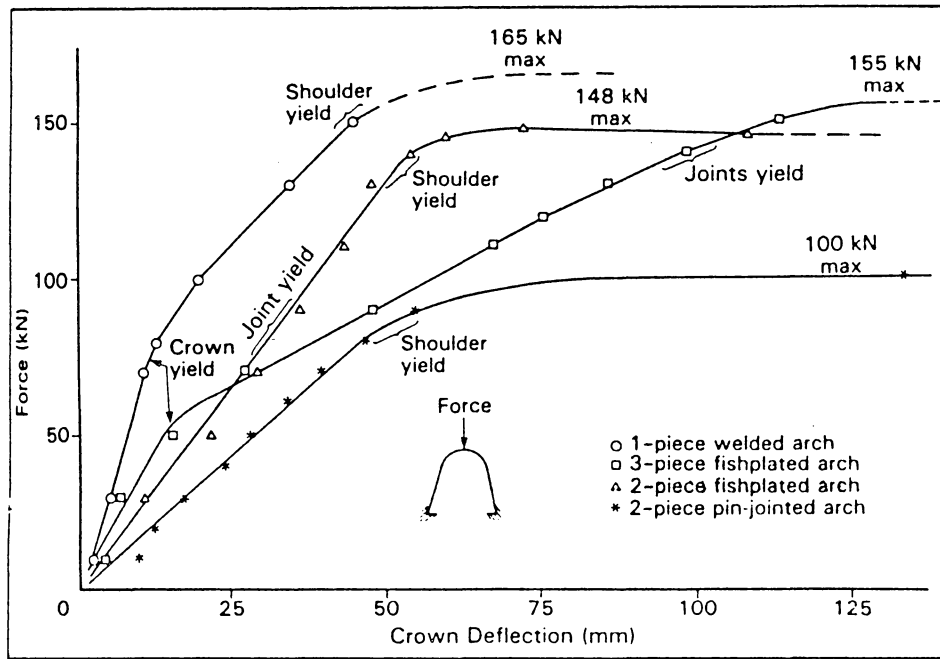


Figure 6.9. Load-deformation curve for single-point crown loading tests. (Sadler, 1984)

1. The stiffnesses of the three-piece arch and of the one-piece welded arch followed the same pattern, and both changed two times. They were different from those of the other two arches. The first stiffness change occurred when the crown yielded. The crown yielded at a very low load since the bending moment at the crown is the largest. The second change came at the time when the shoulder of the arch yielded. The shoulders are subject to the second largest bending moment in the arch. Note that, in figure 6.9, the second change of the stiffness for the three-piece arch occurred after the joints yielded, since the joints are at the shoulder.

2. The stiffnesses of the two-piece fishplated arch and of the two-piece pin-jointed arch followed the same pattern and both changed once. The joint reduced the bending moment at the crown, and thus the stiffness changed only when the shoulder yielded.

3. Between the two-piece arches, the yielding strength of the fishplated arch was much greater than that of the pin-jointed arch. To understand this phenomenon, one has to keep in mind that the bending moments at the crown and at the shoulder are opposite in sign and hence the bending moment at the crown may actually help to reduce the bending moment at the shoulder. Since the pin-jointed type of connection is more articulated than the fishplated type and it eliminates the bending moment at the crown more completely than the fishplated type, the bending moment at the shoulder for the pin-jointed type will be larger than that for the fishplated type. Thus the pin-jointed type was shown to yield at a lower load.

4. Among the four arches, the three-piece fishplated arch was the

most deformable one and the one-piece welded arch is the least but has the highest yielding load. Generally speaking, the three-piece fishplated arch can be considered as the best one, being more yieldable and at the same time maintaining a high load.

During single-point crown loading investigations, simple approximate relationships were found to exist between the strengths of a fishplated arch, the arch diameter and the elastic modulus of the arch section. Although the equations are not exact they are accurate enough for most comparative purposes. For example, considering a continuous arch, i.e. one with no fishplated joints, the theoretical formulae for the forces required to cause yield and collapse are (sadler, 1984):

$$\text{Crown yield } W_y = 2.2 Z/D \quad (6.14)$$

$$\text{Collapse } W_c = 5.8 Z/D \quad (6.15)$$

where Z and D are explained in figure 6.10. These equations give results which vary from calculated values for particular arches by up to 15 percent. The variation depends upon the arch size and occurs because the arches are not geometrically proportional, for example, the leg length is not a fixed proportion of the diameter.

In reality, arches are not continuous because of the presence of the fishplated joints. Strength tests conducted by MRDE on a range of three-piece fishplated arches showed that crown yield occurred at load values within 20 kN (4500 lbs) of the loads predicted by the yield equation for a continuous arch; therefore this equation is acceptable for determining yield loads for three-piece arches. For the two-piece fishplated arch, the load-deformation curve (figure 6.9) gives no indication that crown yield has occurred. However, the two-piece arch

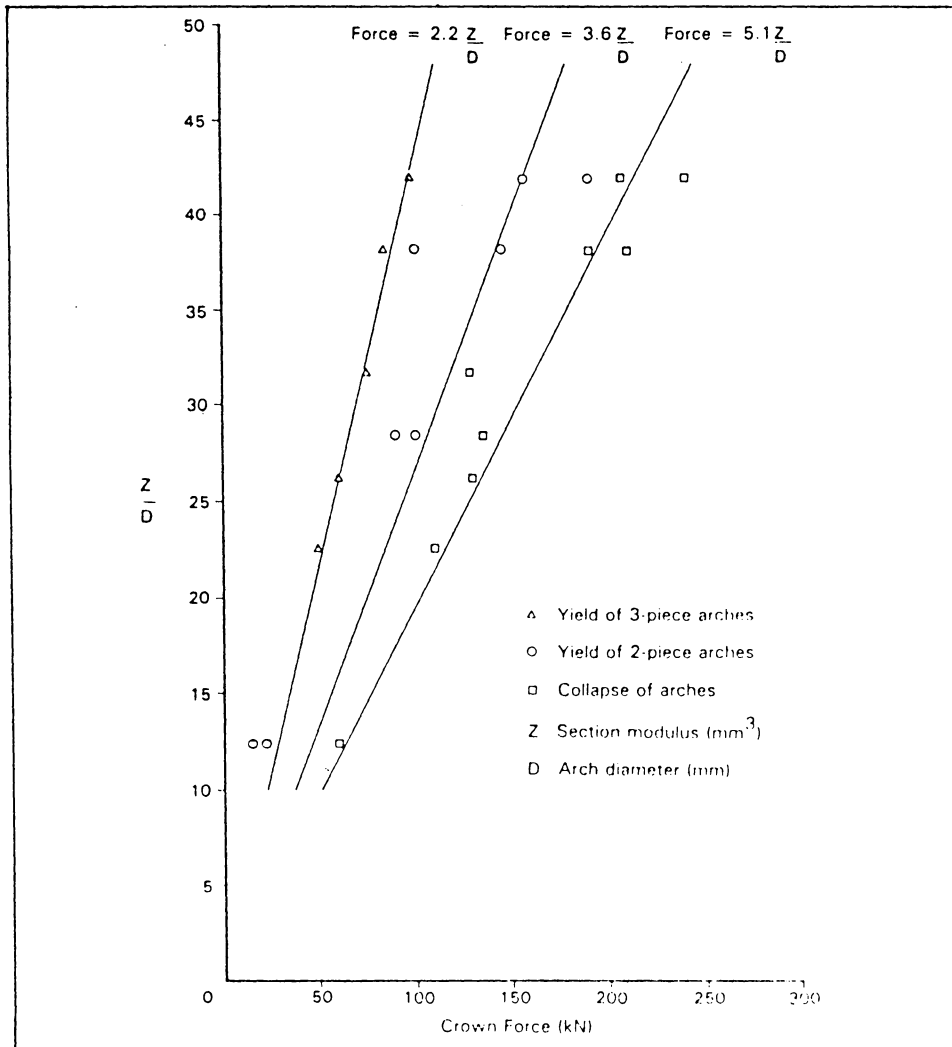


Figure 6.10. Strength of arches from single-point crown loading tests. (Sadler, 1984)

did yield at the shoulder. From figure 6.10, a 'best fit' equation for yield strength of two-piece arch is:

$$W_y = 3.6 Z/D \quad (6.16)$$

The strength of a fishplated arch at collapse is similar to that of a continuous arch. 'Best fit' lines from the experimental results (figure 6.10) indicate that collapse loads of both two and three-piece arches could be found from the equation:

$$W_c = 5.1 Z/D. \quad (6.17)$$

The yieldability of the rigid arch in some cases can not meet the deformation requirement of the entries. Thus yielding arch was developed to cope with this problem. The first yielding arches were designed by Toussaint and Heinzmann with U-section profiles and this type of arch is commonly known as the TH arch. A TH arch is shown in figure 6.11. This type of arch is composed of three or more segmental lengths of rolled steel whose cross-sections are heavily flanged U-shapes. A U-shaped section has a high torsional resistance that allows it to be twisted out of the vertical without significantly decreasing its strength (Peng, 1978). The curved sections nest together at the end to form a 0.3 to 0.4 meter (11.8 to 14.7 inches) overlapping joint. Heavy U-bolt clamps are installed in pairs over the joints. Under normal circumstances, the radius of the top section is smaller than those of the side sections. As the roof pressure increases, the radius of the top section also increases. When the radius of the top section is equal to those of the side sections, and the axial load along the joint exceeds the friction resistance between the two overlapped segments, sliding will occur at the joint. As the sliding continues, the pressure on the arch will be

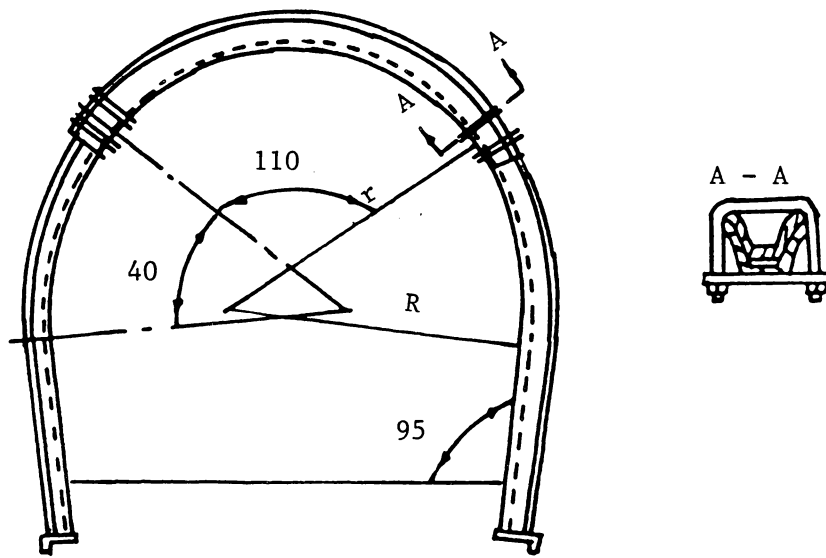


Figure 6.11. Structure of Toussaint-Heizmann arch. (Qian, 1983)

gradually reduced until the axial load at the joint is less than the friction resistance and the arch reaches a new equilibrium. This process continues to repeat until the joints become 'solid'. The initial yielding load of the yielding arch depends on the geometry of the arch segments and the tightness of the clamps.

In addition to the U-section, other types of section profile were also used in the design of yielding arches. Two of these are a bell-shaped section and an I-section. The yielding arch of bell-shaped section is referred as GP type arch and that of I-section is called GI type. Modeling tests were performed in the laboratory to determine the load-deformation curve of the three types of yielding arches (TH, GP and GI) (Qian, 1983).

Figure 6.12 shows the load-deformation curves of the arches when confined and figure 6.13 is the curves of the arches without confinement. Comparing figure 6.12 and figure 6.13, it is obvious that the confined arches can resist a much higher load than the single-point loaded arches. The load-deformation curves of the TH type arch are superior to those of the GP and GI type because the load of both the GP type and the GI type decrease after the initial yielding, while load for the TH type is almost constant throughout the loading period. The good load-deformation characteristics of the TH type yielding arch can be attributed to its joint structures. Figure 6.14 shows the load-deformation curve of the joint of a TH type yielding arch. The curve is almost as good as that of a hydraulic prop.

There are other types of steel supports which utilize the same mechanism as steel yielding arches. For example, to support an entry

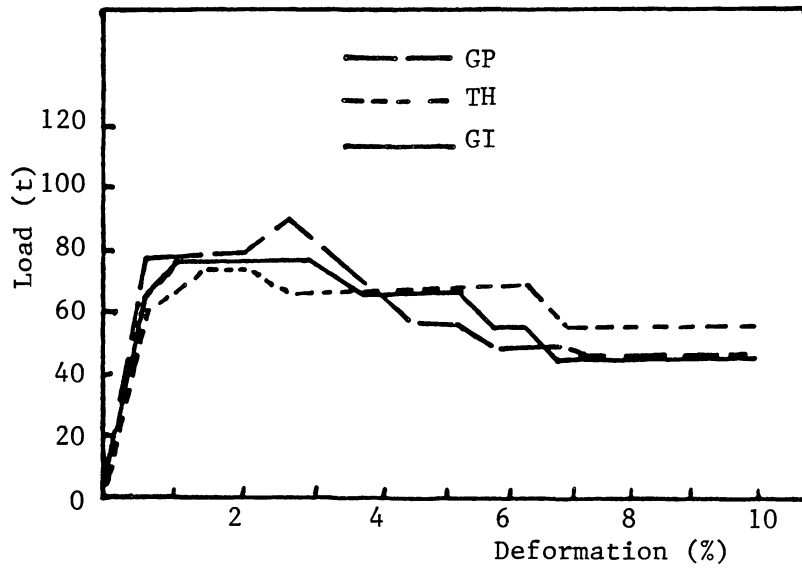


Figure 6.12. Load-deformation curves of the yield arches for single-point crown loading with the arches being confined. (Qian, 1983)

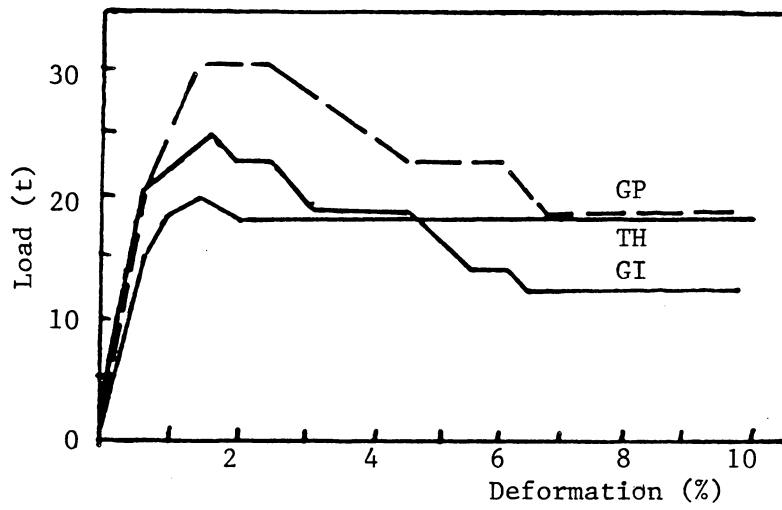


Figure 6.13. Load-deformation curve of the yield arches for single-point loading without confinement. (Qian, 1983)

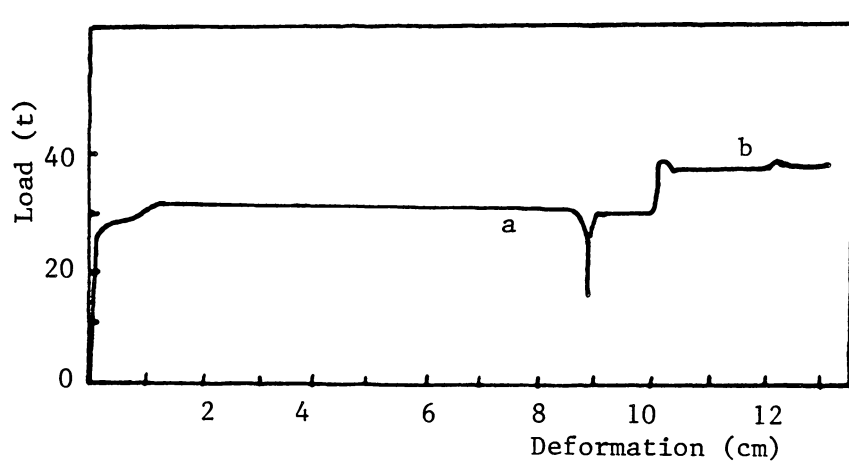


Figure 6.14. Load-deformation curve of the joint of the Toussaint-Heizmann arch. (Qian, 1983)

with a circular cross-section, yielding ring sets were developed (Peng, 1978). A yielding trapezoid set was developed to support entries with trapezoid cross-section (Qian, 1983). The U. S. Bureau of Mines developed arch canopies for rehabilitation of high-roof-fall areas (Allwes, 1986).

Steel arches are expensive supports. However, they can be used to maintain important entries and can last for a long time.

CHAPTER 7 SUMMARY AND RECOMMENDATION

7.1 Summary

In this thesis, twelve types of supports have been evaluated. Emphasis was placed on the mechanical behavior of these supports. To assess the mechanical behavior of the support, the relationships between the roof deflection and the resistance of the support were explored. Two kinds of relationship were introduced, namely hyperbolic and linear relations. According to the hyperbolic relationship, a good support should have the following characteristics:

1. The slope of the initial portion of the load-deformation curve should be as steep as possible. Ideally, it should approach the corresponding characteristic for the intact rock.

2. A definite, predictable yield point should be reached, after which the support should behave in such a way that its load increases slowly as it deforms.

Based upon the linear relationship, the support may have a constant stiffness from the beginning to the end. The value of stiffness depends upon what kind of roof the support is going to control. Generally, the following can be said about the stiffness of the support:

1. If the abutment pressure dominates, then the resistance of the support is of little significance, in other words the deflection of the roof is non-resistable. In this case the function of the support is to prevent local roof fall, and thus the support should be yieldable enough to accommodate the non-resistable deflection, at the same time being

stiff enough to prevent local delamination and cracking.

2. If the abutment pressure is not very large and the roof is flexible, the support can effectively control the deflection. In this case the stiffness of the support can be determined according to the deflection control requirement.

A support can be classified as a rigid or yielding support, based on its deformability. A rigid support is one that undergoes only elastic deformation and does not perform a supporting function after the support material yields. A yielding one is such a support that its deformation is larger than the elastic deformation of the support material and its load can be maintained or increased as it deforms. There are two types of yielding support, namely the mono-stiffness yielding support and the bi-stiffness yielding support. The bi-stiffness yielding supports are referred as Category I supports and they satisfy the criterion set by the hyperbolic relation. The rigid and mono-stiffness yielding supports are called Category II supports and they meet the requirement of the criterion dictated by the linear relation.

The results from evaluation of each individual supports are summarized as follow:

1. Plain timber post: There are two types of plain timber post, namely the circular post and the square post. The square post is superior to the equivalent circular post in terms of support capacity. The plain timber post is a rigid support and usually deforms less than one inch. Eccentric loading can affect its performance. Moisture content, specific gravity, and other natural factors can influence its strength. These factors also have an impact on the timber crib, the Micon

Yield Post, the Super Post, and the Wedge Prop. Finite element analysis indicates that it is very likely that the failure of a circular post will begin at the center of the post. Most plain timber posts are used as temporary support.

2. Timber crib: The timber crib is a yieldable support. It can yield up to 50 percent of its height while the load continues to increase steadily. Its load-deformation is not a linear curve. Stability is an important advantage of the timber crib and it can be more than 50 times as stable as a timber post. Shrinkage due to loss of moisture content may affect the performance of timber cribs and, creep is another factor that may create problems when a timber crib is used for ground control. A timber crib occupies more space than other types of support and take more time to assemble. It can be used under weak or medium strength roof to maintain important intersections, gateroads and other areas.

3. Timber gallery set: The timber gallery set is more yieldable than the timber post. Its deformation consists of two parts, namely the compressive deformation of the timber and the deflection of the set member. When designing a gallery set, the individual members must be considered as a beam-column, instead of a beam or column alone. Timber gallery sets are mainly used to maintain the secondary entries under medium strength roof conditions.

4. Micon Yield Capsule: The Micon Yield Capsule is a yieldable support. Based on the preliminary testing, it can yield 3 to 4 inches more than a plain post, and its load-deformation curve has a constant slope. Compared with the Super Post and Wedge Prop, the Micon Yield Capsule is not an economical yielding support, and thus its use may be

limited.

5. Super Post: The Super Post is more yieldable than the plain timber post and Micon Yield Capsule. The preliminary testing shows that the Super Post is a bi-stiffness yielding support and thus its load-deformation curve has two stages. In the first stage, the deformation is very small and the stiffness is large, while the opposite can be said about the second stage. Although the Super Post is superior to the Micon Yield Capsule, it may not effectively compete with the more yieldable, and cheaper Wedge Prop.

6. Wedge prop: Preliminary testing of the wedge prop shows that it has very good load-deformation characteristics. Generally the load-deformation curves can be divided into two stages. The first stage is before the yielding of the pod and the second stage is after the yielding of the pod. Depending on the load-deformation relationship in the second stage, the curves can be classified into two categories. In the first category, load increases as the prop deforms, and in the second category load does not change as the deformation increases. The maximum load which can be borne by the wedge prop is affected by the wood species. Factors such as the distance between the bands, the depth of the sawcut, the tightness of the bands, the strength of the band material, etc. all contribute to the mechanical properties of wedge props. From a theoretical point of view, the relationship between the stress in the wood log and that in the band can be established when the wedge prop is subjected to uniaxial load. The relationship can be used to determine the possible failure modes of the wedge props. The wedge prop is a bi-stiffness yielding support, and it is more yieldable but

cheaper than the Super Post. Thus, the wedge prop is a very promising support.

7. Plain concrete support: Plain concrete supports are rigid supports. They can resist a very high load with little deformation. The failure mode of plain concrete supports can be dangerous. They will fail suddenly and violently when their strengths are exceeded. Water-cement ratio, properties and proportions of concrete constituents, the method of mixing and placing, the degree of compaction, curing condition and the age of concrete affect the strength of plain concrete, as well as of other kinds of concretes. Plain concrete supports can be used under heavy roof pressure and strong roof conditions. However, the dangerous failure mode of plain concrete may limit its use.

8. Steel-fiber-reinforced concrete support: The pre-failure characteristics of steel-fiber-reinforced concrete under compression are the same as that of plain concrete, but the post-failure characteristics of steel-fiber-reinforced concrete are dramatically improved. Thus, when subjected to compressive load, steel-fiber-reinforced concrete will not fail as dangerously as plain concrete does. Another advantage of steel-reinforced concrete over plain concrete is that its tensile strength is higher than that of plain concrete. Steel-fiber-reinforced concrete can be used as a substitute for plain concrete, but the cost will be higher.

9. Sandwich cribs: The sandwich crib is a yieldable support. Its yieldability is controlled by the yielding members of the crib. For example, in a sandwich crib composed of concrete and timber, the yieldability of the crib is mainly dominated by the timber components.

The behavior of the sandwich crib is affected by the following factors:

(1) the strength of the concrete blocks, (2) the shape of the concrete blocks, (3) the uniformity and surface finish of the blocks, (4) species of timber, (5) size of timber members, (6) tensile strength of the timber, and (7) creep of the timber. The sandwich crib can be used under conditions of heavy roof pressure and large roof to floor convergence.

It is a very promising support.

10. Yielding steel post: The yielding steel post has a load capacity of 45 tons and a potential yield of 24 inches. It is a yieldable support. Laboratory and field testing conducted by the Bureau of Mines has shown that the yielding steel post is a workable mechanism for supporting ground. With further improvements in its design, the post may gain acceptance in underground mining.

11. Steel friction props: Two types of steel friction props were introduced, namely HZJA and HZWA. Both of them are yieldable supports. The HZJA is a mono-stiffness yielding support and the HZWA is a bi-stiffness one. These supports are expensive compared with timber yielding supports such as the Super Post and wedge prop, but they may be reusable.

12. Steel arches: Three types of arches were discussed: the rigid arch, the articulated arch, and the yielding arch. By the definition of a yieldable support, rigid arches can not be simply classified as rigid supports. Based on the single-point crown tests, except for the 1-piece welded arch, other types of rigid arch should also be regarded as yielding supports. However, one should view this conclusion with caution since the single-point test may be biased. Tests show that the strength

of the 3-piece arch is higher than that of the 2-piece one. There are no test data available for the articulated arch, but it is reasonable to say that the bending moment existing in the rigid arch will be eliminated in the articulated arch. A steel yielding arch can yield more than 10 percent of its height. It possesses very good load-deformation characteristics with a load-deformation curve similar to that of a hydraulic prop. The steel yielding arch has been successfully used in supporting soft rock entries where the closure of the surrounding rock is enormous. A disadvantage of the steel yielding arch is its high cost.

The maximum load and deformation for each type of support are summarized in Table 7.1.

7.2 Recommendations For Future Work

Based on the results of the evaluation, further research areas on underground supports can be recommended:

1. Continuing research on the wedge prop and optimizing its parameters.
2. Development of new types of concrete supports. The new concrete supports should be in two different categories. One, like SFRC, is to improve the post-failure characteristics of the concrete. In addition to steel fiber, other types of fibers, such as mineral fibers and organic fibers, may be used. The other is to improve the pre-failure characteristics of the concrete. This can be achieved by adding ductile materials such as polymers into the concrete mixture. Ductile inclusions absorb the work of fracture of cracks propagating through the concrete

Table 7.1 Summary of the Maximum Loads and Deformation
For the Supports Evaluated

Support type	Cross section (in. x in.)	Maximum load (1000 lb.)	Maximum deformation (percentage)
Timber post (hickory)	6 x 8	150	1
Timber crib (beech)	30 x 30	200	24
Micon Yield Capsule	φ6	80	12
Super Post (locust)	φ8	200	17
Wedge Prop (hickory)	φ7.5	200	20
Concrete crib (plain)	16 x 16	1536	0.5
SFRC crib	16 x 16	896	0.7
Sandwich crib (9% P. board)	16 x 16	1459	3.5
Steel yield post	φ3.5 x φ4	90	28
HZWA prop		85	5.7
Steel arch (3-piece)	4x4 H-section	33	5.2
TH arch	U-section	80	10

and can retard crack propagation. They also provide some tensile strength across the cracks already formed in the concrete (Nicholl,1976). Other additives may also be added into the mixture to improve the pre-failure yieldability of the concrete.

3. Development of new types of sandwich crib. This may be achieved by combining different types of concrete with various yieldable materials.

4. Continuing research on the steel yielding arch. Various clamp mechanisms and cross-section profiles of the arch segments can be tried. Mechanical models can be established to analyze the behavior of the yielding arch.

5. Applying operations research techniques to optimize the overall economic results by choosing a proper support under a specified underground condition. Computer software can be developed in this area.

REFERENCES

- Allwes, R. A. and C. P. Mangelsdorf, "Design Procedure For arch Rehabilitation of High-Roof-Fall Area", Proceeding, Fifth Conference on Ground Control in Mining, Morgantwon, West Virginia, pp. 51-61, 1986.
- Anderson, G. L. and T. W. Smelser, "Development Testing and Analysis of Steel-Fiber-Reinforced Concrete Mine Support Members", Report of Investigation, U. S. Bureau of Mine, 1980.
- Arioglu, E. and A. Yuksel, "Dimensioning of Yieldable Steel Arches (TH Arches)", Journal of Mines, Metals & Fuels, pp. 280-282, June-July, 1983.
- Avitzur, B., Metal Forming: Processes and Analysis, McGraw-Hill Book company, 1968.
- Biron, C. and E. Arioglu, Design of Supports in Mines, John Wiley & Sons, 1983.
- Blight, G. E., "Strain-Controlled Tests on Model Mine Supports", Journal of the South African Institute of Mining and Metallurgy, pp. 233-242, April, 1978.
- Bodig, J. and B. A. Jayne, Mechanics of Wood and Wood Composites, Van Nostrand Reinhold Company, 1982.
- Bulleit W. M., "Reinforcement of Wood Materials: A Review", Wood and Fiber Science, 16(3), pp. 391-397, 1984.
- Chlumecky, N. and R. W. Smith, "Donut Cribbing: A New Heavy-Duty Roof Support Concept", Proceedings, Fifth Conference on Ground Control in Mining, Morgantown, West Virginia, pp. 29-43, 1986.
- Chudnoff, M., Eslyn, W. E. and D. B. McKeever, "Decay in Mining timbers, Part III. Species-Independent Stress Grading", Forest Products Journal, Vol. 34, No.3, pp. 43-50, 1984.
- Cook, R. D., and W. C. Young, Advanced Mechanics of Materials, Macmillan Publishing Company, 1985.
- Cramer, S. M. and J. R. Goodman, "Model For Stress Analysis and Strength Prediction of Lumber", Wood and Fiber Science, 15(4), pp. 338-349, 1983.
- Cramer, S. M. and J. R. Goodman, "Failure Modeling: A Basis For Strength Prediction of Lumber", Wood and Fiber Science, 18(3), pp. 446-459, 1986.

- Dunford, J. P. and L. N. Henton, "Development of a Yielding Steel Post", Proceeding, Fifth Conference on Ground Control in Mining, Morgantown, West Virginia, pp. 44-50, 1986.
- Faulkner, G. J., Tang, W. and Z. Yu, "Investigation of Some Alternatives to Timber Posts and Cribs", Proceeding, Fifth Conference on Ground Control in Mining, Morgantown, West Virginia, pp. 61-72, 1986.
- Faulkner, G. J., Yu, Z. and W. Tang, "Study of Timber and Alternatives For Mine Roof Control", Proceeding, Fourth Annual Workshop, Generic Mineral Technology Center, Mine Systems Design and Ground Control, Moscow, Idaho, 1986.
- Fintel, M., Handbook of Concrete Engineering, Van Nostrand Reinhold Company, 1985.
- Flint, J. D., Buchan, I. F., Strachan, I. D. N., and C. A. Clarkson, "Partial Pillar Extraction With Controlled Goafing of the Superincumbent Strata", Journal of South African Institute of Mining and Metallurgy, pp. 193-199, July, 1984.
- Forest Products Lab, U. S. Department of Agriculture, Wood Handbook: Wood as an Engineering Material, Agriculture Handbook No. 72, 1974.
- Gerhards, C. C., "Effect of Moisture Content and Temperature on The Mechanical Properties of Wood: An Analysis of Immediate Effects", Wood and Fiber Science, 14(1), pp. 4-36, 1982.
- Hahn, J. A., Blight, G. E., and L. Dison, "Support in Shallow Mines Using Horizontally Reinforced Systems", Journal of the South African Institute of Mining and Metallurgy, pp. 277-290, October, 1982.
- Hassoun, M. N., Design of Reinforced Concrete Structures, PWS Engineering, 1985.
- Haygreen, J. G., "Properties of Wood Building Materials", Wood: Its Structure and Properties, Vol. II, The Pennsylvania State University, pp. 22-54, 1981.
- Johnsson, H. B., "Evaluation of Yieldable Mine Supports", Undergraduate Research thesis, Department of Mining and Minerals Engineering, VPI&SU, April, 1985.
- Joughin, N. C. and A. J. Jager, "Solid-Waste Packing as a Support Medium at Depth", Journal of South African Institute of Mining and Metallurgy, pp.10-14, August, 1978.
- Jukes, S. G. and S. F. Smith, "Study of Deformation Behavior of Steel Arches in Gate Roadway", Mining Science and Technology, pp. 63-80, 3, 1985.

- Margo, E. and R. K. O. Bradley, "An Analysis of Load Compression Characteristics of Conventional Chock Packs", Journal of South African Institute of Mining and Metallurgy, pp. 364-397, April, 1966.
- McChesney, M., "Modern Materials For Underground Support", Journal of the South African Institute of Mining and Metallurgy, pp. 114-118, December, 1976.
- Nicholls, R., Composite Construction Materials Handbook, Prentice-Hall, Inc., 1976.
- Ortlepp, W. D., "Basic Engineering Principles in The Design of Sandwich-pack Support", Journal of The South African Institute of Mining and Metallurgy, pp. 275-288, June, 1978.
- Peng, S. S., Coal Mine Ground Control, John Wiley & Sons, 1978.
- Petersen, A. C. and R. C. Botha, "The Use of Concrete For Stope Support on Harmony Gold Mining Company Limited", Journal of South African Institute of Mining and Metallurgy, pp. 565-615, June, 1966.
- Qian, M., Strata Mechanics and Mine Ground Control, China Coal Publishing House, 1983 (in Chinese).
- Sadler, G. W., "Testing of Roadway Support Equipment", The Mining Engineer, pp. 237-245, October, 1984.
- Samson, M., "Finite Element Model For Predicting Modulus of Elasticity of Lumber Measured By Stress-Grading Machines", Wood and Fiber Science, 17(4), pp. 490-503, 1985.
- Schniewind, A. P., "Mechanical Behavior and Properties of Wood", Wood: Its Structure and Properties, Vol. I, The Pennsylvania State Universities, pp. 233-267, 1981
- Smart, B. G. D., Davies, D. O. and J. Somerville, "Application of the Roof-Strata-Tilt Approach to Pack Design", The Mining Engineer, pp. 187-191, September, 1984.
- Song, Z., Yu, L., Chen, M., and Y. Song, "The Relation Between the Support and The Surrounding Strata During Weighting Period", Selected Literatures on Strata Mechanics, Shandong Mining Institute, China, pp. 61-72, 1984 (in Chinese).
- Song, Z., Liu, Y. and Y. Jiang, "Determination of the Working Resistance of the Steel Friction Props", Coal Science and Technology, No. 11, 1983 (in Chinese).
- Sorfa, P., "Mining Timber Task Force", CSIR Special Report, Pretoria, South Africa, 1985.

- Spengler, M. G., "The Grouted Skeleton Pack", Journal of The South African Institute of Mining and Metallurgy, pp. 296-297, June, 1978.
- Stone, R. N., Risbrudt, C. and J. Howard, "Wood Products Use By Coal Mines", Forest Products Journal, Vol. 35, No. 6, pp. 45-52, 1985.
- Stone, S., "The Introduction of Concrete Sausage Packs at Rustenburg Platinum Mines Limited", Journal of the South African Institute of Mining and Metallurgy, pp. 243-248, April, 1978.
- Thomas, R. J., "Wood and Ultrastructure", Wood: Its Structure and Properties, Vol. I, The Pennsylvania State University, pp. 101-146, 1981.
- Vuuren, P. J. J. V., "The Design and Testing of Pipe-Sticks For Underground Stope Support", Journal of South African Institute of Mining and Metallurgy, pp. 125-133, December, 1978.

APPENDIX A

```
C *****
C *****
C FE2D ..... FINITE ELEMENT TWO DIMENSIONAL
C STRESS ANALYSIS 4-NODE QUAD ELEMENT LINEAR ELASTICITY
C ORIGINALLY WRITTEN BY DR.T.KUPPUSAMY, VPI&SU
C MODIFIED BY ZHANJING YU, VPI&SU
C *****
C *****
C MAIN PROGRAM
  DIMENSION ANAME(18)
  COMMON NOP,NOEL,NMATR,NTRAC,MOPS,MBDY,MATR,RO(10),E1(10),E2(10),
+ E3(10),P12(10),P21(10),P23(10),P32(10),P13(10),P31(10),G(10)
  1,IND(400,5),X(450),Y(450),ALX(450),ALY(450),KSTRG(450),ITRN(20),JT
  2RN(20),TRAX(20,2),TRAY(20,2),TH(10)
  COMMON/ONE/STIF(8,8),Q(8),B(4,8),C(4,4),AXQ(400),AYQ(400)
  COMMON /TWO/ IBWTH,MEQ,AAR(900),ASTF(900,90)
  COMMON/THREE/ISLK,STRS(4,400)
  DATA MAXEL,MAXNP,MAXMAT,MAXBW,MAXTR/400,450,10,90,20/
C
C PROBLEM IDENTIFICATION AND DESCRIPTION
C
1 READ 5, IPRNO,(ANAME(I),I=1,18)
  IF (IPRNO.LE.0) GO TO 4
  PRINT 9
  PRINT 6, IPRNO,(ANAME(I),I=1,18)
  PRINT 9
  CALL READIN (MAXEL,MAXNP,MAXMAT,MAXTR,ITRUN)
  ISLK=0
  MAXDOF=2*MAXNP
C COMPUTE MAX. NODAL DIFF AND BANDWIDTH
  MAXDIF=0
  DO 2 I=1,NOEL
  DO 2 J=1,4
  DO 2 K=1,4
  LL=IABS(IND(I,J)-IND(I,K))
  IF (LL.GT.MAXDIF) MAXDIF=LL
2 CONTINUE
  IBWTH=2*(MAXDIF+1)
  MEQ=2*NOP
  IF (IBWTH.GT.MAXBW) GO TO 3
  IF (ITRUN.GT.0) GO TO 4
  CALL GLOBL (ITRUN)
  IF (ITRUN.GT.0) GO TO 4
  CALL SOLVR
  PRINT 9
  PRINT 9
9 FORMAT(/'*****
1*****')
  PRINT 7, (I,AAR(2*I-1),AAR(2*I),I=1,NOP)
  PRINT 9
  CALL STRESS
```

```
C      CALL DISPLT(SCAL1, SCAL2)
      GO TO 1
3     PRINT 8, IBWTH, MAXBW
      GO TO 1
4     STOP
5     FORMAT (I5, 3X, 18A4)
6     FORMAT (/8H PROB NO, I5, 3H      , 18A4/)
7     FORMAT (37H OUTPUT      NODE      DISPLACEMENTS//13X, 4HNODE, 9X, 11
1HU = X-DISP., 9X, 11HV = Y-DISP./ (5X, I12, 2E20.8))
8     FORMAT (///12H BANDWIDTH =, I4, 25H EXCEEDS MAX. ALLOWABLE =, I4//30H
1 GO ON TO NEXT PROBLEM      )
      END
      SUBROUTINE READIN (MAXEL, MAXNP, MAXMAT, MAXTR, ITRUN)
      COMMON NOP, NOEL, NMATR, NTRAC, MOPS, MBDY, MATR, RO(10), E1(10), E2(10),
+E3(10), P12(10), P21(10), P23(10), P32(10), P13(10), P31(10), G(10),
1IND(400, 5), X(450), Y(450), ALX(450), ALY(450), KSTRG(450), ITRN(20), JTR
2N(20), TRAX(20, 2), TRAY(20, 2), TH(10)
C
      ITRUN=0
      READ 22, NOP, NOEL, NMATR, NTRAC, MOPS, MBDY
C
      PRINT 23, NOP, NOEL, NMATR, NTRAC, MOPS, MBDY
C
C     CHECKS TO BE SURE INPUT DATA DOES NOT EXCEED STORAGE CAPACITY
      IF (NOP.LE.MAXNP) GO TO 1
      ITRUN=ISTOP+1
      PRINT 24, MAXNP
1     IF (NOEL.LE.MAXEL) GO TO 2
      ITRUN=ISTOP+1
      PRINT 25, MAXEL
2     IF (NMATR.LE.MAXMAT) GO TO 3
      ITRUN=ISTOP+1
      PRINT 26, MAXMAT
3     IF (NTRAC.LE.MAXTR) GO TO 4
      ITRUN=ISTOP+1
      PRINT 27, MAXTR
4     IF (ITRUN.EQ.0) GO TO 5
      PRINT 28, ITRUN
      STOP
C
5     READ 29, (E1(I), E2(I), E3(I), TH(I), I=1, NMATR)
      READ 29, (P12(I), P21(I), P23(I), P32(I), I=1, NMATR)
      READ 29, (P13(I), P31(I), G(I), RO(I), I=1, NMATR)
      PRINT 30
      PRINT 31, (I, E1(I), E2(I), E3(I), TH(I), I=1, NMATR)
      PRINT 31, (I, P12(I), P21(I), P23(I), P32(I), I=1, NMATR)
      PRINT 31, (I, P13(I), P31(I), G(I), RO(I), I=1, NMATR)
C
C     READ AND PRINT NODAL DATA
      PRINT 32
      N=1
```

```
6 READ 33, M, KSTRG(M), X(M), Y(M), ALX(M), ALY(M)
  IF (M-N) 7, 10, 8
7 PRINT 34, M
  PRINT 35, M, KSTRG(M), X(M), Y(M), ALX(M), ALY(M)
  ITRUN=ISTOP+1
  GO TO 6
8 DF=M+1-N
  RX=(X(M)-X(N-1))/DF
  RY=(Y(M)-Y(N-1))/DF
9 KSTRG(N)=0
  X(N)=X(N-1)+RX
  Y(N)=Y(N-1)+RY
  ALX(N)=0.0
  ALY(N)=0.0
10 PRINT 35, N, KSTRG(N), X(N), Y(N), ALX(N), ALY(N)
  N=N+1
  IF (M-N) 11, 10, 9
11 IF (N.LE.NOP) GO TO 6
C
C READ AND PRINT ELEMENT PROPERTIES
  PRINT 36
  L=0
12 READ 38, M, (IND(M, I), I=1, 5)
13 L=L+1
  IF (M-L) 14, 16, 15
14 PRINT 37, M
  PRINT 39, M, (IND(M, I), I=1, 5)
  ITRUN=ISTOP+1
  GO TO 12
15 IND(L, 1)=IND(L-1, 1)+1
  IND(L, 2)=IND(L-1, 2)+1
  IND(L, 3)=IND(L-1, 3)+1
  IND(L, 4)=IND(L-1, 4)+1
  IND(L, 5)=IND(L-1, 5)
16 PRINT 39, L, (IND(L, I), I=1, 5)
  IF (M-L) 17, 17, 13
17 IF (NOEL-L) 18, 18, 12
18 CONTINUE
C
C READ AND PRINT SURFACE LOADING(TRACTION) CARDS
C CALL MESH(10.)
1111 IF (NTRAC.EQ.0) GO TO 20
  PRINT 40
  DO 19 L=1, NTRAC
  READ 41, ITRN(L), JTRN(L), TRAX(L, 1), TRAX(L, 2), TRAY(L, 1), TRAY(L, 2)
19 PRINT 42, ITRN(L), JTRN(L), TRAX(L, 1), TRAX(L, 2), TRAY(L, 1), TRAY(L, 2)
20 IF (ITRUN.EQ.0) GO TO 21
  PRINT 43, ITRUN
21 RETURN
C
22 FORMAT (6I5)
```

```
23  FORMAT (35H INPUT      PROBLEM      PARAMETERS //5X,40H TOTAL NO OF
1  NODES      . . . . . ,I5/5X,40H TOTAL NO OF ELEMENTS. . . .
2  . . . . . ,I5/5X,40H TOTAL NO OF DIFF  MATERIALS . . . . . ,I5/
35X,40H TOTAL NO OF TRACTION DATA CARDS . . . ,I5/5X,40H 1=PLANE S
4TRAIN,2=PLANE STRESS,0=AXI-SYM,I5/5X,40H BODY FORCES(1 = IN -Y DIR
5SEC., 0 = NONE),I5)
24  FORMAT (////33H EXCEEDS  NODAL POINTS, MAXIMUM =,I5)
25  FORMAT (////30H EXCEEDS  ELEMENTS, MAXIMUM = ,I5)
26  FORMAT (////30H EXCEEDS  MATERIALS, MAXIMUM =,I5)
27  FORMAT (////40H EXCEEDS  SURFACE LOAD CARDS, MAXIMUM = ,I5)
28  FORMAT (////28H EXECUTION STOP  BECAUSE OF,I5,13H LARGE ERRORS/)
29  FORMAT (4E10.3)
30  FORMAT (36H INPUT          MATERIAL PROPERTIES//10H          ,5X
1  ,10HMODULUS OF,6X,9HPOISSON S,7X,8HMATERIAL,7X,8HMATERIAL/4X,6HNUM
2BER,5X,10HELASTICITY,8X,7H RATIO ,8X,7HDENSITY,8X,7HTHKNES)
31  FORMAT (I10,4E15.4)
32  FORMAT (34H INPUT          NODAL POINT DATA //5X,5HNODAL,48X,7HX-
1DISP.,8X,7HY-DISP./5X,5HNUMBR,6X,4HTYPE,14X,1HX,14X,1HY,8X,7HOR LO
2AD,8X,7HOR LOAD)
33  FORMAT (2I5,4E10.3)
34  FORMAT (5X,17HERROR IN DATA NO.,I5/)
35  FORMAT (2I10,4E15.4)
36  FORMAT (34H INPUT          ELEMENT DATA //11X,31HCONNECTIVITY
1  OF ELEMENT NODES/3X,7HELEMENT,7X,1H1,7X,1H2,7X,1H3,7X,1H4,2X,8H
2MATERIAL)
37  FORMAT (5X,25HERROR IN ELEMENT DATA NO.,I5/)
38  FORMAT (6I5)
39  FORMAT (I10,4I8,I10)
40  FORMAT (37H INPUT          SURFACE LOADING DATA//17X,33HSURFACE L
1LOAD INTENSITIES AT NODES/4X,6HNODE I,4X,6HNODE J,10X,2HXI,10X,2HXJ
2,10X,2HYI,10X,2HYJ)
41  FORMAT (2I5,4E10.3)
42  FORMAT (2I10,4E12.4)
43  FORMAT (///45H          SOLUTION WILL NOT  PERFORMED,,I5,21H
1  FATAL CARD ERRORS  )
C   RETURN
    END
    SUBROUTINE GLOBL (ITRUN)
    COMMON/THREE/ISLK,STRS(4,400)
    COMMON NOP,NOEL,NMATR,NTRAC,MOPS,MBDY,MATR,RO(10),E1(10),E2(10),
+E3(10),P12(10),P21(10),P23(10),P32(10),P13(10),P31(10),G(10)
1,IND(400,5),X(450),Y(450),ALX(450),ALY(450),KSTRG(450),ITRN(20),JT
2RN(20),TRAX(20,2),TRAY(20,2),TH(10)
    COMMON/ONE/STIF(8,8),Q(8),B(4,8),C(4,4),AXQ(400),AYQ(400)
    COMMON /TWO/ IBWTH,MEQ,AAR(900),ASTF(900,90)
    DIMENSION LM(8)
    DO 22 I=1,NOEL
    DO 22 J=1,4
    STRS(J,I)=0.0
22  CONTINUE
C
```

```
ITRUN=0
C INITIALIZE OVERALL STIFFNESS MATRIX AND OVERALL LOAD VECTOR
DO 1 I=1,MEQ
AAR(I)=0.0
DO 1 J=1,IBWTH
1 ASTF(I,J)=0.0
C
C COMPUTE ELEMENT STIFFNESSES AND LOADS
C
DO 10 M=1,NOEL
IF (IND(M,5).GT.0) GO TO 2
ITRUN=ISTOP+1
GO TO 10
2 CALL ASTIF(M,AREA)
C
C ASSEMBLE STIFF MATRIX AND LOAD VECTOR
C
DO 90 I=1,4
90 LM(I)=2*IND(M,I)-2
DO 130 I=1,4
DO 130 K=1,2
II=LM(I)+K
KK=2*I-2+K
AAR(II)=AAR(II)+Q(KK)
DO 130 J=1,4
DO 130 L=1,2
JJ=LM(J)+L-II+1
LL=2*J-2+L
IF(JJ)130,130,100
100 IF(IBWTH-JJ)110,120,120
110 WRITE(6,340)M
ITRUN=ISTOP+1
GO TO 140
120 ASTF(II,JJ)=ASTF(II,JJ)+STIF(KK,LL)
130 CONTINUE
140 CONTINUE
10 CONTINUE
C
C ADD EXTERNALLY APPL. CONC. NODAL LOADS TO AAR
DO 12 N=1,NOP
IF (KSTRG(N).EQ.3) GO TO 12
K=2*N
IF (KSTRG(N).EQ.1) GO TO 11
AAR(K-1)=AAR(K-1)+ALX(N)
IF (KSTRG(N).NE.0) GO TO 12
11 AAR(K)=AAR(K)+ALY(N)
12 CONTINUE
C
C SURFACE TRACTION CONVERSION
IF (NTRAC.EQ.0) GO TO 14
DO 13 L=1,NTRAC
```

```
I=ITRN(L)
J=JTRN(L)
II=2*I
JJ=2*J
DX=X(J)-X(I)
DY=Y(J)-Y(I)
EL=SQRT(DX*DX+DY*DY)
PXI=TRAX(L,1)*EL
PXJ=TRAX(L,2)*EL
PYI=TRAY(L,1)*EL
PYJ=TRAY(L,2)*EL
IF(MOPS.NE.0)GO TO 5
PXI=PXI*X(I)
PXJ=PXJ*X(J)
PYI=PYI*X(I)
PYJ=PYJ*X(J)
5  CONTINUE
AAR(II-1)=AAR(II-1)+PXI/3.0+PXJ/6.0
AAR(JJ-1)=AAR(JJ-1)+PXI/6.0+PXJ/3.0
AAR(II)=AAR(II)+PYI/3.0+PYJ/6.0
AAR(JJ)=AAR(JJ)+PYI/6.0+PYJ/3.0
13  CONTINUE
C
C      INTRODUCE BOUNDARY CONDITIONS
C
14  DO 17 M=1,NOP
    IF (KSTRG(M).GE.0.AND.KSTRG(M).LE.3) GO TO 15
    ITRUN=ISTOP+1
    GO TO 17
15  IF (KSTRG(M).EQ.0) GO TO 17
    IF (KSTRG(M).EQ.2) GO TO 16
    CALL BOUNC (ALX(M),2*M-1)
    IF (KSTRG(M).EQ.1) GO TO 17
16  CALL BOUNC (ALY(M),2*M)
17  CONTINUE
    IF (ITRUN.EQ.0) GO TO 18
    PRINT 20, ITRUN
18  RETURN
C
340  FORMAT(5X,30HBAND WIDTH EXCEEDS ALLOWABLE ,I5/)
19  FORMAT (/5X,17H AREA OF ELEMENT ,I5,14H IS NEGATIVE /)
20  FORMAT (///42H SOLUTION WILL NOT BE PERFORMED BECAUSE OF ,I5,15H
1  DATA ERRORS /)
    END
    SUBROUTINE STRESS
    COMMON NOP,NOEL,NMATR,NTRAC,MOPS,MBDY,MATR,RO(10),E1(10),E2(10),
+E3(10),P12(10),P21(10),P23(10),P32(10),P13(10),P31(10),G(10)
1,IND(400,5),X(450),Y(450),ALX(450),ALY(450),KSTRG(450),ITRN(20),JT
2RN(20),TRAX(20,2),TRAY(20,2),TH(10)
    COMMON/ONE/STIF(8,8),Q(8),B(4,8),C(4,4),AXQ(400),AYQ(400)
    COMMON/TWO/IBWTH,MEQ,AAR(900),ASTF(900,90)
```

```
COMMON/THREE/ISLK,STRS(4,400)
DIMENSION P(4)
PI=3.1416
ISLK=1
PRINT 30
16 FORMAT(//,' E.NO.   SIG(R)   SIG(Z)   SIG(THETA)   SIG(R-THETA)
1   SIG1           SIG2           ANGLE1     ANGLE2     X(C.G.)     Y
2(C.G.)',/)
17 FORMAT(//,'E.NO.   SIG(X)   SIG(Y)   SIG(Z)   SIG(X-Y)
1   SIG1           SIG2           ANGLE1     ANGLE2     X(C.G.)     Y(C
2.G.)',/)
IF(MOPS.EQ.0)PRINT 16
IF(MOPS.EQ.1)PRINT 17
IF(MOPS.EQ.2)PRINT 17
DO 5 M=1,NOEL
MATR=IND(M,5)
DO 10 KK=1,4
10 P(KK)=STRS(KK,M)
CALL ASTIF(M,AREA)
DO 15 I=1,4
II=2*I
JJ=2*IND(M,I)
Q(II-1)=AAR(JJ-1)
15 Q(II)=AAR(JJ)
DO 20 I=1,4
DO 20 J=1,8
20 P(I)=P(I)-B(I,J)*Q(J)
IF(MOPS.EQ.0)GO TO 9
C P(3)=-PAR(MATR)*(P(1)+P(2))
IF(MOPS.EQ.2)P(3)=0.0
9 CONTINUE
AM=(P(1)+P(2))/2.
PM=(P(1)-P(2))/2.
DM=SQRT(PM**2+P(4)**2)
STRS1=AM+DM
STRS2=AM-DM
ANGLE1=ATAN(P(4)/PM)
ANGLE1=ANGLE1*180./(PI*2.)
IF(ANGLE1.GT.360.)ANGLE1=ANGLE1-360.
ANGLE2=ANGLE1+90.
30 FORMAT(//,'STRESSES'//)
PRINT40,M,(P(I),I=1,4),STRS1,STRS2,ANGLE1,ANGLE2,AXQ(M),AYQ(M)
40 FORMAT(1X,I5,10(2X,E10.3))
5 CONTINUE
RETURN
END
SUBROUTINE BOUNC (U,N)
COMMON /TWO/ IBWTH,MEQ,AAR(900),ASTF(900,90)
DO 2 M=2,IBWTH
K=N-M+1
IF (K.LE.0) GO TO 1
```

```
AAR(K)=AAR(K)-ASTF(K,M)*U
ASTF(K,M)=0.0
1 K=N+M-1
  IF (K.GT.MEQ) GO TO 2
  AAR(K)=AAR(K)-ASTF(N,M)*U
  ASTF(N,M)=0.0
2 CONTINUE
  ASTF(N,1)=1.0
  AAR(N)=U
  RETURN
  END
SUBROUTINE ASTIF(M, AREA)
COMMON NOP, NOEL, NMATR, NTRAC, MOPS, MBDY, MATR, RO(10), E1(10), E2(10),
+E3(10), P12(10), P21(10), P23(10), P32(10), P13(10), P31(10), G(10)
1, IND(400, 5), X(450), Y(450), ALX(450), ALY(450), KSTRG(450), ITRN(20), JT
2RN(20), TRAX(20, 2), TRAY(20, 2), TH(10)
COMMON/ONE/STIF(8, 8), Q(8), B(4, 8), C(4, 4), AXQ(400), AYQ(400)
COMMON/TWO/IBWTH, MEQ, AAR(900), ASTF(900, 90)
COMMON/THREE/ISLK, STRS(4, 400)
DIMENSION TT(4), SS(4)
DATA SS/-1., 1., 1., -1./, TT/-1., -1., 1., 1./
  II=IND(M, 1)
  JJ=IND(M, 2)
  KK=IND(M, 3)
  LL=IND(M, 4)
  MATR =IND(M, 5)
  AREA=0.0
  R12=P12(MATR)
  R21=P21(MATR)
  R23=P23(MATR)
  R32=P32(MATR)
  R13=P13(MATR)
  R31=P31(MATR)
  F1=E1(MATR)
  F2=E2(MATR)
  F3=E3(MATR)
  D=(1-R12*R21-R23*R32-R13*R31-2*R21*R32*R13)/(F1*F2*F3)
C*****
C  AXISYMMERTIC CASE
C*****
  C(1, 1)=(1-R23*R32)/(F2*F3*D)
  C(1, 2)=(R21+R31*R23)/(F2*F3*D)
  C(1, 3)=(R31+R21*R32)/(F2*F3*D)
  C(1, 4)=0.0
  C(2, 1)=C(1, 2)
  C(2, 2)=(1-R13*R31)/(F1*F3*D)
  C(2, 3)=(R32+R12*R31)/(F1*F3*D)
  C(2, 4)=0.0
  C(3, 1)=C(1, 3)
  C(3, 2)=C(2, 3)
  C(3, 3)=(1-R12*R21)/(F1*F2*D)
```

```

      C(3,4)=0.0
      C(4,1)=0.0
      C(4,2)=0.0
      C(4,3)=0.0
      C(4,4)=G(MATR)
IF(MOPS.EQ.0) GO TO 8
IF(MOPS.EQ.2)GO TO 7
      C(1,3)= 0.0
      C(2,3) = 0.0
      C(3,1) = 0.0
      C(3,2) = 0.0
      C(3,3) = 0.0
      C(3,4) = 0.0
GO TO 9
7 CONTINUE
C C(1,1)=E(MATR)/(1.-PRT*PRT)
C C(1,2)=PRT*C(1,1)
  C(1,3)=0.0
  C(1,4)=0.0
  C(2,1)=C(1,2)
  C(2,2)=C(1,1)
  C(2,3)=0.0
  C(2,4)=0.0
  C(3,1)=0.0
  C(3,2)=0.0
  C(3,3)=0.0
  C(3,4)=0.0
C C(4,4)=(((1.-PRT)/2.)*C(1,1))
9 CONTINUE
  RC=1.0
8 CONTINUE
  DO 10 I = 1,8
    Q(I) =0.0
  DO 10 J =1,8
10 STIF(I,J)=0.0
    X1 = X(II)
    X2 = X(JJ)
    X3 = X(KK)
    X4 = X(LL)
    Y1 = Y(II)
    Y2 = Y(JJ)
    Y3 = Y(KK)
    Y4 = Y(LL)
    A12 = X1-X2
    A13 = X1-X3
    A14 = X1-X4
    A23 = X2-X3
    A24 = X2-X4
    A34 = X3-X4
    B12 = Y1-Y2
    B13 = Y1-Y3
```

```
B14 = Y1-Y4
B23 = Y2-Y3
Y24 = Y2-Y4
B34 = Y3-Y4
AREA = A13*Y24-A24 *B13
XM=(X1+X2+X3+X4)/4.0
YM=(Y1+Y2+Y3+Y4)/4.0
AXQ(M)=XM
AYQ(M)=YM
DO 25 II =1,4
  S=SS(II)*0.577350269189626
  T=TT(II)*0.577350269189626
  XJ = AREA + S*(A34*B12-A12*B34)+T*(A23*B14-A14*B23)
  XJAC = XJ/8.0
  SP = 1.+S
  SM = 1.-S
  TP = 1.+T
  TM = 1.-T
  G1=0.
  G2=0.
  G3=0.
  G4=0.
IF(MOPS.NE.0) GO TO 27
  AL1 = 0.25*SM* TM
  AL2 = 0.25*SP* TM
  AL3 = 0.25*SP* TP
  AL4 = 0.25*SM* TP
  RC= AL1*X1 + AL2*X2+AL3*X3 +AL4*X4
  G1 = AL1/RC
  G2 = AL2/RC
  G3 = AL3/RC
  G4 = AL4/RC
27 CONTINUE
  XX1=(-A24+A34*S +A23*T)/XJ
  XX2=(A13-A34*S-A14*T)/XJ
  XX3=(A24-A12*S+A14*T)/XJ
  XX4=(-A13+A12*S-A23*T)/XJ
  YY1=(Y24-B34*S-B23*T)/XJ
  YY2=(-B13+B34*S+B14*T)/XJ
  YY3=(-Y24+B12*S-B14*T)/XJ
  YY4=(B13-B12*S+B23*T)/XJ
  FACTOR = XJAC*RC
  IF(ISLK.EQ.1)GO TO 25
C DEVELOP QUAD STIFFNESS MATRIX.
DO 30 I =1,4
  C1= C(I,1)*FACTOR
  C2= C(I,2)*FACTOR
  C3= C(I,3)*FACTOR
  C4= C(I,4)*FACTOR
  B(I,1)=C1*YY1 +C4*XX1+C3*G1
  B(I,2)= C2*XX1 +C4*YY1
```

```

      B(I,3)=C1*YY2 + C3*G2 +C4*XX2
      B(I,4)=C2*XX2 + C4 *YY2
      B(I,5)= C1*YY3 + C3*G3 + C4*XX3
      B(I,6)=C2*XX3 + C4*YY3
      B(I,7)=C1*YY4 + C3*G4 + C4*XX4
      B(I,8)=C2*XX4 + C4*YY4
30  CONTINUE
      DO 32 I=1,8
          C1 = B(1,I)
          C2 = B(2,I)
          C3 = B(3,I)
          C4 = B(4,I)
          STIF(1,I)=STIF(1,I)+C1*YY1+C3*G1+C4*XX1
          STIF(2,I) =STIF(2,I) + C2* XX1 + C4* YY1
          STIF(3,I)=STIF(3,I)+ C1*YY2+ C3*G2+ C4*XX2
          STIF(4,I)=STIF(4,I) + C2* XX2 + C4*YY2
          STIF(5,I)=STIF(5,I)+ C1*YY3+C3*G3+ C4*XX3
          STIF(6,I)=STIF(6,I)+C2*XX3+ C4*YY3
          STIF(7,I)=STIF(7,I)+ C1*YY4 +C3*G4+ C4*XX4
          STIF(8,I) =STIF(8,I)+C2* XX4 + C4*YY4
32  CONTINUE
          DO 33 I=1,8
              DO 33 J=1,8
33          STIF(I,J)=STIF(I,J)*TH(MATR)
C*****
C  COMPUTE LOAD DUE TO GRAVITY
C*****
      IF(MBDY.EQ.0)GO TO 25
      IF (MOPS .NE. 0) GO TO 28
          WT=-RO(MATR)*FACTOR*TH(MATR)
37          Q(2)=Q(2)+WT*AL1
              Q(4)=Q(4) + WT*AL2
              Q(6)=Q(6) + WT*AL3
              Q(8)=Q(8) + WT*AL4
      GO TO 25
28          WT=-AREA*RO(MATR)*TH(MATR)
          WT= WT/8.
          Q(2)=WT
          Q(4)=WT
          Q(6)=WT
          Q(8)=WT
25 CONTINUE
C*****
C  DEVELOP STRESS MATRIX BS AT CENTROID (AXQ,AYQ)
C*****
          IF(ISLK.EQ.0) GO TO 66
          DO 50 I=1,4
              C1= C(I,1)
              C2= C(I,2)
              C3= C(I,3)/(4.*XM)
          IF(MOPS.NE.0) C3=0.0
```

```
C4 = C(I,4)
T1= (C1*Y24 -C4 *A24)/AREA
T2= (-C1*B13+C4*A13)/AREA
T3= (-C2*A24+C4*Y24)/AREA
T4= (C2*A13-C4*B13)/AREA
  B(I,1)= C3+ T1
  B(I,3)= C3+ T2
  B(I,5)= C3- T1
  B(I,7) = C3-T2
  B(I,2) = T3
  B(I,4) = T4
  B(I,6) = -T3
  B(I,8) = -T4
50    CONTINUE
66    CONTINUE
      RETURN
      END
      SUBROUTINE SOLVR
        COMMON/TWO/IBWTH,MEQ,AAR(900),ASTF(900,90)
C SYMMETRIC BAND MATRX EQUATION SOLVR
        NRS= MEQ-1
        NR= MEQ
        DO 120 N=1,NRS
          M=N-1
          MR= MINO(IBWTH,NR-M)
          PIVOT= ASTF(N,1)
        DO 120 L=2,MR
          C= ASTF(N,L)/PIVOT
          I= M+L
          J=0
        DO 110 K=L,MR
          J= J+1
110      ASTF(I,J)= ASTF(I,J)-C*ASTF(N,K)
120      ASTF(N,L)=C
200     DO 220 N=1,NRS
          M=N-1
          MR= MINO(IBWTH,NR-M)
          C=AAR(N)
          AAR(N)= C/ASTF(N,1)
        DO 220 L=2,MR
          I= M+L
220      AAR(I)= AAR(I)-ASTF(N,L)*C
          AAR(NR)= AAR(NR)/ASTF(NR,1)
        DO 320 I=1,NRS
          N= NR-I
          M= N-1
          MR= MINO(IBWTH,NR-M)
        DO 320 K= 2,MR
          L= M+K
320      AAR(N)= AAR(N)-ASTF(N,K)*AAR(L)
400    RETURN
      END
```

**The vita has been removed from
the scanned document**